arXiv:1106.2060v2 [cond-mat.mes-hall] 12 Oct 2011

# Mechanical systems in the quantum regime

Menno Poot[1], Herre S. J. van der Zant

*Kavli Institute of Nanoscience, Delft University of Technology, P. O. B. 5046, 2600GA Delft, The Netherlands*

**Abstract**

Mechanical systems are ideal candidates for studying quantum behavior of macroscopic objects. To this end, a mechanical resonator has to be cooled to its ground state and its position has to be measured with great accuracy. Currently, various routes to reach these goals are being explored. In this review, we discuss different techniques for sensitive position detection and we give an overview of the cooling techniques that are being employed. The latter include sideband cooling and active feedback cooling. The basic concepts that are important when measuring on mechanical systems with high accuracy and/or at very low temperatures, such as thermal and quantum noise, linear response theory, and backaction, are explained. From this, the quantum limit on linear position detection is obtained and the sensitivities that have been achieved in recent opto and nanoelectromechanical experiments are compared to this limit. The mechanical resonators that are used in the experiments range from meter-sized gravitational wave detectors to nanomechanical systems that can only be read out using mesoscopic devices such as single-electron transistors or superconducting quantum interference devices. A special class of nanomechanical systems are bottom-up fabricated carbon-based devices, which have very high frequencies and yet a large zero-point motion, making them ideal for reaching the quantum regime. The mechanics of some of the different mechanical systems at the nanoscale is studied. We conclude this review with an outlook of how state-of-the-art mechanical resonators can be improved to study quantum *mechanics*

*Keywords:* Quantum-electromechanical systems; QEMS; Nano-electromechanical systems; NEMS; Optomechanics; Quantum-limited displacement detection; Macroscopic quantum mechanical effects; Active feedback cooling; Sideband cooling

**Contents**

**1 Introduction** **3**
1.1 Ground-state cooling and quantum-limited position detection . . . 4
1.2 Bottom-up and top-down nanomechanical devices . . . 5
1.3 Carbon-based materials . . . 5
1.4 Outline of this review . . . 9

**2 Mechanics at the nanoscale** **10**
2.1 Continuum mechanics . . . 10
2.2 Elasticity . . . 11
2.3 Energy, bending rigidity and tension . . . 13
2.3.1 Plates . . . 14
2.3.2 Beams . . . 15
2.4 Examples . . . 15
2.4.1 Cantilevers and doubly-clamped beams . . . 15
2.4.2 String resonators . . . 16
2.4.3 Buckled beams . . . 17
2.4.4 Nanobeams . . . 19
2.4.5 Nanodrums . . . 22

[1]Present address: Department of Electrical Engineering, Yale University, New Haven, CT 06520, USA
*Email addresses:* menno.poot@yale.edu (Menno Poot), h.s.j.vanderzant@tudelft.nl (Herre S. J. van der Zant)

**3 Backaction and cooling** **25**
3.1 From modes to harmonic oscillators . . . 25
3.2 The harmonic oscillator . . . 26
3.2.1 The classical harmonic oscillator . . . 26
3.2.2 The harmonic oscillator in quantum mechanics . . . 27
3.3 Thermal and quantum noise . . . 27
3.4 Backaction and quantum limits on position detection . . . 30
3.4.1 Continuous linear detectors . . . 30
3.4.2 The Haus-Caves derivation of the quantum limit . . . 32
3.4.3 A quantum-limited detector . . . 33
3.5 Cooling . . . 33
3.5.1 Backaction cooling . . . 35
3.5.2 Active feedback cooling . . . 35
3.5.3 Sideband cooling . . . 39
3.5.4 Concluding remarks . . . 41

**4 Detection methods** **42**
4.1 Cavities . . . 44
4.1.1 Fabry-Pérot cavities . . . 45
4.1.2 Movable membrane inside the cavity . . . 46
4.1.3 Optical cavities on the micro scale . . . 46
4.1.4 On-chip optical cavities . . . 47
4.1.5 Superconducting microwave cavities . . . 47
4.2 Transmission modulation based detection methods . . . 48
4.2.1 Optical waveguides . . . 49
4.2.2 Electron tunneling . . . 49
4.3 Capacitive detectors . . . 50
4.3.1 Single-electron transistors . . . 50
4.3.2 Quantum-point contacts . . . 51
4.3.3 Frequency mixing . . . 52
4.4 Piezoelectric resonators . . . 52
4.5 Flux-based position detectors . . . 53
4.5.1 SQUIDs . . . 53
4.5.2 Magnetomotive . . . 54
4.6 Level spectroscopy in suspended quantum dots . . . 54

**5 Prospects** **56**
5.1 NEMS as quantum-limited sensitive detectors . . . 56
5.2 Hybrid quantum *mechanical* systems . . . 57

**6 Acknowledgements** **59**

**A Complex Green's function and displacement** **60**

**B Optimal filtering of $v(t)$** **60**

**C Square-law detection** **61**

## 1. Introduction

Mechanics is probably the most well-known branch of physics as everyone encounters it in every-day life. It describes a wide range of effects: from the motion of galaxies and planets on a large scale, the vibrations of a bridge induced by traffic or wind, the stability of a riding bicycle, to the trajectories of electrons in an old-fashioned television on a microscopic scale. In the early days of physics, mainly objects that could be seen or touched were studied. Until the beginning of the twentieth century it was thought that the three laws of motion obtained by Newton described the dynamics of mechanical systems completely. However, the development of better telescopes and microscopes enabled the study of mechanical systems on both much larger and smaller length scales. In the early 1900s, the rapid developments that led to the theory of special and general relativity and quantum mechanics showed that the laws of classical mechanics were not the whole truth.

Relativistic corrections turn out to be important for objects with large masses or with velocities approaching the speed of light. It is therefore an important factor in astrophysics, where one studies the dynamics of heavy objects like galaxies and black holes or the bending of light by the curvature of space-time. When the masses and velocities of the objects involved are made smaller and smaller, the relativistic corrections eventually vanish and one obtains the classical laws of motion [1].

Quantum mechanics, on the other hand, is particularly well suited to describe the mechanics of objects at the other end of the length-scale range, i.e., (sub)atomic objects. In the beginning of the twentieth century, quantum theory successfully explained the photo-electric effect, black-body radiation, and the atomic emission spectra. Quantum mechanics is different from classical and relativistic mechanics in the sense that objects are no longer described by a definite position, but by a wavefunction. This wavefunction evolves deterministically according to the Schrödinger equation and its absolute value squared should be interpreted as the position probability-density function, the so-called Born rule [2]. To find the object at a particular location one has to *measure* its position. This process, however, inevitably disturbs the evolution of the wavefunction [3, 4].

Quantum mechanics does not only describe processes at the (sub)atomic scale successfully, but it also explains the microscopic origin of many macroscopic effects such as the electronic properties of solids, superfluidity and so on. Unlike in relativity where one can simply take the limit $m, v \to 0$, in quantum mechanics it is still not entirely clear how the transition from quantum mechanics to classical mechanics exactly happens [5, 6]. Although Ehrenfest's theorem implies that the expectation values of the momentum and potential energy obey Newton's second law [2], the classical laws of motion cannot in all cases be recovered by simply taking $\hbar \to 0$ as has recently been shown in calculating the quantum dynamics of nonlinear resonators [7].

Another issue that is still debated is how quantum mechanics should be interpreted [2, 8]: as the truth, as a tool to calculate outcomes of an experiment, or as an incomplete theory? This question has been asked since the early days of quantum theory, resulting in the famous Einstein-Podolsky-Rosen paper [9], but has still not been answered. The interpretation of quantum mechanics and its transition to the macroscopic world are related and can be reformulated into the question "Can a macroscopic object be put in a quantum superposition?" This was first illustrated by Schrödinger in 1935 with the famous dead-or-alive cat *gedanken* experiment. Superpositions of small objects are readily observed, a good example are the singlet and triplet spin states in a molecule, but this becomes increasingly difficult for larger and larger systems mainly due to decoherence [10, 11]. Superpositions have for example been created using the circulating current in superconducting quantum interference devices (SQUIDs) [12] and with fullerenes [13, 14].

Nanomechanical devices [15, 16] are interesting candidates to further increase the size of systems that can be put in a superposition [11, 17]. These systems are the logical continuation of micromechanical devices which are made using integrated-circuit technology, but then on a much smaller, nanometer scale. Micro-electromechanical systems (MEMS) are currently widely used as, for example, accelerometers in airbags, pressure sensors, and in projectors. When scaling these devices down to the nanometer scale, their resonance frequencies increase and at the same time their mass decreases. From an application point of view nano-electromechanical systems (NEMS) may enable single-atom mass-sensing, mechanical computing and efficient signal processing in the radio-frequency and microwave bands. From a scientific point of view these devices are interesting as they can be cooled to temperatures so low that the resonator is nearly always in its quantum-mechanical ground state. Figure 1 shows some examples of miniature mechanical resonators.

In the last decade, many groups have pursued demonstration the quantum limit of motion. The rapid progress in the development of sensitive optical techniques and mesoscopic electronics have led to detectors that have sensitivities that are approaching the quantum limit on position detection [3]. Moreover, very recently the long-sought quantum mechanical behavior of mechanical resonators has become reality in two different experiments indicating that the quantum regime of mechanical motion has now been entered: Selected by Science magazine as research breakthrough [21] of the year 2010, the groups of Cleland and Martinis demonstrated quantum mechanical behavior of a 6 GHz mechanical resonator by coupling it to a superconducting flux qubit [22]. At dilution refrigerator temperatures the first ten energy states of the harmonic mechanical oscillator, including the ground state, could be probed. The measurement itself is performed on the superconducting qubit which acts as a two-level quantum system whose response changes when the

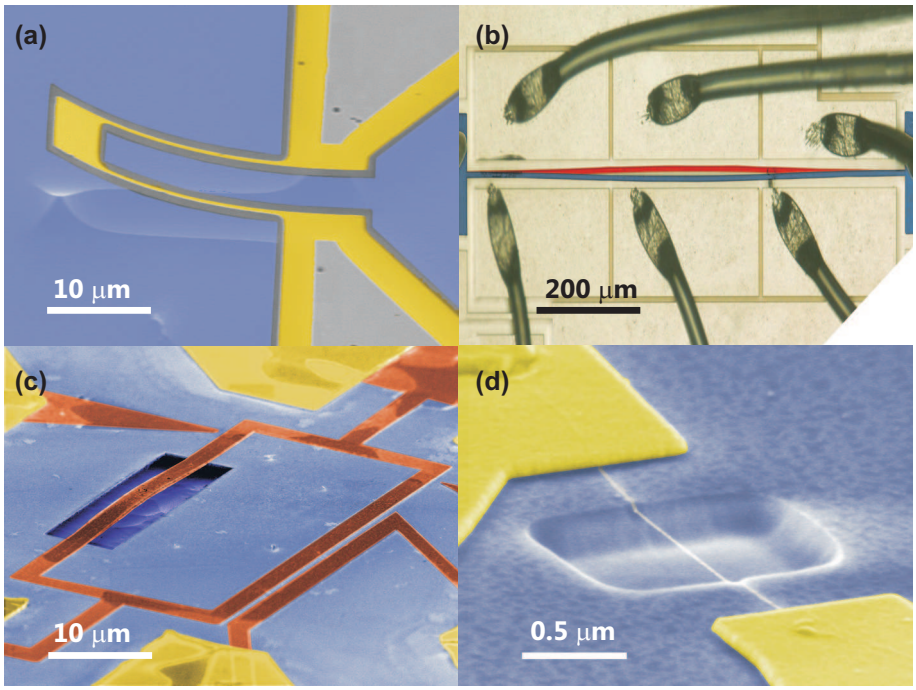


Figure 1: Different types of MEMS/NEMS used at Delft University of Technology. (a) Piezoresistive cantilever. A deflection of the cantilever changes the electrical resistance between the two sides. This resonator geometry can be used for mass detection. (b) Bistable buckled beam. Blue and red indicates the two stable positions of the beam, which can be used to encode digital information [18]. (c) A beam resonator that is embedded in the loop of a dc SQUID (red) [19]. A magnetic field couples the position of the beam to the magnetic flux through the loop. (d) Suspended carbon nanotube (white) as a flexural resonator [20].

occupation of the mechanical resonator state changes. A large coupling between the two quantum systems is achieved by using the piezoelectric properties of the mechanical resonator material. In a different approach Teufel *et al.* [23] use a superconducting microwave cavity to actively cool a mechanical drum resonator to such low temperatures that it is in the quantum mechanical ground state for most of the time. The drum resonator is integrated in the superconducting resonant circuit to provide strong phonon-photon coupling and the measurements use concepts developed for optical cavities to achieve efficient cooling.

These two breakthrough experiments not only show that non-classical behavior can be encoded in the motion of a mechanical resonator but also open a new exciting research field involving quantum states of motion. In this review we will summarize the main theoretical and experimental discoveries that have led to the demonstration of quantum motion. Our main focus will be on the mechanics, i.e., on the mechanical properties of resonators and on the different optical and electronic detection schemes that have been developed to measure their displacements. Since measuring always means that the detector has to be coupled to the resonator, we will also discuss the coupling and the consequences it may have on the measurement itself. Furthermore, the advantages and disadvantages of the various approaches will be discussed.

### *1.1. Ground-state cooling and quantum-limited position detection*

The concept of the quantum limit on mechanical motion detection and its implications became relevant in the 1970s when more and more sensitive gravitational wave detectors [24] were designed (see for example Refs. [25] and [26]), raising questions on the (im)possibility to violate Heisenberg uncertainty principle [2, 3, 27]. Nowadays, these issues are important when measuring micro- and nanomechanical devices with very sensitive detectors or at very low temperatures.

There are two important considerations when approaching the quantum limit. First, the thermal occupation is important, which is defined in Sec. 3.3 as $\overline{n} = (k_B T_R/h f_R) - 1/2$ where $f_R$ is the resonance frequency and $T_R$ is the resonator temperature. A value for $\overline{n}$ that is below 1 indicates that the resonator is in its ground state most of the time (see Sec. 3.3 for a more detailed description of the thermal occupation). Second, the zero-point motion sets the ultimate limit on the resonator displacement. At high temperatures and in the absence of actuation, Brownian motion determines the resonator position. As temperature decreases, the displacement decreases to the point that the quantum regime is reached ($\overline{n} \lesssim 1$). Zero-point motion of the undriven beam remains with an amplitude of $u_0 = \sqrt{\hbar/4\pi m f_R}$ with $m$ the resonator mass. To observe the zero-point motion, one has to detect it. This sounds trivial, but it turns out that a measurement on a quantum system inevitably disturbs it. Quantum mechanics sets a limit to the precision of continuously measuring the position of the resonator, the standard quantum limit. A detector at that limit is therefore called quantum-limited. Detection of the zero-point motion thus requires resonant frequencies higher than about 1 GHz (where $\overline{n} = 1$ corresponds to a temperature

of 50 mK, which can be reached in a dilution refrigerator) in combination with a position detection scheme that meets the quantum limit. Alternatively, a low-frequency resonator can be actively cooled to its quantum mechanical ground state. In experiments, both approaches are pursued and we discuss the status of both of them.

### *1.2. Bottom-up and top-down nanomechanical devices*

Table 1 provides an overview of the different groups that have performed experiments with mechanical resonators that approach the quantum limit in position-detection sensitivity or that have been cooled to a low resonator temperature. The micro- and nanomechanical devices listed in this table are made using so-called top-down fabrication techniques, which are also employed in the semiconductor industry. Different groups use different types of resonators: doubly clamped beams, singly clamped cantilevers, radial breathing modes of silica microtoroids, membranes, micromirrors and macroscopic bars. We have indicated the resonator mass, which ranges from 20 ag to 1000 kg, and the resonator frequency, which ranges from about 10 Hz to a few GHz. From these numbers the zero-point motion $u_0$ has been calculated; for top-down devices it is generally on the order of femtometers.

These top-down nanoscale structures listed in Table 1 (e.g. beams, cantilevers and microtoroids) are made by etching parts of a larger structure, for example a thin film on a substrate, or by depositing material (evaporating, sputtering) on a resist mask that is subsequently removed in a lift-off process. In both cases, patterning of resist is needed, which is done using optical or electron-beam lithography. State-of-the-art top-down fabricated devices have thicknesses and widths of less than 100 nanometer.

A major drawback of making smaller resonators to increase their frequency, is that the quality factor decreases [16]. The quality factor is a measure for the dissipation in the system. A low quality factor or "Q-factor" means a large dissipation, and this is an unwanted property for resonators in the quantum regime. The associated decoherence of quantum states then limits the time for performing operations with these states. For example, in the experiments of Ref. [22] where $Q$ is on the order of a few hundred, the time for the manipulation of quantum states is limited to only 6 ns. The decrease in Q-factor with device dimensions is often attributed to the increase in surface-to-volume ratio [16, 71, 72]. An explanation comes from the fabrication which may introduce defects at the surface during the micro-machining processes that are involved. These defects provide channels for dissipation, resulting in the low Q-factor.

Having this in mind, a different approach is to use the small structures that nature gives us, to build or assemble mechanical resonators. Bottom-up devices are expected not to suffer from excessive damping, as their surface can be defect-free at the atomic scale. Examples are inorganic nanowires[3], carbon nanotubes and few-layer graphene. The last two are examples of carbon-based materials. Using these bottom-up materials, mechanical devices with true nanometer dimensions can be made with the hope that surface defects can be eliminated. High Q-values are therefore expected for these devices, which, combined with their low mass, make them ideal building blocks for nano-electromechanical systems .

Table 2 shows the properties of mechanical resonators that have been made so far using bottom-up fabricated devices. Their frequencies are high: by choosing the right device geometry resonances in the UHF band (300 MHz - 3 GHz) are readily made, as Table 2 shows. When comparing the quality factors and zero-point motion of these devices, it is clear that the nanowire performance is more or less comparable to top-down fabricated devices since their thickness is of the order of 10-100 nm, about the size of the smallest top-down fabricated devices.

Due to their low mass $m$ and high strength (see the mechanical properties listed in Table 3 in Sec. 2) the frequencies of carbon-based resonators are high and their zero-point motion $u_0$ large. Note, that in Table 1 $u_0$ was given in femtometer, whereas in Table 2 it is given in picometer. Figure 2 illustrates this point more clearly. The quantum regime with a large $u_0$ and small $\overline{n}$ is positioned in the upper right corner. When cooled to dilution refrigerator temperatures, carbon-based resonators would therefore be in the ground-state while exhibiting relatively large amplitude zero-point fluctuations.

Position detectors for bottom-up NEMS, however, are not yet as sophisticated as those for the larger top-down counterparts. Consequently, non-driven motion at cryogenic temperatures (i.e., Brownian or zero-point motion) nor active cooling has been reported for carbon-based NEMS. The devices always need to be actuated to yield a measurable response. This is at least in part due to their small size, which makes the coupling to the detector small as well. Nevertheless impressive progress in understanding the electromechanical properties of bottom-up resonators has been made in recent years using so-called self-detecting schemes. In these schemes, the nanotube both acts as the actuator and detector of its own motion. Ultra-high quality factors have now been demonstrated for carbon nanotube resonators at low temperatures [81] as well as a strong coupling between electron transport and mechanical motion [106, 82].

### *1.3. Carbon-based materials*

In this Report we pay special attention to the mechanics of bottom-up materials as this has not been reviewed in such detail as the mechanics of the silicon-based top-down devices. In particular we will focus on the carbon-based materials as they have extraordinary mechanical and electrical properties.

[3] Sometimes "nanowire" is also used for top-down fabricated devices. Here, this term is used exclusively for grown wires.

Table 1: Overview of recent key experiments with micro- and nanomechanical resonators in chronological order. Several types of resonators and detection methods are used by different groups in the field and are measured at different temperatures $T$. The table shows the resonance frequency $f_R$, quality factor $Q$ and the mass $m$ of the resonator. From this, the zero-point motion $u_0$ is calculated.

| | **Group** | **Resonator** | $\mathbf{f_R}$ (MHz) | **Q** | **T** (K) | **m** (kg) | $\mathbf{u_0}$ (fm) | **Ref.** |
|---|---|---|---|---|---|---|---|---|
| 1 | Roukes | SiC beam | 1029 | 500 | 4.2 | $3.4 \cdot 10^{-17}$ | 15 | [28] |
| 2 | UCSB | GaAs beam | 117 | 1700 | 0.030 | $2.8 \cdot 10^{-15}$ | 5.1 | [29] |
| 3 | Schwab | SiN/Au beam | 19.7 | 35000 | 0.035 | $9.7 \cdot 10^{-16}$ | 21 | [30] |
| 4 | LMU | Si/Au cantilever | $7.30 \cdot 10^{-3}$ | 2000 | 295 | $8.6 \cdot 10^{-12}$ | 12 | [31] |
| 5 | Schwab | SiN/Al beam | 21.9 | 120000 | 0.030 | $6.8 \cdot 10^{-16}$ | 24 | [32] |
| 6 | LKB Paris | Si micromirror | 0.815 | 10000 | 295 | $1.9 \cdot 10^{-7}$ | $7.3 \cdot 10^{-3}$ | [33] |
| 7 | UCSB | AFM cantilever | $1.25 \cdot 10^{-2}$ | 137000 | 295 | $2.4 \cdot 10^{-11}$ | 5.3 | [34] |
| 8 | Vienna | $SiO_2/TiO_2$ beam | 0.278 | 9000 | 295 | $9.0 \cdot 10^{-12}$ | 1.8 | [35] |
| 9 | LKB Paris | Si micromirror | 0.814 | 10000 | 295 | $1.9 \cdot 10^{-7}$ | $7.4 \cdot 10^{-3}$ | [36] |
| 10 | MPI-QO | Silica toroid | 57.8 | 2890 | 300 | $1.5 \cdot 10^{-11}$ | 0.10 | [37] |
| 11 | Roukes | SiC/Au cantilever | 127 | 900 | 295 | $5.0 \cdot 10^{-17}$ | 36 | [38] |
| 12 | LIGO | Micromirror | $1.72 \cdot 10^{-4}$ | 3200 | 295 | $1.0 \cdot 10^{-3}$ | $7.0 \cdot 10^{-3}$ | [39] |
| 13 | LIGO | Micromirror | $1.27 \cdot 10^{-5}$ | 19950 | 295 | $1.0 \cdot 10^{-3}$ | 0.026 | [40] |
| 14 | LMU | Si micromirror | 0.547 | 1059 | 300 | $1.1 \cdot 10^{-14}$ | 37 | [41] |
| 15 | JILA | Gold beam | 43.1 | 5000 | 0.25 | $2.3 \cdot 10^{-15}$ | 9.2 | [42] |
| 16 | IBM | Si cantilever | $2.60 \cdot 10^{-3}$ | 55600 | 2.2 | $3.2 \cdot 10^{-13}$ | 100 | [43] |
| 17 | NIST | Si cantilever | $7.00 \cdot 10^{-3}$ | 20000 | 295 | $1.0 \cdot 10^{-10}$ | 3.5 | [44] |
| 18 | LKB Paris | Micromirror | 0.711 | 16000 | 295 | $7.4 \cdot 10^{-4}$ | $1.3 \cdot 10^{-4}$ | [45] |
| 19 | Harris | SiN membrane | 0.134 | 1100000 | 294 | $3.9 \cdot 10^{-11}$ | 1.3 | [46] |
| 20 | Vienna | Si cantilever | 0.557 | 2000 | 35 | $4.0 \cdot 10^{-11}$ | 0.61 | [47] |
| 21 | ANU | Mirror on beam | $8.48 \cdot 10^{-5}$ | 44500 | 300 | $6.9 \cdot 10^{-4}$ | 0.10 | [48] |
| 22 | MPI-QO | Silica toroid | 74.0 | 57000 | 295 | $1.0 \cdot 10^{-11}$ | 0.11 | [49] |
| 23 | JILA | Al beam | 0.237 | 2300 | 0.040 | $2.0 \cdot 10^{-15}$ | 133 | [50] |
| 24 | Roukes | SiC/Au beam | 428 | 2500 | 22 | $5.1 \cdot 10^{-17}$ | 20 | [51] |
| 25 | IBM | Si cantilever | $4.95 \cdot 10^{-3}$ | 22500 | 4.2 | $2.0 \cdot 10^{-12}$ | 29 | [52] |
| 26 | Delft | AlGaSb beam | 2.00 | 18000 | 0.020 | $6.1 \cdot 10^{-13}$ | 2.6 | [19] |
| 27 | AURIGA | Al bar | $8.65 \cdot 10^{-4}$ | 1200000 | 4.2 | $1.1 \cdot 10^{3}$ | $3.0 \cdot 10^{-6}$ | [53] |
| 28 | AURIGA | Al bar | $9.14 \cdot 10^{-4}$ | 880000 | 4.2 | $1.1 \cdot 10^{3}$ | $2.9 \cdot 10^{-6}$ | [53] |
| 29 | Alberta | Si cantilever | 1040 | 18 | 295 | $2.0 \cdot 10^{-17}$ | 20 | [54] |
| 30 | Tang | Si beam | 8.87 | 1850 | 295 | $1.3 \cdot 10^{-15}$ | 27 | [55] |
| 31 | JILA | Al beam | 1.53 | 300000 | 0.050 | $6.2 \cdot 10^{-15}$ | 30 | [56] |
| 32 | JILA | Al beam | 1.53 | 10000 | 0.050 | $6.2 \cdot 10^{-15}$ | 30 | [56] |
| 33 | LMU | SiN beam | 8.90 | 150000 | 295 | $1.8 \cdot 10^{-15}$ | 23 | [57] |
| 34 | Queensland | Silica toroid | 6.272 | 545 | 300 | $3.0 \cdot 10^{-8}$ | $6.7 \cdot 10^{-3}$ | [58] |
| 35 | Tang | Si cantilever | 13.86 | 4500 | 295 | $4.5 \cdot 10^{-16}$ | 37 | [59] |
| 36 | Vienna | Si cantilever | 0.945 | 30000 | 5.3 | $4.3 \cdot 10^{-11}$ | 0.45 | [60] |
| 37 | MPI-QO | Silica toroid | 65.0 | 2000 | 1.65 | $7.0 \cdot 10^{-11}$ | 0.043 | [61] |
| 38 | Painter | Si ph. crystal | 8.2 | 150 | 360 | $4.3 \cdot 10^{-14}$ | 4.9 | [62] |
| 39 | Oregon | Silica sphere | 118.6 | 3400 | 1.4 | $2.8 \cdot 10^{-11}$ | 0.050 | [63] |
| 40 | LIGO | Susp. mirror | $1.23 \cdot 10^{-4}$ | | 300 | $2.7 \cdot 10^{0}$ | $1.6 \cdot 10^{-4}$ | [64] |
| 41 | Painter | Silica double tor. | 8.53 | 4070 | 300 | $1.5 \cdot 10^{-13}$ | 2.6 | [65] |
| 42 | JILA | Al beam | 1.04 | 160000 | 0.015 | $1.1 \cdot 10^{-14}$ | 27 | [66] |
| 43 | MPI-QO / LMU | SiN beam | 8.07 | 10000 | 300 | $4.9 \cdot 10^{-15}$ | 15 | [67] |
| 44 | Schwab | SiN/Al beam | 6.30 | 1000000 | 0.020 | $2.1 \cdot 10^{-15}$ | 25 | [68] |
| 45 | MPI-QO / LMU | SiN beam | 8.30 | 30000 | 300 | $3.7 \cdot 10^{-15}$ | 16 | [69] |
| 46 | UCSB | AlN FBAR | 6170 | 260 | 0.025 | $2.8 \cdot 10^{-12}$ | 0.022 | [22] |
| 47 | Delft | AlGaSb beam | 2.14 | 24000 | 0.015 | $6.1 \cdot 10^{-13}$ | 2.5 | [70] |
| 48 | NIST | Al drum | 10.69 | 360000 | 0.020 | $4.8 \cdot 10^{-14}$ | 4.0 | [23] |

Table 2: Overview of recent experiments with bottom-up resonators. Several types of resonators are used: carbon nanotubes (CNT), nanowires (NW), single-layer graphene (SLG), and few-layer graphene (FLG) or graphene oxide (FLGO) sheets. The table shows the resonance frequency $f_R$ and quality factors at room and cryogenic temperature ($Q_{\mathrm{RT}}$ and $Q_{\mathrm{cryo}}$ resp.). $T_{\mathrm{min}}$ is the lowest temperature at which the resonator is measured. $m$ is the mass of the resonator and $\ell$ is its length. From these data, the zero-point motion $u_0$ is calculated.

| **Group** | **Type** | $\mathbf{f_R}$ (MHz) | $\mathbf{Q_{RT}}$ | $\mathbf{Q_{cryo}}$ | $\mathbf{T_{min}}$ (K) | $\ell$ ($\mu$m) | **m** (kg) | $\mathbf{u_0}$ (pm) | **Ref.** |
|---|---|---|---|---|---|---|---|---|---|
| Cornell | CNT | 55 | 80 | | 300 | 1.75 | $7.4 \cdot 10^{-21}$ | 4.52 | [73] |
| Delft | CNT | 60 | 100 | | 300 | 1.25 | $1.0 \cdot 10^{-20}$ | 3.66 | [20] |
| Berkeley | CNT | 350 | 440 | | 300 | 0.5 | $5.3 \cdot 10^{-20}$ | 0.67 | [74] |
| ICN | CNT | 3120 | 8 | | 300 | 0.77 | $5.8 \cdot 10^{-20}$ | 0.22 | [75] |
| ICN | CNT | 154 | 20 | | 300 | 0.265 | $1.1 \cdot 10^{-19}$ | 0.69 | [75] |
| ICN | CNT | 573 | 20 | | 300 | 0.193 | $4.0 \cdot 10^{-22}$ | 6.03 | [75] |
| ICN | CNT | 167 | 200 | 2000 | 5 | 0.9 | $1.4 \cdot 10^{-21}$ | 6.03 | [76] |
| Berkeley | CNT | 328.5 | 1000 | | 300 | 0.205 | $1.6 \cdot 10^{-21}$ | 4.01 | [77] |
| CalTech | CNT | 230 | | 200 | 6 | 0.45 | $4.8 \cdot 10^{-22}$ | 8.73 | [78] |
| Purdue | CNT | 0.9 | 3 | | 300 | 12.6 | $4.1 \cdot 10^{-16}$ | 0.15 | [79] |
| Chalmers | CNT | 62 | 50 | | 300 | 2.05 | $2.2 \cdot 10^{-17}$ | 0.08 | [80] |
| Delft | CNT | 360 | | 120000 | 0.02 | 0.8 | $5.3 \cdot 10^{-21}$ | 2.09 | [81] |
| ICN | CNT | 50 | 40 | 600 | 4 | 1 | $1.3 \cdot 10^{-21}$ | 11.41 | [82] |
| U. Wash. | CNT | 410 | | | 64 | | | | [83] |
| U. Illinois | CNT | 4 | 240 | | 300 | 6.2 | $5.9 \cdot 10^{-18}$ | 0.59 | [84] |
| LPMCN | CNT | 73.6 | 160 | | 300 | 2 | $8.5 \cdot 10^{-21}$ | 3.66 | [85] |
| CalTech | Pt NW | 105.3 | | 8500 | 4 | 1.3 | $4.0 \cdot 10^{-17}$ | 0.045 | [86] |
| CalTech | Si NW | 215 | | 5750 | 25 | 1.6 | $1.9 \cdot 10^{-17}$ | 0.045 | [87] |
| U. Penn. | GaN NW | 2.235 | 2800 | | 300 | 5.5 | $1.9 \cdot 10^{-16}$ | 0.141 | [88] |
| Yale | GaN NW | 8.584 | 1008 | | 300 | 2.04 | $1.6 \cdot 10^{-17}$ | 0.245 | [89] |
| Lyon | SiC NW | 0.043 | 159000 | | 300 | 93 | $9.8 \cdot 10^{-15}$ | 0.141 | [90] |
| Alberta | Si NW | 1.842 | 4200 | | 300 | 5.2 | $2.4 \cdot 10^{-17}$ | 0.437 | [91] |
| Alberta | Si NW | 1.842 | 2000 | 10000 | 77 | 11.2 | $4.6 \cdot 10^{-16}$ | 0.099 | [91] |
| Penn. State | Si NW | 1.928 | 4830 | | 300 | 11.8 | $2.4 \cdot 10^{-15}$ | 0.043 | [92] |
| Penn. State | Rh NW | 7.186 | 1080 | | 0.3 | 5.8 | $4.4 \cdot 10^{-15}$ | 0.016 | [92] |
| CalTech | Si NW | 96 | 550 | | 300 | 1.8 | $5.3 \cdot 10^{-18}$ | 0.129 | [93] |
| Tsinghua U. | ZnO NW | 26 | 5 | | 300 | 12 | $1.9 \cdot 10^{-14}$ | 0.004 | [94] |
| U. Illinois | Si NW | 0.208 | 10000 | | 300 | 14.4 | $5.1 \cdot 10^{-17}$ | 0.887 | [95] |
| U. Mich. | $SnO_2$ NW | 59 | 2200 | | 300 | 2.5 | $2.2 \cdot 10^{-16}$ | 0.025 | [96] |
| Madrid | Si NW | 2.2 | 2000 | | 300 | 7.5 | $5.5 \cdot 10^{-16}$ | 0.083 | [97] |
| Cornell | SLG | 70.5 | 78 | | 300 | 1.1 | $1.4 \cdot 10^{-18}$ | 0.287 | [98] |
| ICN | FLG | 32 | 64 | | 300 | 2.8 | $2.7 \cdot 10^{-17}$ | 0.098 | [99] |
| Cornell | FLG | 160 | 25 | | 300 | 4.75 | $4.5 \cdot 10^{-16}$ | 0.011 | [100] |
| NRL | FLGO | 57.6 | 3000 | | 300 | 2.75 | $7.8 \cdot 10^{-17}$ | 0.043 | [101] |
| Cornell | FLG | 8.36 | 97 | | 300 | 8 | $3.5 \cdot 10^{-17}$ | 0.169 | [102] |
| Columbia | SLG | 130 | 125 | 14000 | 5 | 3 | $2.2 \cdot 10^{-18}$ | 0.169 | [103] |
| TIFR | SLG | 64 | 250 | 2100 | 7 | 2.5 | $1.9 \cdot 10^{-17}$ | 0.083 | [104] |
| TIFR | $NbSe_2$ | 24 | | 215 | 10 | 3.3 | $1.8 \cdot 10^{-15}$ | 0.014 | [105] |

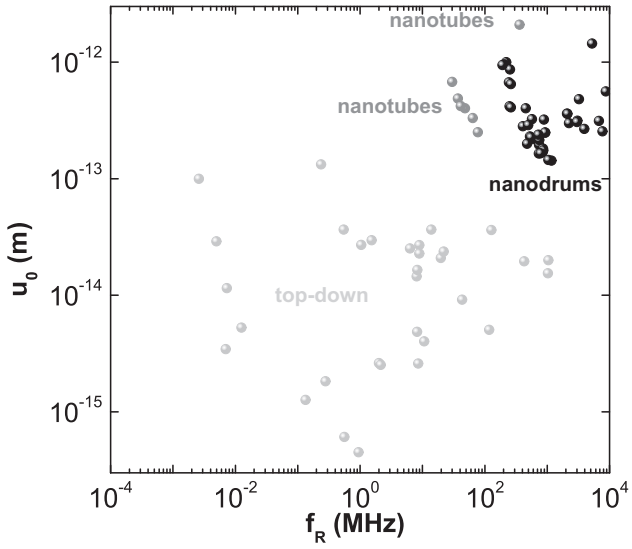


Figure 2: Comparison of the resonance frequency $f_R$ and zero-point motion $u_0$ of top-down (Table 1) and two kinds of bottom-up devices: Suspended carbon nanotubes [20, 81, 106] and graphene nanodrums [107]. The resonance frequencies and zero-point motion are much larger for the bottom-up devices.

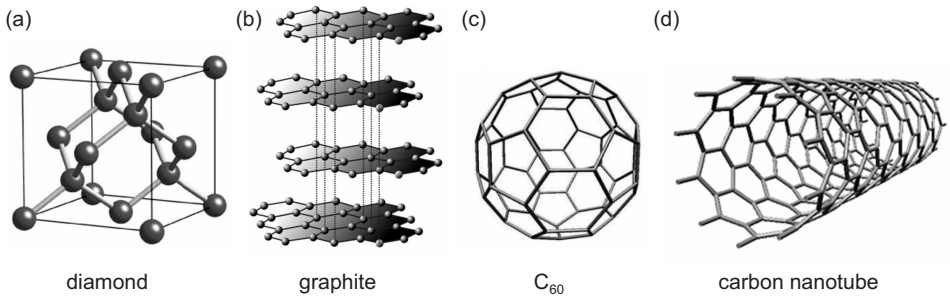


Figure 3: The structure of the different allotropes of carbon. (a) Diamond has two intertwined face-centered cubic lattices. (b) Graphite consists of stacked planes of hexagonally ordered carbon atoms. A single plane is called a "graphene sheet". (c) A $C_{60}$ buckyball molecule. (d) A single-walled carbon nanotube, which can be viewed as a graphene sheet that has been rolled up and sewn together. (c) and (d) Reprinted from Nanomedicine: Nanotechnology, Biology and Medicine, **4** 3, M. Foldvari, M. Bagonluri, Carbon nanotubes as functional excipients for nanomedicines: I. pharmaceutical properties, 173–182, Copyright (2008), with permission from Elsevier.

Carbon exists in many different forms, ranging from amorphous coal to crystalline graphite and diamond. Diamond has a face-centered cubic structure as shown in Fig. 3a and is one of the hardest materials known. Its Young's modulus (Table 3) is extremely high: about 1 TPa. Graphite has a very different crystal structure: it consists of stacked planes of carbon atoms in a hexagonal arrangement (Fig. 3b). Its Young's modulus for in-plane stress is nearly as high as that of diamond, but it is much lower for out-of-plane stress, as Table 3 will indicate. This difference is caused by the nature of the bonds holding the carbon atoms together. Atoms in one of the planes are covalently bonded to each other, whereas different planes are held together by the much weaker van der Waals force.

Graphite and diamond were already known for millennia, but in the last decades novel allotropes of carbon were discovered. First, in 1985 $C_{60}$ molecules, called Buckminsterfullerenes or "buckyballs", were synthesized [108]. Then in the early 1990s carbon nanotubes were discovered [109]. These consist of cylinders of hexagonally ordered carbon atoms; similar to what one would get if one were to take a single layer of graphite and role it up into a cylinder. In 2004 another allotrope called "graphene" was identified [110, 111]. This is a single layer of graphite, which is, unlike a nanotube, flat. Graphene is usually deposited onto a substrate using mechanical exfoliation, and high-quality sheets of mm-size have been made using this technique [112]. Another way of making graphene devices is to grow it directly on a substrate, and in a semi-industrial process meter-sized sheets have been reported [113]. Although truly two-dimensional structures are not energetically stable [114], graphene can exist due to fact that it contains ripples that stabilize its atomically thin structure [115, 116, 117, 118]. Figure 3 shows the structure of the four different carbon allotropes.

Although nanomechanical devices have been made out of diamond using top-down fabrication techniques [119, 120, 71, 121], in this Review we focus on bottom-up fabricated carbon-based NEMS made from few-layer graphene or suspended carbon nanotubes.

*1.4. Outline of this review*

This Review consists of this introduction, three main Sections, one on nanomechanics, one on backaction and cooling, and the last one focusses on different types of detectors. These are supplemented with a final Section summarizing some prospects and future directions in the field of quantum electromechanical systems or QEMS in short. In Section 2 we will discuss mechanics at the nanoscale. From continuum mechanics, the general equations of motion are obtained. These are illustrated by studying the dynamics of a number of nanomechanical devices, such as beam and string-like resonators, buckled beams and suspended carbon nanotubes. We will demonstrate that the dynamics of a particular vibrational mode of the resonator is that of a harmonic oscillator. Another important point is that in nanoscale devices, tension is a crucial property that must be included in the analysis. As we will show it also provides a unique tool for the tuning of resonators when their thickness is on the atomic to nanometer scale.

In Section 3 we discuss the properties of the (quantum) harmonic oscillator and we study the effects of backaction. A measurement always influences the measured object itself and this is called backaction. It has important consequences for linear detection schemes, and we will show that backaction ultimately limits their position resolution to what is known as the standard quantum limit. This limit will be derived in several ways. Backaction, however, can also be used to ones advantage as it provides a way to cool resonator modes. This can be done by backaction alone (self-cooling). Alternatively, the resonator temperature can be lowered by adopting active cooling protocols. An overview of the two most popular protocols will be given, including a summary of the main achievements.

In general, two distinct approaches for position detection of mechanical oscillators are used: optical and electrical. In Sec. 4, we give an overview of the different detection schemes. We will discuss the use of optical cavities in various forms, optical waveguides and their analogues in solid state devices in which electrons play the role of photons. In addition, we will summarize the concepts behind capacitive and inductive actuation and detection as well as the self-detection schemes that are used in bottom-up NEMS devices. Special attention will be paid to the achieved position resolution and to the limitations that prevent the standard quantum limit to be reached. Furthermore, we explain the mechanisms behind the backaction and, when possible, quantify the coupling between resonator and detector.

## 2. Mechanics at the nanoscale

Nearly, all objects, including macroscopic and nanometre-sized systems, have particular frequencies at which they can resonate when actuated. These frequencies are called the eigenfrequencies or normal frequencies; when actuated at an eigenfrequency, i.e. on resonance, the amplitude of vibration can become very large and this can have catastrophic consequences. Examples include the breaking of a glass by sound waves and the collapse of the Tacoma bridge which was set in motion by the wind flowing around it.

Continuum mechanics provides the tools to calculate these frequencies. For simple geometries such as cantilevers, doubly-clamped beams or thin plates, the frequencies of flexural or torsional modes can be calculated analytically. However, in many NEMS experiments more complicated geometries are used, such as microtoroids [122], suspended photonic crystal structures [62, 123], or film bulk acoustic resonators (FBARs) [22, 124] and the vibrational mode may have more a complicated shape than the simple flexural or torsional motion. To calculate the eigenfrequencies and mode shapes in these cases one has to rely on numerical calculations. Popular implementations include the software packages ANSYS and COMSOL which are based on the finite-element method. These packages have additional advantages as they provide a means to model other properties of the nanomechanical system: This includes electrostatic interactions (see e.g. Refs. [125, 126, 57]), thermal effects [127, 122], and electromagnetic (optical) properties [55, 62, 128].

In this Section, we will summarize some main results of continuum mechanics needed to describe the experiments discussed in this Report. We will review analytical expressions for the eigenfrequencies of simple structures such as beams, buckled beams and strings. This material has been described in several textbooks (see e.g. the book by A. Cleland [15]). Less attention has been devoted to thin beams or plates with nanometer-sized cross sections made from, for example, carbon nanotubes or graphene. These resonators are in a different regime than top-down devices that generally have larger sizes. In particular, the deflection of these nano-resonators can exceed their thickness or radius so that tension-induced nonlinear effects start to play a role. We derive the equations for describing these nonlinear effects in nanobeams and show that the induced tension can be used to tune the frequencies over a large range. We end this section with a discussion on the mechanics of (layered) graphene resonators that can be viewed as miniature drums.

### *2.1. Continuum mechanics*

To describe the motion of mechanical objects, the dynamics of all particles (i.e., atoms and electrons) which make up the oscillator should, in principle, be taken into account. It is, however, known that for large, macroscopic objects this is unnecessary and that materials can be accurately described as a continuum with the mechanical behavior captured by a few parameters such as the elasticity tensor. Molecular dynamics simulations [129, 130, 131, 132, 133, 134] and experiments [20, 135, 107] demonstrate that even for nanometer-sized objects continuum mechanics is, with some modifications, still applicable. This means that the dynamics of the individual particles is irrelevant when one talks about deflections and deformations; the microscopic details do, however, determine the material properties and therefore also the values of macroscopic quantities like the Young's modulus or the Poisson ratio.

The basis of continuum mechanics lies in the relations between strain and stress in a material. The strain tells how the material is deformed with respect to its relaxed state. After the deformation of the material, the part that was originally at position $\mathbf{x}$ is displaced by $\mathbf{u}$ to its new location $\mathbf{x} + \mathbf{u}$. The strain describes how much an infinitesimal line segment is elongated by the deformation $\mathbf{u}(x, y, z)$ and is given by[4] [136]:

$$\gamma_{ij} = \frac{1}{2}\left(\frac{\partial u_i}{\partial x_j} + \frac{\partial u_j}{\partial x_i} + \frac{\partial u_m}{\partial x_i}\frac{\partial u_m}{\partial x_j}\right). \tag{1}$$

This definition shows that strain is symmetric under a reversal of the indices, i.e., $\gamma_{ij} = \gamma_{ji}$. The diagonal elements (i.e., $i = j$) of the first two terms are the normal strains, whereas the off-diagonal elements ($i \neq j$) are the shear strains. Eq. 1 is exact, but the last, non-linear term is only relevant when the deformations are large [15] and will not be considered in this work.

To deform a material external forces have to be applied, which in turn give rise to forces inside the material. When the material is thought of as composed of small elements, each element feels the force exerted on its faces by the neighboring elements. The magnitude and direction of the force depend not only on the location of the element in the material but also on the *orientation* of its faces (see Fig. 4a). The force $\delta\mathbf{F}$ on a small area $\delta A$ of the element is given by:

$$\delta F_i = \sigma_{ij} n_j \delta A, \tag{2}$$

[4] In this Report, the so-called Einstein notation [136] for the elements of vectors and tensors is employed. When indices appear on one side of an equal sign only, one sums over them, without explicitly writing the summation sign. For example, $x_i = R_{ij}x_j$ reads as $x_i = \sum_{j=1}^{3} R_{ij}x_j$. The index runs over the three cartesian coordinates $(x, y, z)$, where $x_1 = x$, $x_2 = y$ and $x_3 = z$. Finally, the symbols $\hat{\mathbf{x}}_i$ ($\hat{\mathbf{x}}$, $\hat{\mathbf{y}}$ and $\hat{\mathbf{z}}$) denote the unit vectors in the fixed rectangular coordinate system (which form a basis) so that a vector $\mathbf{r}$ can be expressed as $\mathbf{r} = r_i\hat{\mathbf{x}}_i$.

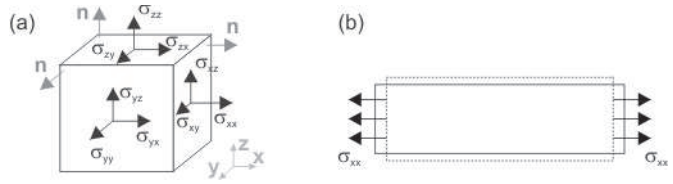


Figure 4: (a) Visualization of the stress tensor on a cubic element $\Delta V$. The force per unit area is the inner product of the stress tensor and the normal vector of the surface $\mathbf{n}$. (b) Deformation of a plate under plane stress. The original plate (dotted) is deformed by the stress $\sigma_{xx}$.

where $\mathbf{n}$ is the vector perpendicular to the surface and $\boldsymbol{\sigma}$ is the stress tensor. Now consider an element of the material with mass $\Delta m$ and volume $\Delta V$. When it is moving with a speed $\mathbf{v} = \dot{\mathbf{u}}$, its momentum $\mathbf{\Delta p}$ is:

$$\mathbf{\Delta p} \equiv \int_{\Delta m} \mathbf{v}\, \mathrm{d}m = \int_{\Delta V} \rho \mathbf{v}\, \mathrm{d}V, \tag{3}$$

where $\rho$ is the mass density. The rate of change of momentum equals the sum of the forces working on the element. These forces include the stress $\boldsymbol{\sigma}$ at the surface and body forces $\mathbf{F_b}$ that act on the volume element $\Delta V$:

$$\frac{\mathrm{d}\mathbf{\Delta p}}{\mathrm{d}t} = \int_{\Delta V} \mathbf{F_b}\, \mathrm{d}V + \int_{\delta(\Delta V)} \boldsymbol{\sigma}\, \mathrm{d}A. \tag{4}$$

Examples of body forces are gravity, with $\mathbf{F_b} = \rho g \hat{\mathbf{z}}$ and the electrostatic force $q\boldsymbol{\mathcal{E}}$, where $g$ is the gravitational acceleration, $q$ is the charge density, and $\boldsymbol{\mathcal{E}}$ is the local electric field. Using the Green-Gauss theorem, the integral over the boundary of the element can be converted into an integral over the volume: $\int_{\delta(\Delta V)} \boldsymbol{\sigma}\, \mathrm{d}A = \int_{\Delta V} \partial \sigma_{ij}/\partial x_i \cdot \hat{\mathbf{x}}_i\, \mathrm{d}V$. Eq. 4 should hold for *any* element because so far nothing has been specified about the shape or size of the element. This then yields Cauchy's first law of motion [136]:

$$\rho \ddot{u}_j = \frac{\partial \boldsymbol{\sigma}_{ij}}{\partial x_i} + F_{b,j}. \tag{5}$$

A similar analysis for the angular momentum yields Cauchy's second law of motion: $\sigma_{ij} = \sigma_{ji}$. With these equations (and boundary conditions) the stress distribution can be calculated for a given applied force profile $\mathbf{F_b}(x, y, z)$.

### *2.2. Elasticity*

The stress tensor gives the forces acting inside the material, whereas the strain tensor describes the local deformation of the material. These two quantities are, of course, related to each other. When the deformations are not too large, the stress and strain tensor are related linearly via the the fourth-rank elasticity tensor $\mathbf{E}$:

$$\sigma_{ij} = E_{ijkl}\gamma_{kl} \tag{6}$$

The properties of the stress and strain tensor imply that $E_{ijkl} = E_{jikl} = E_{ijlk} = E_{klij}$, so $\mathbf{E}$ has at most 21 independent elements out of a total of $3 \times 3 \times 3 \times 3 = 81$ elements. This makes it possible to express Eq. 6 in a convenient matrix representation:

$$\begin{bmatrix} \sigma_{xx} \\ \sigma_{yy} \\ \sigma_{zz} \\ \sigma_{xz} \\ \sigma_{yz} \\ \sigma_{xy} \end{bmatrix} = \begin{bmatrix} E_{xxxx} & E_{xxyy} & E_{xxzz} & E_{xxxz} & E_{xxyz} & E_{xxxy} \\ E_{xxyy} & E_{yyyy} & E_{yyzz} & E_{yyxz} & E_{yyyz} & E_{yyyx} \\ E_{xxzz} & E_{yyzz} & E_{zzzz} & E_{zzzx} & E_{zzzy} & E_{zzxy} \\ E_{xxxz} & E_{yyxz} & E_{zzzx} & E_{xzzx} & E_{xzzy} & E_{yxxz} \\ E_{xxyz} & E_{yyyz} & E_{zzzy} & E_{xzzy} & E_{yxxz} & E_{xyyz} \\ E_{xxxy} & E_{yyyx} & E_{zzxy} & E_{yxxz} & E_{xyyz} & E_{xyyx} \end{bmatrix} \begin{bmatrix} \gamma_{xx} \\ \gamma_{yy} \\ \gamma_{zz} \\ 2\gamma_{xz} \\ 2\gamma_{yz} \\ 2\gamma_{xy} \end{bmatrix}, \tag{7}$$

or in short hand notation[5]: $[\sigma] = [E][\gamma]$. The inverse of the elasticity tensor is called the compliance tensor $\mathbf{C}$, which expresses the strain in terms of the stress:

$$\gamma_{ij} = C_{ijkl}\sigma_{kl}, \text{or } [\gamma] = [C][\sigma]. \tag{8}$$

The number of independent elements of $\mathbf{E}$ is further reduced when the crystal structure of the material has symmetries [15, 137, 138]. The most drastic example is an isotropic material, whose properties are the same in all directions. In this

[5]Note that there are three different notations for the elasticity tensor: $\mathbf{E}$ is the actual *tensor* with *elements* $E_{ijkl}$. Finally, the elements can also be written in a *matrix* $[E]$.

Table 3: Mechanical properties of materials that are used in nanomechanical devices. Most materials have a density $\rho$ around $3 \cdot 10^3\,\mathrm{kg/m^3}$ and a Young's modulus of the order of $10^2$ GPa. The carbon-based materials graphite and diamond are slightly lighter, but much stiffer. Compiled from Refs. [15] and [140].

| Material | $\rho$ ($10^3\,\mathrm{kg/m^3}$) | $E$ (GPa) | $\nu$ |
|---|---|---|---|
| Silicon | 2.33 | 130.2 | 0.28 |
| $Si_3N_4$ | 3.10 | 357 | 0.25 |
| SiC | 3.17 | 166.4 | 0.40 |
| $SiO_2$ (crystaline) | 2.65 | 85.0 | 0.09 |
| $SiO_2$ (amorphous) | 2.20 | $\sim 80$ | 0.17 |
| Diamond | 3.51 | 992.2 | 0.14 |
| Graphite (in-plane) | 2.20 | 920 | 0.052 |
| Graphite (out-of-plane) | 2.20 | 33 | 0.076 |
| Aluminum | 2.70 | 63.1 | 0.36 |
| Gold | 19.30 | 43.0 | 0.46 |
| Platinum | 21.50 | 136.3 | 0.42 |
| Niobium | 8.57 | 151.5 | 0.35 |
| GaAs | 5.32 | 85.3 | 0.31 |
| InAs | 5.68 | 51.4 | 0.35 |

case, only two independent parameters remain: the Young's modulus $E$ and Poisson's ratio $\nu$. The compliance matrix is in this case given by:

$$[C] = \begin{bmatrix} 1/E & -\nu/E & -\nu/E & 0 & 0 & 0 \\ -\nu/E & 1/E & -\nu/E & 0 & 0 & 0 \\ -\nu/E & -\nu/E & 1/E & 0 & 0 & 0 \\ 0 & 0 & 0 & 1/G & 0 & 0 \\ 0 & 0 & 0 & 0 & 1/G & 0 \\ 0 & 0 & 0 & 0 & 0 & 1/G \end{bmatrix} \qquad G = \frac{E}{2+2\nu}, \tag{9}$$

where $G$ is the shear modulus. By inverting $[C]$, the elasticity matrix is obtained:

$$[E] = \frac{1}{(1+\nu)(1-2\nu^2)} \begin{bmatrix} E(1-\nu) & E\nu & E\nu & 0 & 0 & 0 \\ E\nu & E(1-\nu) & E\nu & 0 & 0 & 0 \\ E\nu & E\nu & E(1-\nu) & 0 & 0 & 0 \\ 0 & 0 & 0 & G & 0 & 0 \\ 0 & 0 & 0 & 0 & G & 0 \\ 0 & 0 & 0 & 0 & 0 & G \end{bmatrix}. \tag{10}$$

When a plane stress $\sigma_{xx}$ is applied, a material will be stretched in the x-direction, as illustrated in Fig. 4b. The resulting strain $\gamma_{xx} = \sigma_{xx}/E$ induces stress in the y- and z-directions, which are nulled by a negative strain (i.e., contraction) in these directions that is $\nu$ times smaller than the strain in the x-direction. This follows directly from the structure of the compliance matrix. In the opposite situation where a plane strain is applied, the stress can directly be calculated using the elasticity matrix, Eq. 10 [136]. The Young's modulus and Poisson's ratio of materials that are frequently used for nanomechanical devices are indicated in Table 3. The Young's modulus of most semiconductors (Si, GaAs, InAs), insulators ($Si_3N_4$, SiC, $SiO_2$) and metals is of the order of 100 GPa. This is much larger than the values for soft materials such as polymers (typically between 0.1 and 1 GPa) which have also been used for nanomechanical devices [139], but still smaller than that of diamond and graphite. Their Young's modulus of slightly less than 1 TPa combined with a low mass density makes these carbon-based materials ideal to build high-frequency resonators. Also, the large spread in the mass density of the metals should be noted.

For non-isotropic materials, the Young's modulus and Poisson's ratio depend on the direction of the applied stress and are defined as: $E_i = 1/C_{iiii}$ and $\nu_{ij} = -C_{iijj}/C_{iiii}$ $(i \neq j)$ [141]. Graphite is highly anisotropic, and its mechanical properties are important for studying many carbon-based nanomechanical devices. It consists of layers of carbon atoms that are stacked on top of each other (see Fig. 3b and 5b) with an inter-layer spacing $c = 0.335\,\mathrm{nm}$ [142]. The individual layers are called graphene sheets. The unit cell of graphene consists of a hexagon with a carbon atom on each corner, as illustrated in Fig. 5a. Each of the six carbon atoms lies in three different unit cells; a single unit cell thus contains two carbon atoms. The sides of the hexagon have a length $d_{cc} = 0.14\,\mathrm{nm}$, so that the unit cell has an area of $5.22 \cdot 10^{-20}\,\mathrm{m^2}$, and the two-dimensional mass density is $\rho_{2d} = 6.8 \cdot 10^{-7}\,\mathrm{kg/m^2}$ . The graphene planes are not located exactly above each other but every other layer is shifted by half the unit cell, or equivalently, it is rotated by $60^\mathrm{o}$ around an axis through one

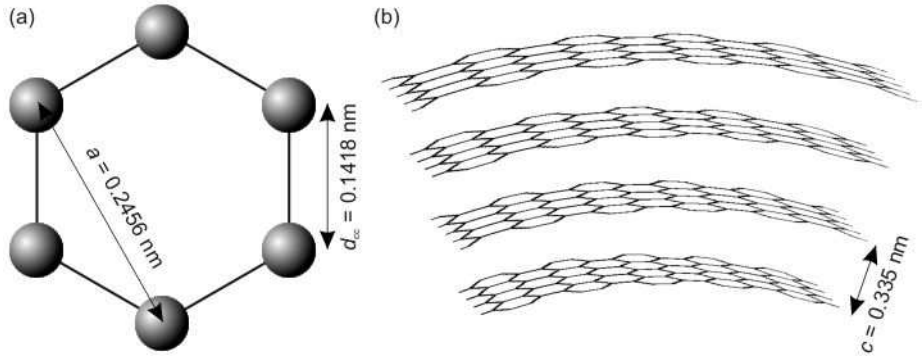


Figure 5: (a) The unit cell of graphene with the dimensions indicated. $a$ is the length of the two translation vectors $\mathbf{a}_{1,2} = \frac{1}{2}a[\pm 1, \sqrt{3}, 0]$, and $d_{cc}$ is the distance between two carbon atoms. The area of the unit cell is $\frac{1}{2}\sqrt{3}a^2 = 5.22 \cdot 10^{-20}\,\mathrm{m}^2$. (b) Bending of a few-layer graphene sheet. The equilibrium distance between the graphene layers is $c = 0.335\,\mathrm{nm}$ [142].

of the carbon atoms. Three of the six atoms are on top of the atoms in the other layer and the other three are located at the center of the hexagon below them. The six-fold rotational symmetry ensures that the elastic properties are the same when looking in any direction along the planes, i.e., they are isotropic in those directions [137, 138]. On the other hand, the mechanical properties for deformations perpendicular to the planes are quite different. It is therefore convenient to introduce the in- and out-of-plane Young's modulus, $E_\square$ and $E_\perp$ respectively, and the corresponding Poisson's ratios $\nu_\square$ and $\nu_\perp$. They are defined such that the compliance matrix is given by[6]:

$$[C] = \begin{bmatrix} 1/E_\square & -\nu_\square/E_\square & -\nu_\perp/E_\perp & 0 & 0 & 0 \\ -\nu_\square/E_\square & 1/E_\square & -\nu_\perp/E_\perp & 0 & 0 & 0 \\ -\nu_\perp/E_\perp & -\nu_\perp/E_\perp & 1/E_\perp & 0 & 0 & 0 \\ 0 & 0 & 0 & 1/G_\square & 0 & 0 \\ 0 & 0 & 0 & 0 & 1/G_\square & 0 \\ 0 & 0 & 0 & 0 & 0 & 1/G_\perp \end{bmatrix}, \tag{11}$$

where[7] $E_\square = 0.92\,\mathrm{TPa}$, $E_\perp = 33\,\mathrm{GPa}$, $G_\square = 1.8\,\mathrm{GPa}$, $G_\perp = 0.44\,\mathrm{TPa}$, $\nu_\square = 0.052$ and $\nu_\perp = 0.076$ [137]. The large in-plane stiffness is the reason that carbon nanotubes and graphene have very high Young's moduli of about 1 TPa, which makes them one of the strongest materials known. Note, that these six elastic constants are not independent as the in-plane shear modulus is given by $G_\square = (E_{1111} - E_{1122})/2$ for a material with hexagonal symmetry.

### *2.3. Energy, bending rigidity and tension*

In the previous Section the relation between the stress and strain in a material was given. Here, we focus on the energy needed to deform the material. From this, the equations of motion are derived. For small deformations, the potential energy $U$ depends quadratically on the strain. It should be invariant under coordinate transformations [136], leading to

$$U = \int_V U' \,\mathrm{d}V \qquad \text{with} \qquad U' = \frac{1}{2} E_{ijkl}\gamma_{ij}\gamma_{kl}, \tag{12}$$

where $U'$ is the potential energy density. From this definition it follows that the stress is given by $\sigma_{ij} = \partial U'/\partial\gamma_{ij}$. For an isotropic material Eq. 12 reduces to [138]:

$$U' = \frac{1}{2}\frac{E}{1+\nu}\left(\gamma_{ij}^2 + \frac{\nu}{1-2\nu}\gamma_{kk}^2\right). \tag{13}$$

Although Eq. 12 is valid for any mechanical system in the linear regime, it is not straightforward to analyze a system this way. Therefore, we focus on two simple and frequently used geometries where the equation of motion can be obtained without too much effort, namely plates and beams.

[6] Note that this definition is slightly different from the conventional definition of the Poisson's ratio in an anisotropic material that was given on page 12.

[7] The values of the elastic constants depend on the quality of the graphite samples. Therefore, slightly different values can be found in the literature. Compare, for example, the data in Refs. [143] and [144] with the values in Ref. [137]

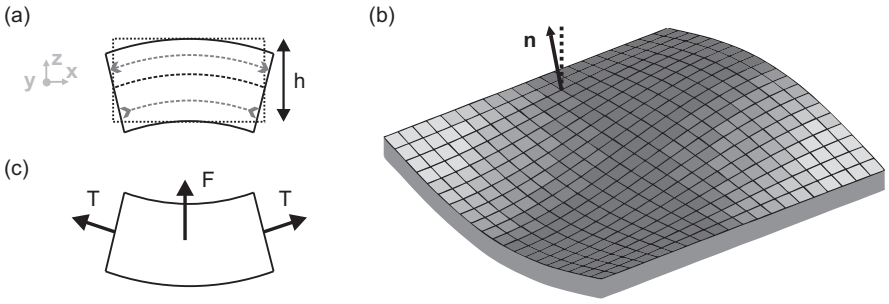


Figure 6: (a) Bending of a plate with thickness $h$. The top part of the plate is extended, whereas the bottom is compressed. The black dashed line indicates the neutral plane. (b) The normal vector of the top surface of a slightly deflected plate makes a small angle with the unit vector $\hat{\mathbf{z}}$ (dotted). (c) If tension $T$ is present in a plate, a net vertical force $\mathbf{F}$ results when the displacement profile has a finite curvature.

*2.3.1. Plates*

A plate is a thin object that is long and wide, i.e., $h \ll \ell \lesssim w$. When a torque is applied to it, it bends, as illustrated in Fig. 6a. The top part, which was initially at $z = h/2$, is extended whereas the bottom part of the beam, originally at $z = -h/2$, is compressed. There is a plane through the plate where the longitudinal strain is zero: the so-called neutral plane. The vertical displacement of this plane is indicated by $u(x, y)$ and for small deflections it lies midway through the plate [138], which we take at $z = 0$. Because of the small deflection and small thickness this is called the thin-plate approximation.

Consider the top (or bottom) face of the plate that is shown in Fig. 6b: because there is no material above (below) that surface, there cannot be a normal force $\mathbf{F_n}$ at this surface (except at the clamping points). In other words, the perpendicular stress components vanishes: $F_{n,i} = \sigma_{ij} n_j = 0$. For a thin plate, the normal vector $\mathbf{n}$ at the top and bottom face points in the z-direction i.e., $\mathbf{n} = \pm\hat{\mathbf{z}}$ to first order in the displacement $u$ or, equivalently, in the radius of curvature $R_c^{-1}$. The condition for vanishing stress thus becomes: $\sigma_{xz} = \sigma_{yz} = \sigma_{zz} = 0$ at the faces. This not only holds at the faces but also inside the material because the plate is thin and the stress cannot build up. For an isotropic material the displacement and strain fields that satisfy these requirements are [138]:

$$\begin{aligned} u_x = &\quad -z \cdot \partial u/\partial x, &\quad \gamma_{xx} &= -z \cdot \partial^2 u/\partial x^2 \\ u_y = &\quad -z \cdot \partial u/\partial y, &\quad \gamma_{yy} &= -z \cdot \partial^2 u/\partial y^2 \\ u_z = &\quad u, &\quad \gamma_{zz} &= z\nu/(1-\nu) \cdot \nabla^2 u \\ \gamma_{xz} = &\quad \gamma_{yz} = 0, &\quad \gamma_{xy} &= -z \cdot \partial^2 u/\partial x \partial y. \end{aligned} \tag{14}$$

The vertical displacement of the material $u_z$ is thus equal to the deflection $u$ for every value of $z$. Besides this vertical displacement there is also a horizontal displacement ($u_x$ and $u_y$) induced when $u$ changes. In that case, the material displaces in different directions above and below the neutral plane (Fig. 6a) as expressed by the proportionality with $z$. Moreover, the strain components averaged over the thickness $h$, $\overline{\gamma}_{ij}(x, y)$, are all zero, as the contributions above and below the neutral plane cancel each other.

To proceed, Eq. 14 is inserted into Eq. 13 and the integration over $z$ in Eq. 12 is carried out. This yields the energy needed to bend the plate:

$$U_B = \frac{Eh^3}{24(1-\nu^2)} \iint \left[ \left( \frac{\partial^2 u}{\partial x^2} + \frac{\partial^2 u}{\partial y^2} \right)^2 + 2(1-\nu) \left( \left\{ \frac{\partial^2 u}{\partial x \partial y} \right\}^2 - \frac{\partial^2 u}{\partial x^2} \frac{\partial^2 u}{\partial y^2} \right) \right] \mathrm{d}x\,\mathrm{d}y \tag{15}$$

It is possible that the plate is not only bent, but that it is also under a longitudinal tension $\mathbf{T} = \int \boldsymbol{\sigma}\, \mathrm{d}z$ (positive for tensile tension, negative for compressive tension). The tension is tangential to the surface and from Fig. 6c it is clear that the longitudinal tension results in a restoring force in the z-direction when the plate is bent, i.e., when $\partial^2 u/\partial x^2 \neq 0$. The tension deforms the plate, as indicated in Fig. 4b. The displacement results in a strain field $\overline{\gamma}_{\alpha\beta} = \frac{1}{2}(\partial \overline{u}_\beta/\partial x_\alpha + \partial \overline{u}_\alpha/\partial x_\beta + \partial \overline{u}/\partial x_\alpha \cdot \partial \overline{u}/\partial x_\beta)$, where Greek indices run over the x and y coordinate only. Using Eq. 12 the work done by applying the tension is calculated. The resulting stretching energy is:

$$U_T = \frac{1}{2} \iint \gamma_{\alpha\beta} T_{\alpha\beta}\, \mathrm{d}x\,\mathrm{d}y, \text{ where } T_{\alpha\beta} = \int_{-h/2}^{h/2} \sigma_{\alpha\beta}\, \mathrm{d}z \equiv h\overline{\sigma}_{\alpha\beta}. \tag{16}$$

The equation of motion for the vertical deflection of the plate is obtained when the variation of the total potential energy $U = U_B + U_T + U_F$ is considered ($U_F = -\iint Fu\, \mathrm{d}x\,\mathrm{d}y$ includes the effect of an external force per unit area $F$ in the

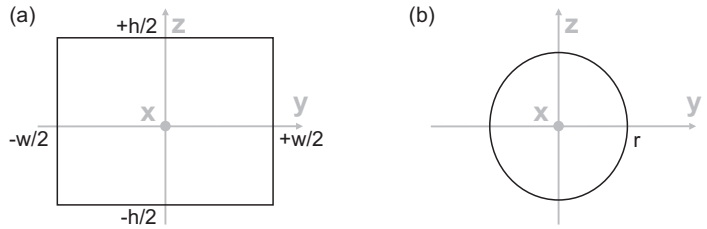


Figure 7: Cross-sections of a rectangular beam with thickness $h$ and width $w$ (a) and a cylindrical beam with radius $r$ (b).

z-direction) for an arbitrary variation in the displacement $u \to u + \delta u$. This yields the equation of motion for the plate [138]:

$$\rho h \frac{\partial^2 u}{\partial t^2} + \left( D\nabla^4 - \frac{\partial}{\partial x_\alpha} T_{\alpha\beta} \frac{\partial}{\partial x_\beta} \right) u(x,y) = F(x,y), \tag{17}$$

where $\rho$ is the mass density of the material[8]. The first term in Eq. 17 is the inertial term and the last term is the external force acting on the plate. The term in brackets is the force resulting from the deformation of the plate. Here, $D = Eh^3/12(1-\nu^2)$ is the so-called bending rigidity of the plate, the prefactor in Eq. 15 that quantifies how much energy it costs to bend a unit area of the plate. The tension makes Eq. 17 nonlinear as a displacement of the plate elongates it and thereby induces tension, i.e. $T_{\alpha\beta} = T_{\alpha\beta}[u(x',y')](x,y)$. However, for small deformations the displacement-induced tension is small and will be overwhelmed by the bending rigidity or by tension induced by the clamping. Then the tension is independent of $u$ and Eq. 17 is linear.

*2.3.2. Beams*

Table 1 shows that many nanomechanical devices are doubly-clamped beams or cantilevers instead of plates i.e., they have a width that is much smaller then their length. For a beam, the normal components of the stress on the sides should also vanish, i.e., $\sigma_{yy} = \sigma_{xy} = 0$ and the integration of Eq. 12 over $y$ can be done directly. This implies that the tension $T_{\alpha\beta}$ is only in the x-direction. Moreover, the material displaces in the x-direction so that $T = T_{xx}$ is independent of $x$. Combining all of this yields the equation of motion in the "thin-beam" approximation: the Euler-Bernoulli equation with tension:

$$\rho A \frac{\partial^2 u}{\partial t^2} + D \frac{\partial^4 u}{\partial x^4} - T \frac{\partial^2 u}{\partial x^2} = F, \tag{18}$$

where the crosssection area $A$ equals $wh$ for a rectangular beam and for a cylindrical beam $A = \pi r^2$ (see Fig. 7). The structure of Eq. 18 is similar to that of the the equation of motion for a plate, Eq. 17. The first term is the acceleration and the term on the right-hand side is the external force. The restoring force due to the bending stiffness depends on the fourth order derivative of the displacement w.r.t. $x$. For the tension, this is a second-order derivative. The bending rigidity[9] $D = Eh^3w/12(1-\nu^2)$ can be written as the product of the Young's modulus and the second moment of inertia $D = EI/(1-\nu^2)$, where the small correction $(1-\nu^2)$ is often omitted [15]. For a rectangular beam the second moment of inertia is $I = h^3w/12$; for a (solid) cylinder with radius $r$ it is $I = \pi r^4/4$ [15]. The bending rigidity depends strongly on the dimensions of the device. It can be as small as $10^{-24}\,\mathrm{Nm}^2$ for a carbon nanotube (Sec. 2.4.4) or as large as $10^{-5}\,\mathrm{Nm}^2$ for a millimetre-sized mirror [33].

*2.4. Examples*

*2.4.1. Cantilevers and doubly-clamped beams*

A cantilever is a beam that is clamped on one side ($x = 0$) and free on the other side ($x = \ell$). Because a cantilever is not fixed on the, say, right side, the tension is zero apart from more exotic cases where electrostatic forces [74, 80] or surface tension [145, 146] acts on the free end. With $T = 0$, the eigenmodes $u_n$ and (angular) eigenfrequencies $\omega_n$ satisfy:

$$\omega_n^2 \rho A u_n = D \frac{\partial^4 u_n}{\partial x^4}. \tag{19}$$

The solution to this equation is a linear combination of the regular and hyperbolic sine and cosine functions ($\sin(kx)$, $\cos(kx)$, $\sinh(kx)$, and $\cosh(kx)$ resp.), where $k^4 = \omega^2 D/\rho A$. Their coefficients are determined by the boundary conditions.

[8] In principle, the first term should read $\rho h \partial^2 u/\partial t^2 + \rho h^3 \partial/\partial t^2 (\partial^2 u/\partial x^2 + \partial^2 u/\partial y^2)/12$ as the material is also moving in the x and y direction. These corrections are, however, negligible when $h/\ell \ll 1$.

[9] Note that the units of the bending rigidity, tension and external force are different from the case of a plate due to the integration over the y-coordinate. $D$ is given in $\mathrm{Nm}^2$ instead of Nm(= J) and $T$ is now in N instead of N/m. The external force $F$ is given per unit length instead of per unit area. From the context it should be clear what the meaning of the different symbols is.

Table 4: Normalized eigenfrequencies and average mode deflection $\mu_n$ for the first 5 flexural eigenmodes for cantilevers and doubly-clamped beams. $\mu_n = \ell^{-1}\int_0^\ell \xi_n(x)\,\mathrm{d}x$ indicates the displacement of the mode averaged along the length of the resonator per unit deflection. This number is important to calculate the detection efficiency for detectors that couple over the whole length of the beam (p26). $\alpha_n$ and $\beta_n$ are the solutions of Eq. 21 and 18 respectively which determine the eigenfrequencies. For large $n$ the solutions approach $\alpha_n \to (n+1/2)\pi$ and $\beta_n \to (n+3/2)\pi$.

| **Mode** | **Cantilever** | | | **Beam** | | |
|---|---|---|---|---|---|---|
| $n$ | $\alpha_n$ | $f_n/f_0$ | $\mu_n$ | $\beta_n$ | $f_n/f_0$ | $\mu_n$ |
| 0 | 1.875 | 1.000 | 0.783 | 4.730 | 1.000 | 0.831 |
| 1 | 4.694 | 6.267 | 0.434 | 7.853 | 2.757 | 0 |
| 2 | 7.855 | 17.547 | 0.254 | 10.996 | 5.404 | 0.364 |
| 3 | 10.996 | 34.386 | 0.182 | 14.137 | 8.933 | 0 |
| 4 | 14.137 | 56.843 | 0.141 | 17.279 | 13.344 | 0.231 |

At the fixed end, the displacement is zero and the beam is horizontal: $u(0) = 0$ and $u'(0) = 0$, where $'$ denotes differentiation with respect to $x$. At the free end, the force in the z-direction and the torque vanish, so $u''(\ell) = 0$ and $u'''(\ell) = 0$. There are thus four boundary conditions and four unknown coefficients. This system always has a trivial solution $u_n = 0$ where all four coefficients are zero. There are, however, certain values $k = k_n$ where one of the four boundary conditions is automatically satisfied. These values correspond to the eigenmodes of the flexural resonator. Using the other three boundary conditions, three of the coefficients are expressed in the fourth one (which we call $c_4$). For a cantilever we define $\alpha_n \equiv k_n\ell$ and the n-th eigenmode is:

$$u_n(x) = c_4\left(\sin(\alpha_n\frac{x}{\ell}) - \sinh(\alpha_n\frac{x}{\ell}) - \frac{\sin(\alpha_n)+\sinh(\alpha_n)}{\cos(\alpha_n)+\cosh(\alpha_n)}\left[\cos(\alpha_n\frac{x}{\ell}) - \cosh(\alpha_n\frac{x}{\ell})\right]\right). \tag{20}$$

Note, that if $u_n(x)$ is an eigenmode of the cantilever, then $c\cdot u_n(x)$ is one as well, for every value of $c$. In the following part we will therefore use the normalized eigenfunctions $\xi_n$, which satisfy $\ell^{-1}\int_0^\ell \xi_n^2\,\mathrm{d}x = 1$. The eigenfrequencies are given by:

$$\cos(\alpha_n)\cosh(\alpha_n) + 1 = 0, \quad \omega_n = 2\pi f_n \alpha_n^2 \ell^{-2}\sqrt{D/\rho A}. \tag{21}$$

This equation can only be solved numerically. The first few solutions $\alpha_n$ are indicated in Table 4 and Fig. 8b shows the corresponding mode shapes. Unlike in a string under tension, a type of resonator that will be discussed in the next section, which has $f_n/f_0 = (n+1)$, the eigenmodes do not have a harmonic spectrum. Also, the average displacement of the mode, defined as $\mu_n = \ell^{-1}\int_0^\ell \xi_n\,\mathrm{d}x$, decreases with increasing mode number $n$. This is because a part of the cantilever is moving upwards and an other part is moving downwards.

The analysis for the flexural eigenmodes of a doubly-clamped beam, which does not have a free end but which is clamped at both $x = 0$ and $x = \ell$, closely follows that for a cantilever. The difference is that the boundary conditions at $x = \ell$ are now $u(\ell) = 0$ and $u'(\ell) = 0$. With $\beta_n \equiv k_n\ell$ this yields:

$$u_n(x) = c_4\left(\sin(\beta_n\frac{x}{\ell}) - \sinh(\beta_n\frac{x}{\ell}) - \frac{\sin(\beta_n)+\sinh(\beta_n)}{\cos(\beta_n)+\cosh(\beta_n)}\left[\cos(\beta_n\frac{x}{\ell}) - \cosh(\beta_n\frac{x}{\ell})\right]\right), \tag{22}$$

and

$$\cos(\beta_n)\cosh(\beta_n) - 1 = 0, \quad \omega_n = 2\pi f_n = \beta_n^2\ell^{-2}\sqrt{D/\rho A}. \tag{23}$$

Table 4 shows that $\beta_n > \alpha_n$, so that the eigenfrequencies of a clamped-clamped beam are higher than that of a cantilever with the same dimensions. This is because the additional clamping makes it stiffer. Moreover, due to symmetry $\mu_n$ vanishes for the odd modes of a beam. Figure 8 shows the first three mode shapes.

Equations 21 and 23 show that when the resonator is made shorter while its transverse dimensions are kept the same, the eigenfrequencies increase due to the $\ell^{-2}$ term in the characteristic frequency scale $\omega_{ch} \equiv \ell^{-2}\sqrt{D/\rho A}$ [147, 148]. On the other hand, the crosssectional area and the bending rigidity depend on the size of the resonator. The exact scaling is $\omega_{ch} \propto h/\ell^2$ and $\omega_{ch} \propto r/\ell^2$ for a rectangular and cylindrical resonator respectively . When making all dimensions of a resonator smaller [38], the resonance frequencies thus increase inversely proportionally with the size. This scaling is the reason that nanomechanical resonators can have very high resonance frequencies of more than 1 GHz [28].

### *2.4.2. String resonators*

So far we have not considered the effect of tension in the examples of flexural resonators. In certain types of materials there can be so much stress that the bending rigidity hardly contributes to the restoring force. The resonator is then a string under tension instead of a beam. Eq. 18 shows that this is the case when $T \gg D/\ell^2$, or when this is rewritten in the (longitudinal) strain $\gamma$, $\gamma \gg (h/\ell)^2/12$. Tension is thus more important in resonators with a large aspect ratio $\ell/h$.

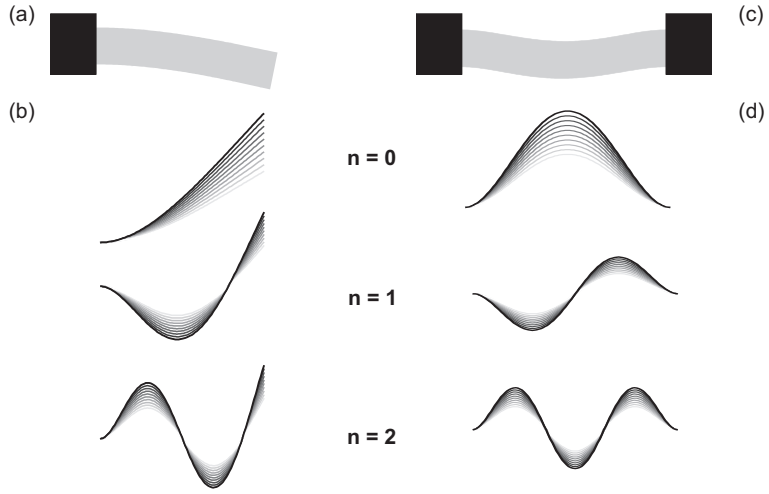


Figure 8: Schematic of a singly-clamped cantilever (a) and a doubly-clamped beam (c). (b) and (d) show the shape of the first three ($n = 0, 1, 2$) flexural modes of these flexural resonators. This shape is calculated using Eqs. 20 and 22 respectively.

The eigenfrequencies of a string under tension are $f_n = \sqrt{T/\rho A} \times (n+1)/2\ell$ and the corresponding modeshapes are $\xi_n(x) = \sqrt{2}\sin(\pi n x/\ell)$.

Tension in the resonator arises when materials with different thermal expansion coefficients or different lattice constants are used. An example of the former is given by Regal *et al.* [50], where a 50 $\mu$m long aluminum beam resonator is annealed at 150 to 350 °C, thereby increasing the resonance frequency from 237 kHz to 2.3 MHz. Stress can also be induced by growing heterostructures with different lattice constants. If the layer with the resonator has a smaller lattice constant that the layer underneath it, then the resonator is strained. By engineering the heterostucture, different amounts of tension can be induced in the resonator [149, 150]. Another way of inducing tension is by placing the resonator on a flexible substrate that can be bent. As the top part of the substrate is elongated, the resonator becomes strained. With this technique, the resonance frequency of a resonator has been tuned by more than a factor 5 [151]. The most commonly used high-stress material is silicon nitride. Under the appropriate growing conditions thin films with stresses of $\sim$ 1 GPa can be obtained [152] and resonators made using this material have extremely high quality factors [153, 154]. Recently, high-stress SiN has therefore become a very popular material for nanomechanical resonators [68, 57, 69, 151, 72]. Another important type of string resonators are suspended carbon nanotubes. Since in this system the displacement can readily be of the same order as the radius of the tube, nonlinear effects are important. These systems will be treated in Sec. 2.4.4.

Although high $Q$-values seem to be a general observation for strained beams, the mechanism behind the increase is not completely clear. Recall that the Q-factor is proportional to the ratio between the energy stored in the oscillator and the energy dissipated per cycle. Supported by experiments, the authors in Ref [72] demonstrate that stress does not substantially change the dissipation rate in strained beam mechanical oscillators but rather significantly increases the elastic energy stored in the resonator. They argue that the microscopic origin of the damping lies in localized defect states in the material. In the abovementioned experiments by Regal *et al.* the quality factor of an aluminum beam resonator was increased by a factor 50 by annealing it [50]. Although the induced tension also increased the resonance frequency by a factor 10, the quality factor increased more. This means that in this case the annealing did not just increase the energy in the resonator, but it actually reduced the damping rate ($\gamma_R = \omega_R/Q$), which is the ratio of the resonance frequency $\omega_R$ and the quality factor. Also in this system the physical mechanism behind this remarkable increase is still unclear.

### *2.4.3. Buckled beams*

In the case of a string resonator the tension is tensile, i.e., the resonator is elongated. It is also possible that the resonator is compressed. In that case, the tension is negative. When the tension exceeds a critical value, it is energetically favorable for the beam to have a non-zero flexural displacement; the beam buckles. Buckled beams form an important class of (nano)mechanical resonators, and can be formed when the resonator consists of layers of different materials [155, 156, 19], or using thermal expansion [18].

The starting point for the analysis of buckled beams is the Euler-Bernoulli beam equation (Eq. 18) with no external force, i.e., $F = 0$. The boundary conditions are the same as for a doubly-clamped beam: $u(0) = u(\ell) = 0$ and $u'(0) = u'(\ell) = 0$ [19, 157]. The negative tension has two contributions: first the beam is compressed by the fact that it is clamped. Figure 9a shows that the length of the free beam ($\ell_0$) and that of the clamped beam ($\ell$) are different when the clamping point exert a longitudinal tension on the beam. This is the so-called residual tension, $T_0 = EA\gamma_0$, with $\gamma_0 = (\ell - \ell_0)/\ell_0$.

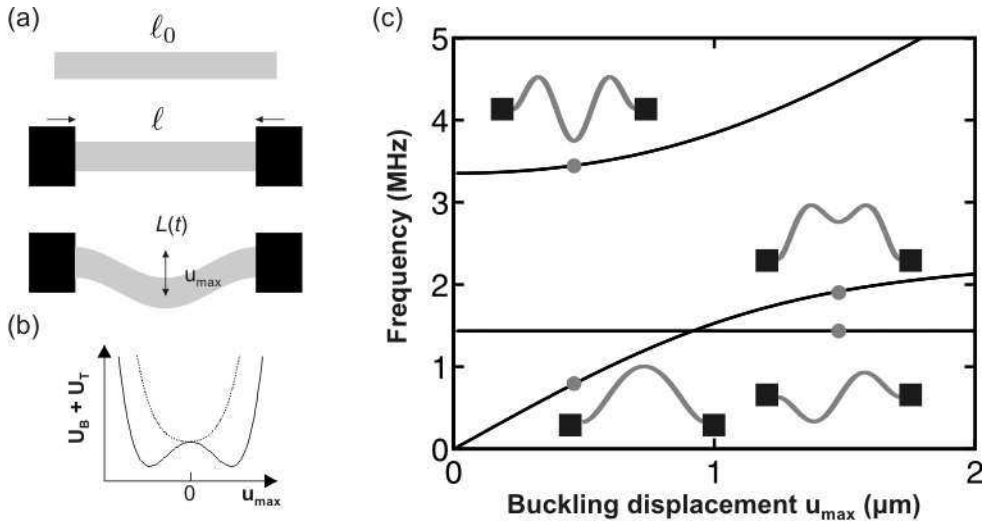


Figure 9: (a) The distance between the clamping points $\ell$ of a doubly clamped beam differs from the length of the free beam $\ell_0$. If the induced tension is large enough, it is energetically favorable for the beam to displace, releasing strain energy at the cost of bending energy. This is called buckling. Due to the displacement $u(x)$ the length of the beam is extended to $L(t)$. (b) The total potential energy $U_T + U_B$ for a beam below (dotted) and above (solid) the buckling threshold. In the former case the potential energy only has a single minimum at $u_{\max} = 0$, whereas the latter has two minima at non-zero deflection. (c) An example of the calculated eigenfrequencies of a 50 $\mu$m-long beam with $D = 3.20 \cdot 10^{-15}$ J [19]. The mode shapes at the position of the dots are shown.

The second, positive, contribution comes from the stretching of the beam when it flexures. The resulting length of the flexed beam is denoted by $L = \int_0^\ell \{1 + (\partial u/\partial x)^2\}^{1/2}\,\mathrm{d}x$. Combining both effects gives for small ($\partial u/\partial x \ll 1$) deflections:

$$T \approx T_0 + \frac{EA}{2\ell}\int_0^\ell \left(\frac{\partial u}{\partial x}\right)^2 \mathrm{d}x. \tag{24}$$

In the absence of driving, both the displacement and the tension are time-independent and the static deflection $u_{\mathrm{dc}}$ satisfies:

$$D\frac{\partial^4 u_{\mathrm{dc}}}{\partial x^4} - T_{\mathrm{dc}}\frac{\partial^2 u_{\mathrm{dc}}}{\partial x^2} = 0, \quad \text{with} \quad T_{\mathrm{dc}} = T_0 + \frac{EA}{2\ell}\int_0^\ell \left(\frac{\partial u_{\mathrm{dc}}}{\partial x}\right)^2 \mathrm{d}x. \tag{25}$$

This only has a non-trivial solution $u_{\mathrm{dc}} \neq 0$ when $T_{\mathrm{dc}} = n^2 T_c$, where $T_c = -4\pi^2 D/L^2$ is the critical tension at which the beam buckles and $n$ is an integer. The solution is then $u_{\mathrm{dc}}(x) = u_{\max}[1 - \cos(2\pi n x/\ell)]/2$. When an initially unstrained beam is compressed slightly, work is done and the energy stored in $U_T$ increases. The potential energy has a single minimum around $u_{\max} = 0$ in this case; see the dotted line in Fig. 9b. When the compressive residual tension $T_0$ is made more negative than $T_c$, it becomes energetically favorable for the beam to convert a part of $U_T$ into the bending energy $U_B$. The potential energy now has two minima at non-zero static displacements, as illustrated by the solid line in Fig. 9b. The beam buckles to a displacement that keeps the tension exactly at $T_c$ (for $n$=1). The value of the displacement depends on the residual tension that caused it: $u_{\max} = \pm 2\ell/\pi \cdot ([T_c - T_0]/EA)^{1/2}$ for $T_0 \leq T_c < 0$. Note, that in the absence of a static force, the beam does not have a preferential direction of buckling.

To find the eigenmodes of the buckled beam, we do not only focus on the static deflection, but we also include the dynamics of the displacement. When driving the modes of the beam, the total deflection $u$ is the sum of the static ($u_{\mathrm{dc}}$) and an oscillating part ($u_{\mathrm{ac}}$). The time-dependent displacement satisfies:

$$\rho A\frac{\partial u_{\mathrm{ac}}^2}{\partial t^2} + D\frac{\partial^4 u_{\mathrm{ac}}}{\partial x^4} - T_{\mathrm{dc}}\frac{\partial^2 u_{\mathrm{ac}}}{\partial x^2} = T_{\mathrm{ac}}\frac{\partial^2 u_{\mathrm{dc}}}{\partial x^2}, \tag{26}$$

with:

$$T_{\mathrm{ac}} = \frac{EA}{\ell}\int_0^\ell \frac{\partial u_{\mathrm{dc}}}{\partial x}\frac{\partial u_{\mathrm{ac}}}{\partial x}\,\mathrm{d}x. \tag{27}$$

Note, that both sides of Eq. 26 are linear in $u_{\mathrm{ac}}$ and that the static displacement $u_{\mathrm{dc}}$ thus acts as an effective spring constant for ac motion, as indicated by the r.h.s. of Eq. 26. The eigenfrequencies of buckled beams were calculated by Nayfeh *et al.* [157]. As an example the eigenfrequencies and modes for the beam used in Ref. [19] are shown in Fig. 9b. At zero buckling the frequency of the fundamental mode is zero as the potential energy is quartic in the displacement: the quadratic terms in $U_B$ and $U_T$ cancel each other exactly. The frequency of the fundamental mode increases with

increasing buckling due to the contribution of $T_{\rm ac}$. The first higher mode has an eigenfrequency $\omega_1/2\pi = 1.44\,$MHz and is independent of $u_{\rm max}$, as the mode is anti-symmetric around the node, giving $T_{\rm ac} = 0$. When $u_{\rm max}$ is increased to $0.92\,\mu$m, the two lowest modes cross and the fundamental mode is higher in frequency than the first odd mode.[10] Thus, when the length of the beam, bending rigidity and the buckling displacement are known, the eigenfrequencies and modeshapes of a buckled beam can be calculated.

*2.4.4. Nanobeams*

In Sec. 2.4.2 we showed that tension can overwhelm the influence of bending rigidity in nanomechanical devices with high aspect ratios. For these thin wires the displacement can be of the order of the resonator thickness and in this case nonlinear effects connected with the deflection-induced tension become important. Suspended carbon nanotubes resonators are prototypical examples where the induced tension can be so large that the tubes are tuned from bending (beam-like) to tension dominated (string-like) [20, 158].

The induced tension is a key feature of thin resonators as it can be used to electrically tune their frequency over a large range. In this Subsection we derive the equations for the frequency tuning and give some typical numbers for single-wall CNTs. We will start with considering the device geometry of a suspended CNT resonator and derive some of the basic equations describing the electrostatics of the problem. The analysis is, however, also applicable to other thin string-like resonators such as multi-wall CNTs, suspended graphene nanoribbons, or long suspended nanowires made from inorganic materials (see Table 2).

Fig. 10a shows an atomic force microscope image of a suspended single-wall carbon nanotube in a three terminal geometry [159]. The nanotube is connected to source and drain electrodes, enabling electrical transport measurements. The tube is suspended above a gate electrode at a distance $h_{\rm g}$, which cannot only be used to change the electrostatic potential on the tube, but also to drive the resonator [160] and to induce tension. An electrostatic force can be applied to the tube by applying a voltage $V_{\rm g}$ between a gate electrode (Fig. 10b) and the nanotube. The potential energy[11] depends on the capacitance between the tube and the gate $C_{\rm g}$, and is $U_F = -C_{\rm g}V_{\rm g}^2/2$. The potential energy depends on the distance between the gate and the tube $h_{\rm g} - u(x)$ via the gate capacitance, which means that there is a force acting acting on the nanotube. The electrostatic potential energy is written as: $U_F = -\int_0^\ell c_g(x)V_{\rm g}^2/2\,{\rm d}x$, where $c_g(x)$ is the capacitance per unit length, and the potential energy equals by definition $U_F = -\int_0^\ell Fu\,{\rm d}x$. The electrostatic force per unit length is thus $F(t) = \frac{1}{2}\partial c_g/\partial u V_{\rm g}^2$.

To calculate the displacement dependence of the capacitance, we first consider the spatial profile of the electrostatic potential. Under the assumption that the screening effect of the source and drain electrodes is negligible, the tube is viewed as an infinitely long grounded solid cylinder, suspended above a conducting plate at an electrostatic potential $\phi(z = 0) = V_{\rm g}$. The potential profile for $u = 0$ is given by [162]:

$$\phi(y,z) = V_g - V_g \frac{1}{\operatorname{arccosh}(h_{\rm g}/r)} \ln\left(\frac{\left[z + \sqrt{h_{\rm g}^2 - r^2}\right]^2 + y^2}{\left[z - \sqrt{h_{\rm g}^2 - r^2}\right]^2 + y^2}\right). \tag{28}$$

The field lines associated with this potential are shown in Fig. 10b. The deflection of the nanotube is included by replacing $h_{\rm g}$ with $h_{\rm g} - u$. After dividing the induced charge by the gate voltage, the capacitance per unit length $c_g(x)$ is obtained[12]:

$$c_g(x) = \frac{2\pi\epsilon_0}{\operatorname{arccosh}\big([h_{\rm g} - u(x)]/r\big)} \approx \frac{2\pi\epsilon_0}{\operatorname{arccosh}\big(h_{\rm g}/r\big)} + \frac{2\pi\epsilon_0}{\sqrt{h_{\rm g}^2 - r^2}\,\operatorname{arccosh}^2\big(h_{\rm g}/r\big)}u(x). \tag{29}$$

The approximation in Eq. 29 is allowed because the displacement $u$ is typically much smaller than $h_{\rm g}$. This in contrast to top-down fabricated devices, where higher order terms can be important and electrostatic softening of the spring constant might occur [163, 57]. This softening is thus due to nonlinear capacitance terms, which should be contrasted to the nonlinearities due to the displacement-induced tension that we will discuss further on in this Section. For thin resonators under high built-in tension, however, the nonlinear capacitance terms can become relevant again. This has been nicely illustrated in graphene resonators, which show a small downward shift in the frequency around zero-gate voltage [104]. We will not consider these effects in the following, but we finally note that the electrical softening is closely related to the optical spring that will be discussed in Sec. 3.5.3.

[10] The modes are classified by their shape and not by the ordering of eigenfrequencies. The fundamental mode is the mode without a node.

[11] This is the potential energy for the tube, in contrast to the energy stored in the capacitor: $+C_{\rm g}V_{\rm g}^2/2$. The difference in the sign is because the voltage source performs work when the capacitance changes [161], which should also be taken into account.

[12] This expression might appear different from those in Refs [135] and [158], but note that $\operatorname{arccosh}(x) = \ln(x + \sqrt{x^2 - 1}) \approx \ln(2x)$ for $x \gg 1$.

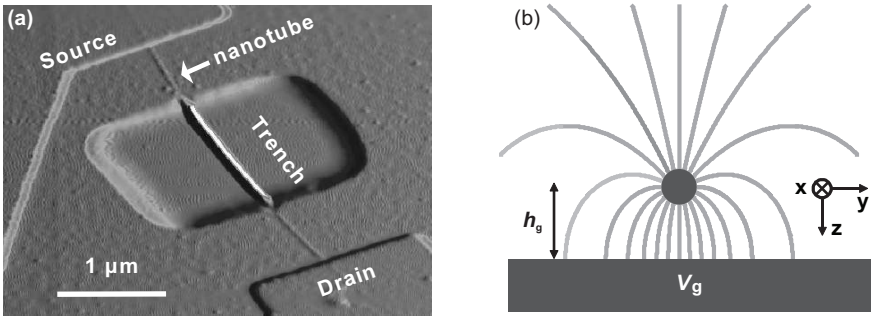


Figure 10: (a) an AFM image of a suspended nanotube device connected to the source and drain electrode. The tube is suspended above the trench only. The suspended part of this device is $\ell = 1.25\,\mu$m long and the radius of the tube is $r = 1.4$ nm. (b) Field lines of the electrostatic potential induced by the gate electrode. When the distance between the tube and the gate $h_g$ changes, the gate capacitance $C_g$ changes.

The electrostatic force per unit length is now:

$$F(t) = \frac{1}{2}\frac{\partial c_g}{\partial u}V_{\rm g}^2(t) = \frac{\pi\epsilon_0 V_{\rm g}^2(t)}{\sqrt{h_{\rm g}^2 - r^2}\,\operatorname{arccosh}^2\left(h_{\rm g}/r\right)}. \tag{30}$$

Often, the gate voltage consists of two parts: a static part $V_{\rm g}^{\rm dc}$ and a time-dependent part $V_{\rm g}^{\rm ac}\cos(\omega t)$ to drive the nanotube at frequency $f = \omega/2\pi$. The experimental condition $V_{\rm g}^{\rm ac} \ll V_{\rm g}^{\rm dc}$ ensures that terms proportional to $(V_{\rm g}^{\rm ac})^2$ are negligible. The force is then the sum of a static and driving contribution: $F = F_{\rm dc} + F_{\rm ac}\cos(\omega t)$, with $F_{\rm dc} = \pi\epsilon_0/(h_{\rm g}^2 - r^2)^{1/2}\operatorname{arccosh}^2\left(h_{\rm g}/r\right)\cdot(V_{\rm g}^{\rm dc})^2$ and $F_{\rm ac}(t) = \pi\epsilon_0/(h_{\rm g}^2 - r^2)^{1/2}\operatorname{arccosh}^2\left(h_{\rm g}/r\right)\cdot 2V_{\rm g}^{\rm dc}V_{\rm g}^{\rm ac}(t)$.

The bending mode vibrations are described by the Euler-Bernoulli beam equation with tension included, i.e., Eq. 18. When the amplitude of the oscillation $u_{\rm ac}$ is small compared to the larger of the tube's radius and the static displacement, terms proportional to $u_{\rm ac}^2$ are negligible and the tube is in the linear regime[13]. Similar to the analysis presented for the buckled beams, the equation of motion (Cf. Eq. 18) is separated:

$$D\frac{\partial^4 u_{\rm dc}}{\partial x^4} - T_{\rm dc}\frac{\partial^2 u_{\rm dc}}{\partial x^2} = F_{\rm dc}, \tag{31}$$

$$-\omega^2\rho A u_{\rm ac} + i\omega\gamma u_{\rm ac} + D\frac{\partial^4 u_{\rm ac}}{\partial x^4} - T_{\rm dc}\frac{\partial^2 u_{\rm ac}}{\partial x^2} - T_{\rm ac}\frac{\partial^2 u_{\rm dc}}{\partial x^2} = F_{\rm ac}. \tag{32}$$

The first equation describes the static displacement of the tube that is induced by the dc gate voltage. This equation is independent of $u_{\rm ac}$. On the other hand, the ac displacement, given by Eq. 32, depends on the static displacement and also on the static tension $T_{\rm dc}$. Similar to the case of the buckled beam, the static tension has two contributions, as indicated by Eq. 25: The first one is the residual tension due to the clamping as the length of the suspended part is not necessarily equal to the length when it would not be clamped. For example, a nanotube resonator could be strained during the growth process or lay slightly curved on the substrate before suspending it. The second contribution is the displacement-induced tension: The gate electrode pulls the resonator towards it, thereby elongating it. Moreover, the oscillator experiences a time-dependent variation in its length and $T_{\rm ac}$ is the part of the tension that is linear in $u_{\rm ac}$. Both effects are included in Eq. 32. As the tension contains the static displacement, it has to be solved self-consistently [158, 135, 159] with Eq. 31 to find the static displacement. The resulting static tension, ac tension and dc displacement are then inserted into Eq. 32 to find the eigenfrequencies $\omega_n$ and the response function $u_{\rm ac}(x,\omega)$ [164].

To analyze the system of Eqs. 24, 31 and 32, it is useful to take a closer look at their scaling behavior [135]. In this section, we use the convention that primed variables indicate scaled (dimensionless) variables. An obvious way to normalize the coordinate $x$ is to divide it by the tube length: $x' = x/\ell$, so that the equation for the static displacement Eq. 31 becomes:

$$\frac{\partial^4 u_{\rm dc}}{\partial x'^4} - \frac{\ell^2 T_{\rm dc}}{D}\frac{\partial^2 u_{\rm dc}}{\partial x'^2} = \frac{\ell^4 F_{\rm dc}}{D} \equiv l_{\rm dc}. \tag{33}$$

On the right hand side, a natural length scale for the static displacement, $l_{\rm dc}$, appears. However, scaling the displacement with $l_{\rm dc}$ is not handy because $l_{\rm dc}$ equals zero at zero gate voltage. Therefore $u_{\rm dc}$ (and $u_{\rm ac}$) are scaled by the radius of the tube: $u'_{\rm dc} = u_{\rm dc}/r$. Moreover, the tension has become dimensionless, resulting in an equation for the static displacement where the number of parameters has been reduced from 5 to 2:

$$\frac{\partial^4 u'_{\rm dc}}{\partial x'^4} - T'_{\rm dc}\frac{\partial^2 u'_{\rm dc}}{\partial x'^2} = l'_{\rm dc}, \tag{34}$$

[13]This refers to the dynamical behavior. The static displacement is actually nonlinear when the tube is in the strong bending limit [158].

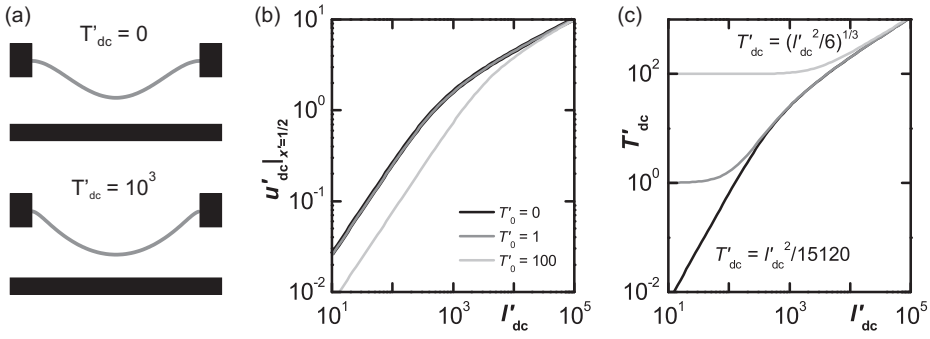


Figure 11: (a) static displacement profiles for $T'_{\rm dc} = 0$ (top), and $T'_{\rm dc} = 10^3$ (bottom). (b,c) The calculated static displacement at the center of the nanotube (b) and the corresponding tension (c) for various value of the residual tension $T'_0$. The limits for the tension for small and large static forces are indicated.

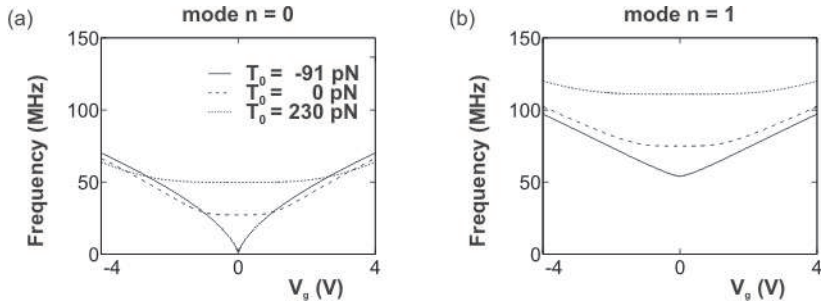


Figure 12: Gate-voltage tuning of the eigenfrequencies of the first (a) and second (b) flexural mode of a $1\,\mu$m-long suspended carbon nanotube (see Table 5). The residual tensions are $T_0 = -91,\ 0,\ +230$ pN for the solid, dashed and dotted lines respectively, which corresponds to the dimensionless values $T'_0 = -39.4,\ 0,\ +100$.

where

$$T'_{\rm dc} = \frac{\ell^2 T_{\rm dc}}{D} = T'_0 + \frac{Ar^2}{2I}\int_0^1 \left(\frac{\partial u'_{\rm dc}}{\partial x'}\right)^2 {\rm d}x',\ \ T'_0 = \frac{\ell^2 T_0}{D},\ \ \text{and}\ \ l'_{\rm dc} = l_{\rm dc}/r. \tag{35}$$

The definition of $T'_{\rm dc}$ with the $\ell^2$ dependence shows that tension becomes more and more important when the length of the device increases. Figure 11a shows the dc displacement profiles for different values of the static tension. In the case where the bending rigidity dominates (top panel) the profile is rounded at the edge, whereas for high tension (lower panel) the profile is much sharper. The tension and center deflection are calculated by self-consistently solving Eq. 31 with Eq. 35, and are plotted in Fig. 11b and c. Two different slopes can be distinguished in the double-logarithmic plot of Fig. 11b. These correspond to the weak and strong bending regime [158], where $u_{\rm dc}$ is proportional to $F_{\rm dc}$ and $F_{\rm dc}^{1/3}$ repectively. The two regimes cross at $T'^{*}_{\rm dc} = 6\sqrt{70} \approx 50.2$, $l'^{*}_{\rm dc} = 36 \cdot 70^{3/4} \approx 871$. The gate voltage at which $l'_{\rm dc} = l'^{*}_{\rm dc}$ is called the cross-over voltage, $V^{*}_{\rm g}$. AFM measurements of the gate-induced displacement of multi-walled carbon nanotubes have confirmed this scaling behavior experimentally [135].

To calculate the gate-tuning of the resonance frequency $f_R(V_{\rm g}^{\rm dc})$, the scaling analysis is also applied to the equation for the ac displacement, Eq. 32. One immediately finds the length scale $l_{\rm ac} = \ell^4 F_{\rm ac}/D$ for the ac force and $T'_{\rm ac} = T_{\rm ac}\ell^2/EI$. As in Sec. 2.4.1, $\omega_{ch} = (D/\rho A)^{1/2}/\ell^2$ is again the characteristic frequency scale for the bending mode vibrations. Next, one has to solve Eqs. 34 and 35 to obtain the static tension and dc displacement. Then, the boundary conditions are imposed to find the resonance frequencies. Figure 12a shows the calculated eigenfrequencies, plotted against the static pulling force for different residual tensions. The higher the residual tension is, the higher the resonance frequencies are at a given $V_{\rm g}^{\rm dc}$. The value $T'_0 = -39.4 \approx T_c$ indicates that the thin resonator is close to buckling; this is visible by the nearly vanishing resonance frequency of the first mode at low $V_{\rm g}^{\rm dc}$. When the static force is increased, all resonance frequencies increase and the differences between the curves due to the different residual tensions become smaller.

To relate the dimensionless quantities in this Subsection to physical ones, the system dimensions are needed. Table 5 shows the estimated sizes and the calculated values of several parameters for two typical nanotube devices, one with a length $\ell = 1\,\mu$m and one with a length $\ell = 200$ nm. Note, that with our definition of $u_n$, the mass and spring constant appearing in the zero-point motion $u_0$ (Eq. 51) and the equipartition theorem (Eq. 54) are equal to the total mass $m$ and $k_R = m\omega_n^2$ respectively. There is no need to introduce an effective mass; see Sec. 3.1. The table indicates that for a long device tension is important and the difference between $f_R$ and $f_0$ is large. For a short resonator, the mechanical properties are mainly determined by the bending rigidity and $f_R \approx f_0$. The higher value of $V^{*}_{\rm g}$ indicates that a larger gate voltage has

Table 5: Data for two suspended carbon nanotubes with different lengths $\ell$. The values of the parameters are calculated with a nanotube radius $r = 1.5\,\text{nm}$, and distance to the gate electrode $h_g = 500\,\text{nm}$. The resonance frequency $f_R$, tension $T_{dc}$ and static displacement $u_{dc}(\ell/2)$ are evaluated for a gate voltage $V_g^{dc} = 4\,\text{V}$ and zero residual tension. $m$, $f_0$ and $D$ are the mass, resonance frequency of the nanotube without tension and the bending rigidity respectively. Furthermore, $k_{dc}$ and $k_R = m\omega_R^2$ are the static and dynamic spring constants [165, 166, 167], $C_g$ is the capacitance to the gate and $u_0$ the zero-point motion (see Sec. 1 for its definition and the discussion in Sec. 3).

| $\ell$ | 1.00 | 0.20 | $\mu$m |
|---|---|---|---|
| $m$ | 6.4 | 1.3 | $10^{-21}$ kg |
| $D$ | 4.8 | 4.8 | $10^{-24}$ Nm$^2$ |
| $f_0$ | 97.0 | 2424 | MHz |
| $f_R$ | 238.6 | 2424 | MHz |
| $k_R$ | 14.5 | 299 | $10^{-3}$ N/m |
| $u_0$ | 2.3 | 1.6 | pm |
| $C_g$ | 8.56 | 1.71 | aF |
| $\partial C_g/\partial u$ | 2.63 | 0.53 | zF/nm |
| $F_{dc}\ell$ | 21 | 4.2 | pN |
| $l_{dc}$ | 4412 | 7.1 | nm |
| $u_{dc}(\ell/2)$ | 4.1 | 0.018 | nm |
| $k_{dc}$ | 11.9 | 229 | $10^{-3}$ N/m |
| $T_{dc}$ | 0.35 | $1.8 \cdot 10^{-4}$ | nN |
| $T'_{dc}$ | 73 | $1.5 \cdot 10^{-3}$ | |
| $V_g^*$ | 2.2 | 54.4 | V |
| $l'_{dc}$ | $2.9 \cdot 10^3$ | 4.7 | |

to be applied to tune this resonator to the strong bending regime.

As a final note, we consider the difference between a nanobeam resonator with a high frequency and one with a low frequency that is tuned using a gate voltage to the same frequency as the former [159]. The current associated with the motion in mixing experiments (see Sec. 4.3.3) [73, 20, 76, 78, 82, 83] is proportional to the length-averaged displacement amplitude $\mu_n u_n(\omega)$; it is thus proportional to the length scale $l_{ac}$ that determines the amplitude. As a consequence, the mechanical signal drops rapidly with decreasing length, making the measurement of single-walled carbon nanotubes with $f_0 > 1\,\text{GHz}$ (corresponding to a device with $\ell \lesssim 0.2\,\mu\text{m}$ and $r = 1\,\text{nm}$) challenging as the signal is about 100× smaller compared to a $f_0 = 100\,\text{MHz}$ device with $\ell \approx 0.6\,\mu\text{m}$. The latter tube can also operate at 1 GHz frequency by tuning it with a gate-induced tension of $T'_{dc} = 5 \cdot 10^3$. In this case the signal decreases too, but only by a factor of 10. A tension of $T'_{dc} = 5 \cdot 10^3$ corresponds to a strain of about 0.2%, which is larger than the values in the abovementioned experiments, but is still smaller than the strain at which single-walled carbon nanotubes break [168, 169, 170].

### *2.4.5. Nanodrums*

So far, we have only considered one-dimensional resonators such as beams and strings. An example of a two dimensional resonator is a graphene nanodrum. This device consists of a hole that is etched in a substrate and that is covered by a (few-layer) graphene flake. Surprisingly, an one-atom layer can be suspended and holes with a diameter of $100\,\mu$m have been reported [171]. A much smaller version of these devices (a nanodrum) has been used to study the (im)permeability of graphene to gases [100] and to measure the bending rigidity of and tension in the flake using an atomic force microscope [107, 172]. In the latter experiments, an atomic force microscope tip is used to apply a force $F_{tip}$ to the flake as illustrated in Fig. 13a. This versatile technique has also been applied to other geometries [173, 174] and nanomaterials [175, 176, 177]. The point $(r_0, \theta_0)$ where the force is applied can be varied and the resulting deflection of the nanodrum is measured. The restoring force that opposes the applied force has several contributions. First of all, there is the bending rigidity of the flake $D$, and secondly, tension may be present in the flake.

Since graphite is highly anisotropic, the analysis of the bending rigidity of an isotropic material in Sec. 2.3 has to be generalized.[14] Using the compliance tensor in Eq. 11 the rigidity for bending along the sheets (see Fig. 5b) is calculated:

$$D = E_\square h^3/12(1-\nu_\square^2), \tag{36}$$

which only contains the in-plane elastic constants. However, when the number of graphene layers becomes small, corrections to Eq. 36 have to be made. Consider the situation in Fig. 5b where a few-layer graphene sheet is bent with a radius

[14] The analysis is in principle also valid for other layers two-dimensional membranes; for a thin isotropic membrane Eq. 38 and the derivation following it are still valid if the appropriate bending rigidity $D$ is taken.

of curvature $R_c$. In the continuum case, the bending energy is given by $U_B/\ell W \equiv \frac{1}{2}D/R_c^2 = \frac{1}{2}\int_{-h/2}^{h/2} E_\square (z/R_c)^2\,\mathrm{d}z$, when taking $\nu = 0$ for simplicity. In the case of a small number of layers $N$, the continuum approximation in the z-direction is no longer valid and the stress is located only at the position of the sheets $z_i = c(i - [N+1]/2)$, where $c = 0.335\,\mathrm{nm}$ is the inter-layer spacing (see p. 12). The integral over $z$ is replaced by a sum and the bending rigidity becomes:

$$D_N = \frac{E_\square h^3}{12(1-\nu_\square^2)}\frac{N-1}{N}, \tag{37}$$

where the thickness is set by the number of layers $h = Nc$, which reduced to Eq. 36 in the limit $N \to \infty$. According to Eq. 37 the bending rigidity vanishes for a single layer. However, molecular dynamics simulations have shown that a single layer of graphene still has a finite bending rigidity: of the order of one eV [117, 178, 179] (compare this to the value for a double layer ($N = 2$) calculated with Eq. 37: $D_2 = 54\,\mathrm{eV}$). The rigidity of a single layer comes from the fact that electrons in the delocalized $\pi$-orbitals, located below and above the sheet, repel each other when the sheet is bent [179].

The deflection of the nanodrum satisfies the equation for the deflection of a plate, Eq. 17, and when the force applied by the AFM tip is assumed to be located at a single point $(x_0, y_0)$, one gets [138, 180, 181, 182]:

$$\left(D\nabla^4 - \frac{\partial}{\partial x_\alpha}T_{\alpha\beta}\frac{\partial}{\partial x_\beta}\right)u(x,y;x_0,y_0) = F_{\mathrm{tip}}\delta(x-x_0)\delta(y-y_0). \tag{38}$$

Here, the $\nabla$-operator and the partial derivatives $\partial/\partial x_i$ are working in the xy-plane only, as the z-dependence is absorbed in the bending rigidity (see Sec. 2.3) and where the tension $T_{\alpha\beta} = \int_0^h \sigma_{\alpha\beta}\,\mathrm{d}z$. This equation is difficult to solve in its most general form, but fortunately some simplifications can be made: The tension tensor can have both normal and shear components. It is, however, always possible to find two orthogonal directions where the shear components are zero [136]. When we assume that the tension is uniform then these directions are independent of position, so without loss of generality the x and y-axis are taken along the principle directions of the tension. When the difference in tension in the x and y direction, $\Delta T = (T_{xx} - T_{yy})/2$, is small, first the solution for isotropic tension ($T_{\alpha\beta} \approx T\delta_{\alpha\beta}$) is obtained and then the correction due to the finite $\Delta T$ can be calculated [165]. Here, we will focus on the situation where $\Delta T = 0$. For a circular membrane, it is convenient to use polar coordinates and the equation for the displacement reads[15]:

$$\left(D\nabla^4 - T\nabla^2\right)u(r,\theta;r_0,\theta_0) = \frac{F_{\mathrm{tip}}}{r}\delta(r-r_0)\delta(\theta-\theta_0). \tag{39}$$

The solution is written as:

$$u(r,\theta;r_0,\theta_0) = \sum_{m=0}^{\infty} R_m(r;r_0)\cos(m\theta - m\theta_0). \tag{40}$$

Inserting this into Eq. 39 yields for the radial coefficients:

$$\begin{aligned} R_0(r;r_0) = {} & A_0 I_0(\lambda r/R) + B_0 K_0(\lambda r/R) + \\ & C_0\ln(r/R) + D_0 + R_0^{(p)}(r;r_0), \end{aligned} \tag{41}$$

$$\begin{aligned} R_m(r;r_0) = {} & A_m I_m(\lambda r/R) + B_m K_m(\lambda r/R) + \\ & C_m(r/R)^{-m} + D_m(r/R)^m + R_m^{(p)}(r;r_0) \quad (m>0), \end{aligned} \tag{42}$$

where $I_m$ and $K_m$ are the Bessel functions of the first and second kind respectively, and $\lambda = \sqrt{TR^2/D}$ is a dimensionless parameter that indicates the importance of the tension in comparison with the bending rigidity of the flake.

The flake with radius $R$ is clamped at the edge of the circular hole so the boundary conditions are $u(R) = 0$ and $\mathrm{d}u/\mathrm{d}r|_{r=R} = 0$. Furthermore, the deflection at the center is finite and smooth (i.e., $\mathrm{d}u/\mathrm{d}r|_{r=0} = 0$). The set of coefficients $\{A_m, B_m, C_m, D_m\}$ can be calculated analytically. Figure 13b shows the deflection profiles calculated where the force is applied at different distances $r_0$ from the center. The deflection of the flake is clearly reduced when the AFM tip is moved away from center of the nanodrum. This indicates that its local compliance $k_f^{-1}(r_0,\theta_0) = \partial u(r_0,\theta_0;r_0,\theta_0)/\partial F_{\mathrm{tip}}$ decreases. As the tension is assumed to be isotropic, $k_f^{-1}$ is independent of $\theta_0$ and its radial profile, shown in Fig. 13c for different values of the tension, contains all the information. In analogy with the displacement profile of a bending and tension-dominated carbon nanotube (Fig. 11a), the profile is rounded at the edge of the hole for vanishing tension ($\lambda = 0$), whereas for large tension ($\lambda \to \infty$) the compliance profile becomes much shaper[16] at the edge and diverges at

[15] $\nabla^2 = \frac{\partial^2}{\partial x^2} + \frac{\partial^2}{\partial y^2} = \frac{\partial^2}{\partial r^2} + \frac{1}{r}\frac{\partial}{\partial r} + \frac{1}{r^2}\frac{\partial^2}{\partial\theta^2}$ and
$\nabla^4 = \frac{\partial^4}{\partial x^4} + \frac{\partial^4}{\partial y^4} = \frac{\partial^4}{\partial r^4} + \frac{2}{r}\frac{\partial^3}{\partial r^3} - \frac{1}{r^2}\frac{\partial^2}{\partial r^2} + \frac{1}{r^3}\frac{\partial}{\partial r} + \frac{4}{r^4}\frac{\partial^2}{\partial\theta^2} + \frac{1}{r^4}\frac{\partial^4}{\partial\theta^4} + \frac{2}{r^2}\frac{\partial^4}{\partial r^2\partial\theta^2} - \frac{2}{r^3}\frac{\partial^3}{\partial r\partial\theta^2}$.

[16] In the limit $\lambda \to \infty$, the $\nabla^4$ term in Eq. 39 vanishes and only a second order differential equation remains. Therefore, the boundary conditions $\mathrm{d}u/\mathrm{d}r|_{r=0,R} = 0$ are discarded.

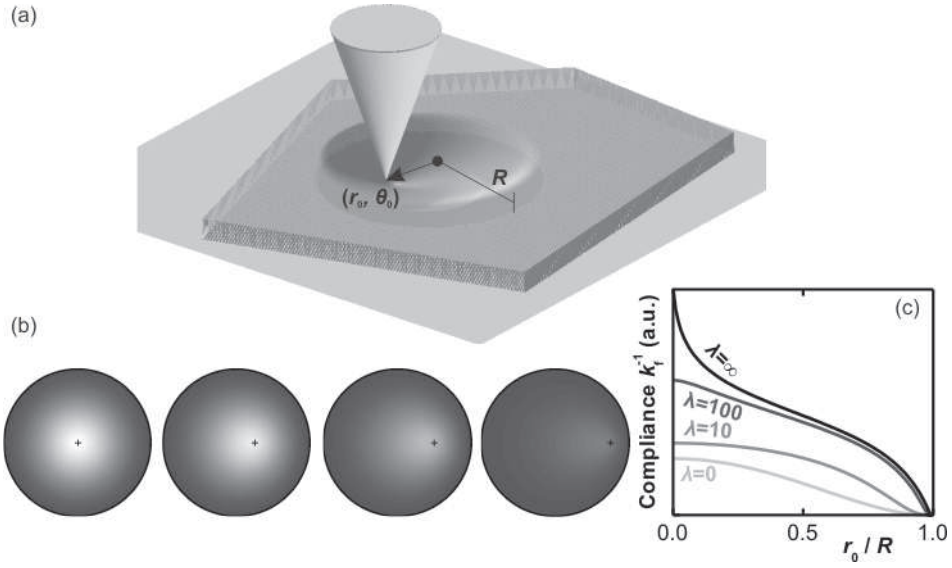


Figure 13: (a) Schematic overview of the nanodrum. A few-layer graphene flake is suspended over a circular hole with radius $R$. A force is applied at the point $(r_0, \theta_0)$ using an AFM tip. This results in a deflection of the nanodrum (b) Colormaps of the calculated deflection profile (Eq. 39) of a nanodrum with vanishing tension. The force is applied at the location of the cross and the color scale is identical in all four panels: white corresponds to a large deflection and dark gray to no deflection. (c) The calculated radial compliance profile for different values of the tension, with $\lambda^2 = TR^2/D$.

the center for a point force. In practice the tip has a finite radius of curvature which prevents that the spring constant of the flake $k_f(r_0 = 0)$ vanishes [172]. By comparing the experimentally measured profile with the calculated ones, the values for $D$ and $T$ can be determined [107]. Knowing the tension (and in principle also the bending rigidity, but this is negligible for thin flakes) an estimate of the resonance frequency can be made. The fundamental eigenfrequency of a circular drumhead is $f_0 = \sqrt{T/\rho_{2d}}/2\pi R \cdot \nu_0^2$, where $\nu_0 \approx 2.4048$ is the first zero of the zero-order Bessel function of the first kind. Measurements have indicated a typical value of $T \sim 0.3\,\mathrm{N/m}$ for exfoliated single layer graphene flakes [172]. With this value and the value for the two-dimensional mass density of single-layer graphene, $\rho_{2d} = 6.8 \cdot 10^{-7}\,\mathrm{kg/m^2}$ (see page 12) we obtain a resonance frequency of 100 MHz for a nanodrum with a diameter of $2R = 5\,\mu\mathrm{m}$. By decreasing the size of the hole, the frequency can be increased. For a hole with a diameter of 500 nm, the frequency already exceeds 1 GHz. The latter resonator has a mass of only $m = 5 \cdot 10^{-19}\,\mathrm{kg}$ and a very large zero-point motion of $u_0 = 0.4\,\mathrm{pm}$. This makes graphene nanodrums ideal devices for QEMS.

## 3. Backaction and cooling

In this Section we consider the influence of the detector, the so-called backaction and we discuss ways to cool the resonator to the ground state. To describe these effects in detail concepts such as thermal noise, Brownian motion, and the effective resonator temperature are introduced. Next we will discuss detector backaction and show that it plays an important role, especially when continuously probing the resonator properties. Backaction is therefore often an unwanted, but unavoidable element in measurements on mechanical systems. It determines how precise the position can be monitored; ultimately, quantum mechanics poses a limit on continuous linear detection, the standard quantum limit. We will derive this limit in different ways. The standard quantum limit can be circumvented by employing different detection schemes, such as square-law detection and backaction evading measurements. These will however not be discussed in depth in this Review.

Backaction does not just impose limits, it can also work to one's advantage: It can squeeze the resonator motion [183, 184, 185, 186, 187], couple and synchronize multiple resonators [188, 189], and backaction can cool the resonator as we will show. Besides this self-cooling by backaction, other active cooling schemes have been developed. In this Section we will discuss two different cooling schemes, namely active feedback cooling and sideband cooling. It is interesting to note that, at present, cooling has only been performed on top-down devices because the experiments to observe thermal motion of bottom-up devices are more challenging.

### *3.1. From modes to harmonic oscillators*

Before starting the discussion of backaction, first an important point has to be addressed. In the previous Section we have given the equations of motion for several nanomechanical systems. Solving these equations gives the frequency and the displacement profile of a particular mode. An important conclusion of describing small displacements around the equilibrium position of NEMS is that each mode can be viewed as a harmonic oscillator. To show this, we start with expanding the displacement in the basis[17] formed by the eigenfunctions $\xi_n$ [191, 192, 159, 164]:

$$u(x,t) = \sum_n u^{(n)}(t)\xi_n(x). \tag{43}$$

Inserting this into the equation of motion and taking the inner product with $\xi_n$ yields the displacement of mode $n$. For example, for the nanobeams discussed in Sec. 2.4.4, Eq. 32 yields:

$$\left(\omega_n'^2 - \omega'^2 + i\omega'\gamma'\right) u_{\rm ac}^{(n)} = l_{\rm ac}\mu_n; \qquad \mu_n = \int_0^1 \xi_n(x')\,{\rm d}x'. \tag{44}$$

The left hand side shows that the frequency response of each mode is equal to the response function of a damped driven harmonic oscillator. The same conclusion is reached for the other examples: all their modes can be describes as harmonic oscillators. The mathematical reason behind this is that the equation of motion for small deformations of a mechanical system can be written in the form $m_{\rm eff}\ddot{u}(\mathbf{r},t) = -\gamma\dot{u}(\mathbf{r},t) + \mathcal{L}[u(\mathbf{r},t)]$ for some Hermitian operator $\mathcal{L}$. Its eigenfunctions are the mechanical modes and these form a complete orthogonal basis. After expanding the displacement in this basis, a set of uncoupled harmonic oscillators results. An important question that one should ask after the transformation from the spatial modes to the harmonic oscillators is: What is the effective mass $m_{\rm eff}$ of the oscillator? This question might seem trivial at first, but the concept of the effective mass has given rise to much confusion in the past years. From the equation of motion it follows that the effective mass of mode $n$ equals $m_{{\rm eff},n} = \int_V \rho\xi_n^2\,{\rm d}V$. The effective mass thus depends on the normalization of the basis functions, or equivalently on the definition of the mode displacement $u_n$. In this Review we have adopted the convention that the basis functions $\xi_n$ are orthonormal, i.e. $\ell^{-1}\int_0^\ell \xi_n^2\,{\rm d}x = 1$. In this case[18] the effective mass equals the total mass of the system (i.e., $m_{{\rm eff},n} = m$). On the other hand, one can also use different normalizations, for example using the average displacement ($\ell^{-1}\int_0^\ell \xi_n\,{\rm d}x = 1$) or using the maximum displacement ($\max\xi_n = 1$). In these cases, the effective mass differs from the total mass and it depends on the exact mode profile. To illustrate the confusion this may create, consider the flexural modes of a beam resonator: With the latter two definitions, every mode has a different effective mass. Moreover, tuning a flexural resonator from the bending to stretching-dominated regime (Sec. 2.4.4) changes the effective mass of its modes. These complications are avoided by using orthonormal basis functions, where $\ell^{-1}\int_0^\ell \xi_n^2\,{\rm d}x = 1$.

Although some groups study the interaction between different coupled modes in nano and micromechanical systems [193, 194, 195, 164, 124, 196], most experimental and theoretical work focuses on a single mode only and the harmonic oscillator describes the dynamics of the entire mechanical system. In this case, we make no distinction between the

[17] It can be shown that these functions form a basis for functions that satisfy the homogeneous boundary conditions [190, 159].

[18] For simplicity it is assumed that the mass density is constant.

resonator (i.e., the entire mechanical system) and the mode that is studied. However, we note again that the actual displacement of the resonator at a certain position $x$ is given by $u^{(n)}\xi_n(x)$ and not by $u^{(n)}$ itself.

Before reviewing the properties of the classical and quantum harmonic oscillator, we stress, however, that knowledge about the displacement profile remains important when analyzing NEMS experiments. In particular, different detectors or driving forces may couple differently to the displacement profile and could detect therefore different modes. In most cases both the driving and detection mechanisms couple to the average displacement of the resonator. In this case, anti-symmetric modes are not visible in nanomechanical experiments as these have a vanishing value of the length-averaged displacement $\mu_n$ (see Eq. 44 and Table 4). An example is a nanotube resonator with frequency mixing readout (Secs. 2.4.4 and 4.3.3) that is either coupled to a back gate or to a local gate; the former couples uniformly to the whole nanotube, so that the detected signal is proportional to $\mu_n$ and consequently only symmetric modes can be detected. A local gate may, depending on its position, couple to all modes.

### *3.2. The harmonic oscillator*

The harmonic oscillator is probably the most extensively studied system in physics. Nearly everything that returns to its equilibrium position after being displaced can be described by a harmonic oscillator. Examples range from the suspension of a car, traffic-induced vibrations of a bridge, and the voltage in an electrical LC network, to light in an optical cavity. For large amplitudes, the oscillator can become nonlinear. We will not study that situation in this Report, but instead we refer the reader to the large body of literature on this subject, see e.g. Refs. [197, 198]. We will now proceed with describing the classical and quantum harmonic oscillator in more detail and reviewing their basic properties.

#### *3.2.1. The classical harmonic oscillator*

In a harmonic oscillator, the potential energy depends quadratically on the displacement $u$ from the equilibrium position:

$$V(u) = \frac{1}{2}k_R u^2, \tag{45}$$

where $k_R$ is the spring constant. The parabolic shape of the potential results in a force that is proportional to the displacement. When damping and a driving force $F(t)$ are included, the equation of motion reads:

$$m\ddot{u} = -k_R u - m\gamma_R \dot{u} + F(t), \tag{46}$$

for a resonator with mass $m$ and damping rate $\gamma_R$. When the oscillator is displaced and released, it will oscillate at frequency $\omega_R$ with a slowly decreasing amplitude due to the damping. The quality factor $Q = \omega_R/\gamma_R$ indicates how many times the resonator moves back and forth before its energy has decreased by a factor e.

The harmonic oscillator responds linearly to an applied force; in other words, it is a linear system. Any linear system is characterized by its impulse response or Green's function [199]. For the harmonic oscillator, the impulse response $h_{HO}(t)$, is the solution to Eq. 46 with $F(t) = k_R\delta(\omega_R t)$:

$$h_{HO}(t) = \sin(\omega_R t)e^{-\frac{\omega_R t}{2Q}}\Theta(\omega_R t), \tag{47}$$

where $\Theta(t)$ is the Heaviside stepfunction. The impulse response function[19] describes how the resonator reacts to a kick at time $t = 0$ and is plotted in Fig. 14a. The initial displacement is zero, but the kick gives it the resonator a finite velocity at $t = 0$. The resonator then oscillates back and forth with a period $2\pi/\omega_R$ and these oscillations slowly die out due to the dissipation. With the impulse-response function the time evolution of the displacement for a force with arbitrary time-dependence $F(t)$ can be obtained directly:

$$u(t) = h_{HO}(t) \otimes F(t)/k_R, \tag{48}$$

where the symbol $\otimes$ denotes convolution.

In many experiments the oscillator is driven with a periodic force $F(t) = F_0\cos(\omega t)$. After a short ($\sim \gamma_R^{-1}$) transient, the resonator oscillates with the same frequency as the driving force. This motion is not necessary in-phase with the driving signal. Both the amplitude and phase of the motion are quantified by the transfer function $H_{HO}(\omega)$ that is obtained by taking the Fourier transformation[20] of the equation of motion, Eq. 46:

$$H_{HO}(\omega) = k_R\frac{u(\omega)}{F(\omega)} = \frac{\omega_R^2}{\omega_R^2 - \omega^2 + i\omega\omega_R/Q}. \tag{49}$$

[19] This is the Green's function for a high-Q resonator. For lower Q-values, the resonator oscillates at a slightly lower frequency $\omega_R' = \omega_R\sqrt{1-(1/2Q)^2}$ and the impulse response of an underdamped oscillator (i.e., one that has $Q > 1/2$) is: $h_{HO}(t) = \sin(\omega_R' t)\exp(-\omega_R t/2Q)\cdot[1-(2Q)^{-2}]^{-1/2}\Theta(t)$. An overdamped resonator ($Q < 1/2$) returns to $u = 0$ without any oscillations and has a different impulse response. Throughout this Review it is assumed that $Q \gg 1$ so that $\omega_R' \approx \omega_R$ and $h_{HO}$ is given by Eq. 47. Note, that Eq. 49 is valid for all (positive) values of $Q$.

[20] By convention [199], the Fourier transformation is defined as: $X(\omega) = \mathcal{F}[x(t)] = \int_{-\infty}^{+\infty} x(t)\exp(-i\omega t)\,\mathrm{d}t$ so that the inverse transformation is given by: $x(t) = \mathcal{F}^{-1}[X(\omega)] = \frac{1}{2\pi}\int_{-\infty}^{+\infty} X(\omega)\exp(+i\omega t)\,\mathrm{d}\omega$.

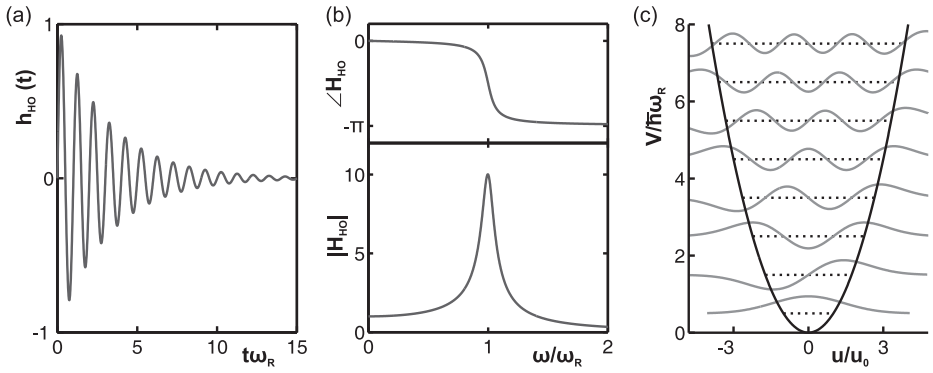


Figure 14: (a) The Green's function $h_{HO}(t)$ and (b) frequency response $H_{HO}(\omega)$ of a harmonic oscillator with $Q = 10$. (c) Eigenenergies $E_n$ (dashed) and the corresponding wave functions $\psi_n(u)$ (solid) of the harmonic oscillator for $n = 0..7$.

The magnitude $|H_{HO}(\omega)|$ and phase $\angle H_{HO}(\omega)$ are plotted in Fig. 14b. When the driving frequency is far below the resonance frequency, the oscillator adiabatically follows the applied force: $u(t) = F(t)/k_R \Leftrightarrow H_{HO} = 1$, and so both $|H_{HO}|$ and $\angle H_{HO}$ are small. The small motion is then almost in phase with the driving signal. The amplitude grows when sweeping the frequency towards the natural frequency. Exactly on resonance, the amplitude has its maximum $|H_{HO}| = Q$. The phase response shows that at the resonance frequency, the displacement lags the driving force by $-\pi/2$. When further increasing the driving frequency, the oscillator can no longer follow the driving force: the amplitude drops and the lag approaches $-\pi$. The motion is then 180° out of phase with the applied force. The width of the resonance peak is related to the damping: the full width at half maximum of the resonance equals $\gamma_R = \omega_R/Q$.

*3.2.2. The harmonic oscillator in quantum mechanics*

In quantum mechanics the harmonic oscillator is described by the Hamiltonian $\hat{H} = \hat{p}^2/2m + \frac{1}{2}m\omega_R^2\hat{u}^2$ [2], as the classical displacement coordinate $u$ and momentum $p = m\dot{u}$ have to be replaced by the *operators* $\hat{u}$ and $\hat{p} = -i\hbar \cdot \partial/\partial u$. The displacement is described by a wave function $\psi(u)$ that satisfies the time-independent Schrödinger equation:

$$\hat{H}\psi = -\frac{\hbar^2}{2m}\frac{\partial^2\psi}{\partial u^2} + \frac{1}{2}m\omega_R^2\hat{u}^2\psi = E\psi. \tag{50}$$

This equation is solved by introducing the creation and annihilation operators: $\hat{a}^\dagger = (m\omega_R\hat{u} - i\hat{p}) / \sqrt{2m\hbar\omega_R}$ and $\hat{a} = (m\omega_R\hat{u} + i\hat{p}) / \sqrt{2m\hbar\omega_R}$ respectively. The Hamiltonian then becomes $\hat{H} = \hbar\omega_R(\hat{n} + \frac{1}{2})$, where $\hat{n} = \hat{a}^\dagger\hat{a}$ is the number operator that counts the number of phonons in the oscillator. The eigenenergies are $E_n = \hbar\omega_R(n + \frac{1}{2})$, with eigenstates $|n\rangle$. The corresponding wave functions $\psi_n(u)$ are plotted in Fig. 14c. The lowest ($n = 0$) eigenstate has a non-zero energy $E_0 = \frac{1}{2}\hbar\omega_R$, the so-called zero-point energy. Even when the oscillator relaxes completely, it still moves around the potential minimum at $u = 0$. The probability density of finding the resonator at position $u$, is given by $|\psi_0(u)|^2$ when the resonator is in the ground state. The zero-point motion $u_0$ is the standard deviation of this probability density:

$$u_0 \equiv \left(\int_{-\infty}^{\infty} u^2|\psi_0(u)|^2\,\mathrm{d}u\right)^{1/2} = \langle 0|\,\hat{u}^2\,|0\rangle^{1/2} = \sqrt{\frac{\hbar}{2m\omega_R}}. \tag{51}$$

The zero-point motion is an important length scale that determines the quantum limit on continuous linear position measurement and is also related to the effective resonator temperature as the following Sections will show.

*3.3. Thermal and quantum noise*

In the previous Section, Sec. 3.2.2 it was shown that a resonator always moves because it contains at least the zero-point energy. In practise, except at the lowest temperatures, the zero-point motion is overwhelmed by thermal noise. Thermal noise is generated by the environment of the resonator. As an example, consider a resonator in air. At room temperature, the air molecules have an average velocity of about 500 m/s. The molecules randomly hit the resonator and every collision gives the resonator a kick. These kicks occur independently of each other, so the resonator experiences a stochastic force $F_n(t)$. Other thermal noise sources are phonons in the substrate that couple to the resonator via the clamping points, fluctuating amounts of charge on nearby impurities and so on. The environment of the resonator is thus a source of random fluctuations on the oscillator. The force noise can be described by an autocorrelation function

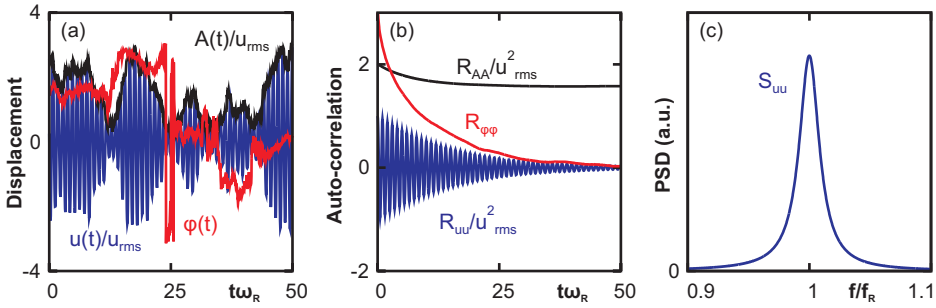


Figure 15: (a) Simulated time-trace of the displacement (blue), amplitude (black) and phase (red) of a resonator that is driven by Gaussian white noise for $Q = 50$. The phase $\varphi$ is in radians and both the displacement $u$ and amplitude $A$ are normalized by the root-mean-square displacement $\langle u^2 \rangle^{1/2}$. The corresponding auto-correlation functions and the displacement-noise power spectral density are shown in (b) and (c) respectively. The area under the curve in (c) equals the variance of the displacement.

$R_{F_nF_n}(t) = \mathbb{E}[F_n(t')F_n(t'+t)]$ (the symbol $\mathbb{E}$ denotes the expectation value) or by its power spectral density[21] (PSD) $\overline{S}_{F_nF_n}(\omega)$ [200]. For white noise, the latter is independent of frequency and $F_n(t)$ has an infinite variance. For a given $F_n(t)$ the realized displacement is easily found using the Green's function, i.e., with Eq. 48. Figure 15a shows a simulated time-trace of this so-called Brownian motion. The resonator oscillates back and forth with frequency $\omega_R$ while its phase and amplitude vary on a much longer timescale. The displacement can be written as $u(t) = A(t)\cos[\omega_R t + \varphi(t)]$ (see Appendix A) and the time-traces of the amplitude $A$ and phase $\varphi$ are plotted in Fig. 15a as well. Figure 15b shows the calculated autocorrelation functions of the displacement, amplitude and phase. The displacement autocorrelation $R_{uu}(t)$ displays oscillations with period $2\pi/\omega_R$, whereas $R_{AA}$ and $R_{\varphi\varphi}$ do not contain these rapid oscillations. All three functions fall off at timescales $\sim Q/\omega_R$. Note, that $R_{AA}(t)$ does not go to zero for long times, because $\mathbb{E}[A] > 0$ as $A(t)$ is always positive.

The displacement PSD is proportional to the force noise PSD and is given by [200]:

$$\overline{S}_{uu}(\omega) = k_R^{-2}|H_{HO}(\omega)|^2\overline{S}_{F_nF_n}. \tag{52}$$

When $\overline{S}_{F_nF_n}$ is white in the bandwidth of the resonator, which is typically assumed, $S_{uu}$ has the characteristic bell shape shown[22] in Fig. 15c. Moreover, the PSD can be used to obtain the variance of the displacement:

$$\langle u^2 \rangle = \frac{1}{2\pi}\int_0^\infty \overline{S}_{uu}(\omega)\,\mathrm{d}\omega = \frac{1}{4}\frac{Q\omega_R}{k_R^2}\overline{S}_{F_nF_n} = \frac{\pi}{2}\frac{Qf_R}{k_R^2}\overline{S}_{F_nF_n}. \tag{53}$$

The force noise PSD is related to the temperature, and in equilibrium the resonator temperature equals the environmental temperature. The equipartition theorem [201] relates the variance of the displacement to the equilibrium temperature:

$$\frac{1}{2}k_R\langle u^2 \rangle = \frac{1}{2}m\langle \dot{u}^2 \rangle = \frac{1}{2}k_\mathrm{B}T. \tag{54}$$

The thermal energy $k_\mathrm{B}T$ is distributed equally between the potential energy and the kinetic energy. By combining Eqs. 53 and 54, a relation between the force noise PSD and the properties of the resonator is found:

$$\overline{S}_{F_nF_n}(\omega) = 4k_\mathrm{B}Tm\omega_R/Q. \tag{55}$$

This so-called fluctuation-dissipation theorem [201, 202, 203] shows that on one hand the force noise PSD can directly be obtained from the resonator properties and temperature, without knowing its microscopic origin. On the other hand, the force noise determines the dissipation (i.e., quality factor) of the resonator.

At equilibrium, the temperature of the resonator is proportional to the variance of its Brownian motion as indicated by Eq. 54. However, out of equilibrium the force noise is no longer given by Eq. 55, and the resonator temperature can be

[21] The engineering convention for the single-sided power spectral density, $\overline{S}_{XX}(\omega) = S_{XX}(\omega) + S_{XX}(-\omega)$, is used. Here, $S_{XX}(\omega) = \mathcal{F}[R_{XX}]$ is the double-sided PSD and $R_{XX}$ is its autocorrelation function. The variance of $X$ is given by $\langle X^2 \rangle = R_{XX}(0) = (2\pi)^{-1} \cdot \int_{-\infty}^{\infty} S_{XX}(\omega)\,\mathrm{d}\omega = (2\pi)^{-1} \cdot \int_0^\infty \overline{S}_{XX}(\omega)\,\mathrm{d}\omega$.

[22] This peak shape is often said to be Lorentzian, although formally that is not correct. The peak is proportional to $[(\omega_R^2 - \omega^2)^2 + \omega_R^4/Q^2]^{-1}$, which can be approximated by $\omega_R^{-2}/[(\omega_R - \omega)^2 + \omega_R^2/Q^2]$ for $\omega \approx \omega_R$. The latter is indeed a Lorentzian, but the approximation is only valid for frequencies close to the resonance frequency of a high-Q resonator.

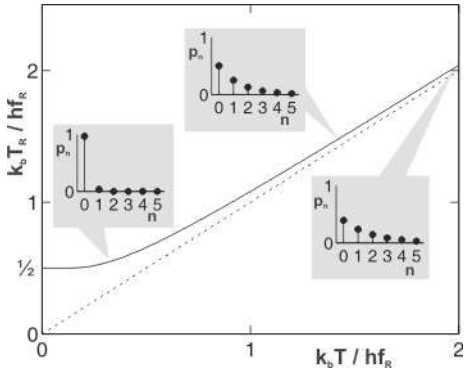


Figure 16: The resonator temperature $T_R$ plotted against the environmental temperature $T$. At low temperatures $T$ the resonator temperature saturates at the zero-point energy: $T_R = \frac{1}{2}\hbar\omega_R/k_B$ and at high temperatures $T_R = T$ (dashed line). The insets show the occupation probability $P_n$ of the energy levels at $k_B T/\hbar\omega_R = 0.3,\ 1/\ln 2 \approx 1.44$ and 2.0.

different from $T$. The effective resonator temperature $T_R$ is defined as:

$$T_R \equiv \frac{k_R\langle u^2\rangle}{k_B} = \frac{k_R}{k_B}\int_0^\infty \overline{S}_{uu}(\omega)\frac{d\omega}{2\pi} = \frac{k_R}{k_B}\int_0^\infty |H_R|^2\overline{S}_{FF}(\omega)\frac{d\omega}{2\pi}, \tag{56}$$

which yields $T_R = T$ in equilibrium. When the force noise is larger than that of Eq. 55, the effective resonator temperature is higher than the environmental temperature. When $\langle u^2\rangle$ is smaller than its equilibrium value, $T_R < T$. Equation 56 shows that the resonator temperature can be obtained from the experimental displacement noise PSD: The resonator temperature is proportional to the area under the curve (Fig. 15c). Note that the suggestive notation $d\omega/2\pi = df$ is used in Eq. 56 as in an measurement typically the real frequency $f$ is on the horizontal axis and not the angular frequency $\omega$.

When the resonator is cooled to very low temperatures where $k_B T \sim \hbar\omega_R$, the classical description breaks down as the quantized energy-level structure (Fig. 14c) becomes important. Semi-classically, the thermal and quantum effects are combined by replacing the force noise of Eq. 55 with the Callen and Welton equation [204]:

$$\overline{S}_{F_nF_n}(\omega) = \frac{4m\omega}{Q}\cdot\frac{1}{2}\hbar\omega\coth\left(\frac{\hbar\omega}{2k_B T}\right), \tag{57}$$

so that for $Q \gg 1$:

$$\langle u^2\rangle = u_0^2\cdot\coth\left(\frac{\hbar\omega_R}{2k_B T}\right) \quad\Leftrightarrow\quad T = \frac{\hbar\omega_R}{k_B}\ln^{-1}\left(\frac{\langle u^2\rangle + u_0^2}{\langle u^2\rangle - u_0^2}\right). \tag{58}$$

Then by inserting the first part of Eq. 58 in Eq. 56 the resonator temperature is obtained[23]. The dependence of $T_R$ on the environmental temperature is shown in Fig. 16. At high temperatures ($k_B T \gg \hbar\omega_R$) the resonator temperature is the temperature of the environment: $T_R = T$. At zero temperature the resonator temperature is determined by the quantum fluctuations: $T_R = \frac{1}{2}\hbar\omega_R/k_B$.

In thermal equilibrium, the energy levels of a harmonic oscillator have occupation probabilities that are given by [201]:

$$P_n = \left(e^{-\frac{\hbar\omega_R}{k_B T}}\right)^n\left(1 - e^{-\frac{\hbar\omega_R}{k_B T}}\right). \tag{59}$$

The average thermal occupation is $\overline{n} = \sum_{n=0}^\infty nP_n = [\exp(\hbar\omega_R/k_B T) - 1]^{-1}$ [201], which equals $k_B T_R/\hbar\omega_R - \frac{1}{2}$. The insets in Fig. 16 show the occupation probabilities at three different temperatures $T$. At low temperature the resonator is in the ground state most of the time. At $k_B T = \ln 2\ \hbar\omega_R$ the probability finding the resonator in the ground state is exactly 50% and the average occupation is $\overline{n} = 1$. At any non-zero temperature, there is always a finite probability to find the resonator in an excited state. With the statement that "the resonator is cooled to its ground state" one actually means $\overline{n} \lesssim 1$ . In Sec. 3.5 we will explain in detail how this goal can be achieved using different cooling techniques, but now we will focus on the detection of the resonator position, in particular on the role of the detector, backaction and the standard quantum limit.

[23]Note, that some authors use Eq. 58 instead of Eq. 56 as the definition of $T_R$, which implies that when $\langle u^2\rangle = u_0^2$, $T_R = 0$. This in contrast to the definition used here where $T_R = \frac{1}{2}\hbar\omega_R/k_B$ for $\langle u^2\rangle = u_0^2$. In the latter case $T_R$ is not the actual temperature, but it is a measure for the (quantum or thermal) fluctuations.

### 3.4. Backaction and quantum limits on position detection

Since the discovery of the Heisenberg uncertainty principle in 1927 it is known that quantum mechanics imposes limitations on the uncertainty with which quantities can be measured. This was first discovered for single measurements of conjugate variables, such as the position $u$ and momentum $p$ of a particle, or the components $\sigma_x, \sigma_y$ and $\sigma_z$ of the spin of a spin-1/2 particle.

When a system is initially in a superposition of the eigenstates of the operator corresponding to the quantity that is measured, a strong measurement gives one of the eigenvalues as the outcome [2]. The probability for measuring a value $\mu_i$ is $|c_i|^2$ when $|\psi\rangle = \sum_i c_i |\mu_i\rangle$ was the expansion of the original state in the basis of eigenstates of the operator $\hat{\mu}$, with $\hat{\mu}|\mu_i\rangle = \mu_i |\mu_i\rangle$. At the same time, the wave function collapses into the state corresponding to the measured value $\mu_i$: $|\psi\rangle \rightarrow |\mu_i\rangle$. To obtain the probability of a certain outcome of a measurement of a different quantity $\nu$, the state $|\mu_i\rangle$ has to be expanded in the basis $|\nu_i\rangle$. The uncertainties in $\mu$ and $\nu$ satisfy: $\Delta\mu \cdot \Delta\nu \geq \left|[\hat{\mu}, \hat{\nu}]/2i\right|$, where $[\hat{\mu}, \hat{\nu}] = \hat{\mu}\hat{\nu} - \hat{\nu}\hat{\mu}$ is the commutator of $\hat{\mu}$ and $\hat{\nu}$. For $\hat{\mu} = \hat{u}$ and $\hat{\nu} = \hat{p}$, this yield the Heisenberg uncertainty principle for position and momentum: $\Delta u \cdot \Delta p \geq \hbar/2$. Note that quantum mechanics does not forbid to determine the position with arbitrary accuracy in a single measurement.

Most measurements are, however, not single, strong measurements, but weak continuous measurements instead [205]. As a measurement of the position disturbs the momentum of the resonator, a subsequent measurement of the position after a time $\Delta t$ inevitably is influenced by the previous measurement. This backaction is therefore important in continuous linear displacement detectors. In an experiment, backaction results in three different effects on the resonator: a frequency shift, a change in damping, and a change in the resonator temperature. If the resonator temperature is lower than the bath temperature, backaction has led to self-cooling, whereas a higher temperature indicates that there is a net energy flow from the detector to the resonator.

A way to circumvent backaction is to perform measurements on the position *squared*. As we show in Appendix C, such a square-law detector probes the energy states of the resonator and these are not disturbed by the measurement itself as the energy operator equals, and hence commutes with, the Hamiltonian of the system. Therefore, this measurement scheme is called a quantum non-demolition (QND) or a backaction evading (BE or BAE) measurement [4].

In the following section, continuous (linear) detectors and their backaction are discussed in detail and the quantum limits on position detection are explored. The analysis presented is largely based on the work by Clerk and co-workers [206, 207]. We start with an analysis of generic linear detectors and what the effects of backaction are. Then we discuss three different routes to arrive at the quantum limit: the Haus-Caves derivation, the power-spectral density method, and the optimal estimator approach. These all have different ranges of applicability and rigor but lead to the same conclusion: the quantum limited resolution for continuously monitoring the resonator position is approximately the zero-point motion $u_0$.

The sensitivity and resolution of a detector will be important concepts in the following discussion. These notions, however, sometimes lead to confusion and, before defining them mathematically, we will first discuss the similarities differences between them. Both are a measure of the imprecision with which the position is measured. A noisy detector has a bad sensitivity and a bad position resolution, whereas a good detector has a good sensitivity and resolution. Counterintuitively, this means that the latter detector has *lower sensitivity values*, although one often says that it has a *higher sensitivity*. This is the first point that leads to confusion. The second is the difference between sensitivity and resolution. This can be understood as follows: Consider a resonator that is standing still and that is coupled to a detector that inevitably introduces noise in its output signal. When measuring the position for a short period, the inferred position has a large uncertainty due to the detector noise. By measuring longer, the noise averages out and the uncertainty decreases. This uncertainty is the resolution of the detector and is measured in units of length. It thus depends on the duration of the measurement $\Delta t$. For white detector noise, the resolution improves (i.e. its value decreases) as $1/\sqrt{\Delta t}$. The proportionality constant between the resolution and the measuring time is the sensitivity, and it has the units of $\mathrm{m}/\sqrt{\mathrm{Hz}}$. In the discussion of Fig. 18 it will be shown that the sensitivity is easily extracted from the noise spectrum of the detector output.

#### 3.4.1. Continuous linear detectors

A continuous linear position detector gives an output that depends linearly on the current and past position of the resonator. Figure 17 shows the scheme of a generic linear detector. Note again, that the analysis is for a generic continuous linear detector and quantum effects only come into play in Sec. 3.4.2. We will discuss all its elements step by step. The output signal of the detector[24] is related to the displacement by:

$$v(t) = A\lambda_v(t) \otimes u(t) + v_n(t). \tag{60}$$

Here, $\lambda_v$ is the responsivity of the detector, with $\lambda_v(t) = 0$ for $t < 0$ due to causality. $v_n$ is the detector noise and $A$ is a dimensionless coupling strength. The coupling between the resonator and the detector is an important element when

[24] Continuous linear detectors are usually (implicitly) assumed to be time-invariant [208]. Unless stated otherwise, this is also assumed in this Report. Examples where the linear detector is not time-invariant are frequency-converting, stroboscopic and quadrature measurements [208, 4, 3, 27].

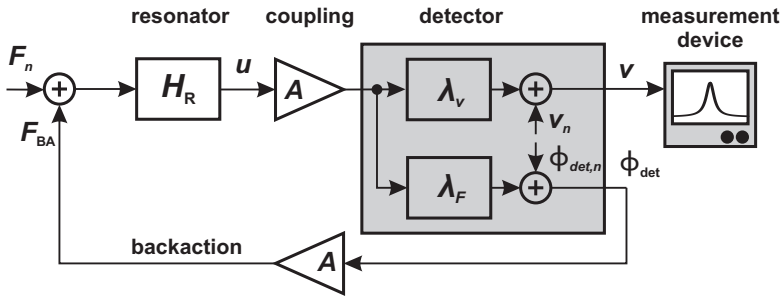


Figure 17: The detector is coupled (via $A$) to the resonator. Its output $v(t)$ depends linearly on $u(t)$ with a response function $\lambda_v$ but also contains detector noise $v_n$. The detector exerts a backaction force $F_{BA} = A\Phi_{det}$ on the resonator that contains a stochastic part $F_{BA,n}$ and a linear response to $u(t)$. Both contributions add up with the thermal or quantum force noise $F_n$. The resonator displacement $u$ is obtained via the transfer function $H_R = H_{HO}/k_0$.

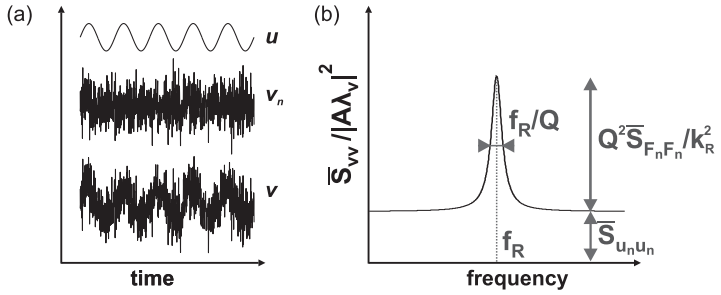


Figure 18: The resonator displacement $u$ is measured by the detector. The detector also adds imprecision noise $v_n$. The sum of this noise and the physical displacement $v$ is recorded. (a) shows schematically time traces of the resonator displacement $u$, imprecision noise $v_n$ and the apparent displacement $v$. Often, one is interested in the noise spectrum of the detector output, especially when the resonator displacement is its Brownian motion. This can be done using a spectrum analyzer and (b) shows that from a resulting spectrum the resonance frequency $f_R$, the quality factor $Q$, the detector noise floor $\overline{S}_{u_nu_n}$ and the force noise $\overline{S}_{F_nF_n}$ are readily extracted. The signal-to-noise ratio is the height of the resonance peak divided by the height of the noise floor. It is therefore advantageous to have a large quality factor as this leads to a larger signal-to noise ratio.

discussing different detectors in Sec. 4. The choice of the coupling $A$ is slightly arbitrary as it could also be incorporated in $\lambda_v$. However, in most detectors it is possible to make a distinction between the coupling to the resonator and the output. Different types of detector will be discussed extensively in Sec. 4, but in the case of an optical interferometer, $v$ represents the number of photons arriving at the photon counter, in a single-electron transistor it is the current through the island, and in a dc superconducting-interference-device detector it represents the output voltage. The difference between $u$, $v$ and $v_n$ is illustrated in Fig. 18a. Note, that often the detector responds instantaneously to the displacement. In that case $A\lambda_v(t) = \partial v/\partial u\ \delta(t)$ and $A\lambda(\omega) = \partial v/\partial u$. The frequency response of the resonator is then flat[25].

To calculate the sensitivity of the detector, the noise at the output of the detector, $v_n$, is referred back to the input using the known response function $\lambda_v$ and gain $A$. This yields the displacement noise $u_n$ at the detector input. The equivalent input noise PSD is $\overline{S}_{u_nu_n} = \overline{S}_{v_nv_n}/|A\lambda_v|^2$. This power spectral density is an important parameter that characterizes the detector. In nanoelectromechanical experiments, this noise floor is usually determined by the classical noise in the electronics of the measurements setup. In optical experiments, however, the noise floor can be shot-noise limited; quantum mechanics now sets the imprecision of the experiment. We will discuss the quantum limit in the next subsection. Note that for a flat frequency response $u_n$ is simply given by $v_n/A\lambda_v$.

The detector does not only add noise to the measured signal, it also exerts a force $F_{BA}(t)$ on the resonator. This is the so-called backaction force. Backaction, in its most general definition, is the influence of a measurement or detector on an object. The detector backaction is a force on the resonator. This can be seen from the following argument: when there is no coupling between the resonator and the detector, i.e., $A = 0$, the Hamiltonian describing the total system is the sum of that of the Hamiltonian of the oscillator and of the detector Hamiltonian. When these are coupled ($A \neq 0$), there is an interaction Hamiltonian of the form $H_{int} = -A\Phi_{det}u$. The backaction force is then $F_{BA} = -\partial H_{int}/\partial u = A\Phi_{det}$ [206]. The backaction force is thus also proportional to the detector-resonator coupling $A$. The quantity $\Phi_{det}$ is related to one of the internal variables of the detector; for example in an optical cavity it is proportional to the number of photons, in a SET to the electron occupation, and in a SQUID to the circulating current.

The backaction force has three different contributions:

- A deterministic force that is independent of the displacement. This changes the equilibrium position of the resonator.

[25] When the output of the detector has a delay time $\tau$, $A\lambda_v(t) = \partial v/\partial u\ \delta(t-\tau)$ and $A\lambda_v(\omega) = \partial v/\partial u\ \exp(-i\omega\tau)$.

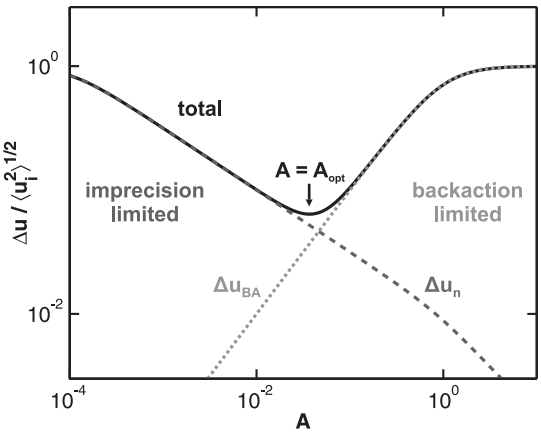


Figure 19: (a) The position resolution of the detector in units of the amplitude of the Brownian motion $\langle u_i^2 \rangle^{1/2}$ (classical limit) for different coupling strengths $A$. The solid line is the total resolution; the dotted line is the contribution of the backaction force noise (Eq. B.5) and the dashed line the contribution of the imprecision noise (Eq. B.6). The total resolution is optimized at $A = A_{\rm opt} \approx 0.0355$. The resolution has been calculated for $Q_0 = 10^4$, $\lambda_v = 1$, $\lambda_F = 0$, $\overline{S}_{v_n v_n} \cdot k_0^2 = \overline{S}_{\Phi_{det,n}\Phi_{det,n}} = \overline{S}_{F_n F_n}$ and $\overline{S}_{\Phi_{det,n} v_n} = 0$.

Without loss of generality it can thus be set to zero and it is not considered here.

- A force that responds linearly to the displacement: $F_{BA,u} = A\lambda_F(t) \otimes Au(t)$. This changes the effective resonator response from $H_R$ to $H'_R$, where $H'^{-1}_R = H^{-1}_R + A^2\lambda_F(\omega)$. An example of this force is the optical spring that we will encounter in Sec. 3.5.3. This part of the backaction can lead to cooling, see Sec. 3.5.1 [32].

- A stochastic force $F_{BA,n} \equiv A\Phi_{det,n}$ that is caused by the fluctuations in the detector, $\Phi_{det,n}$. Note, that this force noise and the imprecision noise $v_n$ can be correlated, i.e., $\overline{S}_{\Phi_{det,n} v_n} \neq 0$. In any case, this contribution tries to heat the resonator since it adds up to the original thermal force noise..

In summary, this whole process of action and backaction is the one shown schematically in Fig. 17: The resonator position is coupled to the input of the detector, which adds imprecision noise $v_n$ and exerts force noise on the resonator. For small coupling $A$, the statistical properties of $\Phi_{det,n}$ and $v_n$ are independent of the resonator displacement [206, 207].

One way to analyze the data is to measure the detector output using a spectrum analyzer. This way, information about the resonance frequency, quality factor, and imprecision and force noise PSD can easily be obtained, as illustrated in Fig. 18b. However, in a linear detection scheme one is usually interested in measuring the resonator position as accurate as possible, without perturbing the resonator considerably. Using optimal-control and estimation theory, the best estimate $\hat{u}$ for the resonator displacement in the absence of the detector, $u_i$, is found. The resolution of the detector is $\Delta u = \left(\mathbb{E}[u_i^2 - \hat{u}^2]\right)^{1/2}$, as explained in detail in Appendix B. It quantifies the difference between the displacement that the resonator would have had when it was not measured and the one reconstructed from the detector output. By rewriting the resolution as $\Delta u = \left(\mathbb{E}[(u^2 - \hat{u}^2) + (u_i^2 - u^2)]\right)^{1/2}$ it becomes clear that there are two contributions [209]: the first one, which we name $\Delta u_n$, indicates how well the realized displacement is reconstructed from the detector output, whereas the second term, $\Delta u_{BA}$, quantifies the difference between $u_i$ and the realized displacement, i.e., how much the motion is perturbed. Heuristically, we can understand that the first term is due to the imprecision of the detector, whereas the second is due to the backaction.

The resolution is plotted in Fig. 19a as a function of the coupling strength $A$. In experiments this coupling strength is an important parameter and Sec. 4 we will give typical numbers for the different detection schemes. We now discuss the general features of Fig. 19 in more detail. With a low coupling $\Delta u$ is large (i.e., the detector has a low resolution) because of the large imprecision noise contribution $\Delta u_n$ (dashed line) of the detector. The backaction contribution is very small. An increase of the coupling reduces $\Delta u$ because by increasing the coupling, the mechanical signal becomes larger whereas $S_{v_n v_n}$ remains the same, so the relative contribution of the imprecision noise decreases. The increase of the coupling also raises the backaction contribution, which still remains small. The resolution improves with increasing $A$ up to the point where the optimal value $A = A_{\rm opt}$ is reached. A further increase of $A$ makes the backaction force noise dominant, driving the resonator significantly, thus yielding a higher $\Delta u$.

### *3.4.2. The Haus-Caves derivation of the quantum limit*

The system analysis of the linear detector discussed above is valid for any – quantum limited or not – linear detector. An elegant way of deriving the quantum limit of a continuous linear position detector was given by Haus and Mullen [210] and was extended by Caves [208]. They consider the situation where the input and output signal of the detector are carried

by single bosonic modes, $\hat{a}_u$ and $\hat{a}_v$ respectively. When the "photon number gain" of the detector is $G = \langle \hat{a}_v^\dagger \hat{a}_v \rangle / \langle \hat{a}_u^\dagger \hat{a}_u \rangle$, one might think that the modes are related to each other by $\hat{a}_v = \sqrt{G}\hat{a}_u$. This is, however, not valid as this gives $[\hat{a}_v, \hat{a}_v^\dagger] = G$ instead of the correct value, 1 [208, 207]. The actual relation is $\hat{a}_v = \sqrt{G}\hat{a}_u + \hat{v}_n$. Here, $\hat{v}_n$ represents the noise added by the amplifier. This operator has a vanishing expectation value ($\langle \hat{v}_n \rangle = 0$) and is uncorrelated with the input signal ($[\hat{a}_u, \hat{v}_n] = [\hat{a}_u^\dagger, \hat{v}_n] = 0$). Requiring $[\hat{a}_v, \hat{a}_v^\dagger] = 1$ yields $[\hat{v}_n, \hat{v}_n^\dagger] = 1 - G$ for the commutator and, more importantly, $\Delta a_v^2 \geq G\Delta a_u^2 + \frac{1}{2}|G - 1|$ for the noise in the number of quanta of the output mode [207]. The first term is the amplified input signal (i.e., the resonator motion) and the second one is the noise added by the amplifier. In the limit of large gain[26] ($G \gg 1$), the equivalent input noise of the detector is $\Delta(a_u^{eqv})^2 \equiv \Delta a_v^2/G - \Delta a_u^2 \geq \frac{1}{2}$. This means that a quantum-limited detector adds at least half a vibrational quantum of noise to the signal.

As pointed out in Ref. [207] most practical detectors cannot easily be coupled to a single bosonic mode that carries the information of the resonator to the detector, because there is also a mode that travels from the detector towards the resonator. Therefore, the linear-system analysis at the beginning of this Section is used to further explore the quantum limits on continuous linear position detection.

### *3.4.3. A quantum-limited detector*

In the previous discussion, no constraints were enforced on the detector noises $\Phi_{det,n}$ and $v_n$. If both noise contributions could be made small enough, the resolution would be arbitrarily good. This is unfortunately not possible. It can be shown that the power spectral densities must satisfy[27]:

$$\overline{S}_{v_n v_n}(\omega) \cdot \overline{S}_{\Phi_{det,n} F_{det,n}}(\omega) - \left|\overline{S}_{\Phi_{det,n} v_n}(\omega)\right|^2 \geq |\hbar \lambda_v(\omega)|^2 , \tag{61}$$

or, equivalently, when this is referred to the input:

$$\overline{S}_{u_n u_n}(\omega) \cdot \overline{S}_{F_{BA,n} F_{BA,n}}(\omega) - \left|\overline{S}_{F_{BA,n} u_n}(\omega)\right|^2 \geq \hbar^2. \tag{62}$$

These constraints enforce the quantum limit of the linear detector and should be considered as the continuous-detector equivalent of the Heisenberg uncertainty principle: Accurately measuring the position results severe force noise and vice versa.

Clerk *et al.* [207] continue now by finding the gain where the total added noise at the input, i.e., $\overline{S}_{u_n u_n}(\omega) + |H_R'|^2 \overline{S}_{F_{BA,n} F_{BA,n}}(\omega)$, is minimized. As they already point out, this is not entirely correct because at every frequency a different optimal gain is required. Usually, only the optimal gain at $\omega = \omega_0$ is used and then the magnitude of the signal and detector noise are equal at that frequency. In that case, the imprecision noise and the backaction-induced displacement provide exactly half of the total added noise [207, 30, 66]. However, by optimizing the total *resolution*, the true optimal gain is found, see Fig. 20. The resolution is optimized at $A = 0.87$ and reaches a value of 0.81 times the zero-point motion.

All three methods (the Haus-Caves derivation, the total added noise at the input, and the optimal estimator) indicate that the detector adds about the same amount of noise as the zero-point fluctuations of the resonator itself.

## *3.5. Cooling*

To prepare a nanomechanical system in the ground state, the thermal occupation of its normal modes should be minimal. The most direct approach is to mount an ultra-high frequency ($f_R > 1\,\mathrm{GHz}$) resonator in a dilution refrigerator ($T < 50\,\mathrm{mK}$) so that $\overline{n} \leq 1$. Such a resonator will, however, have a very small zero-point motion and the readout of tiny high-frequency signals at millikelvin temperatures is difficult. An alternative approach is to perform the experiments with lower-frequency resonators and/or at higher temperatures. The thermal occupation is then higher than one and cooling techniques have to be used to reduce the temperature of the resonator $T_R$ well below the environmental temperature $T$. Figure 21 and Table 6 show how recent experiments are approaching the limit $n \leq 1$ over a range of frequencies that spans seven orders of magnitude.

In most experiments either active feedback or sideband cooling is employed. In the former case, which is discussed in detail in Sec. 3.5.2, the position of the resonator is measured and the detector signal is fed back to the resonator to damp its motion. With sideband cooling (Sec. 3.5.3) the resonator is embedded in an optical or microwave cavity. Phonons can be removed from the resonator by up-converting a red-detuned photon to the resonance of the cavity, thus cooling the resonator. Finally, also other cooling mechanisms like bolometric (photothermal) [31, 41, 211] and backaction cooling [32] (see Sec 3.4) are used. We will now discuss these cooling mechanisms in more detail.

[26] In the opposite limit where the detector does not have any net gain, i.e., $G = 1$, no additional noise is required by quantum mechanics.

[27] Here, it is assumed that the measurement of $v(t)$ does not result in an additional force noise on the resonator and that the detector has a large power gain. For more details, see Ref. [207].

Table 6: Overview of resonator temperature and cooling of recent experiments with micro- and nanomechanical resonators. The table shows the resonance frequency $f_R$, the temperature of the environment $T$, the minimum resonator temperature $T_R^{\min}$ and the corresponding number of quanta. The numbers of the first column correspond to the experiments listed in Table 1.

| | $\mathbf{f_R}$(MHz) | **T**(K) | $\mathbf{T_R^{min}}$(K) | $\bar{\mathbf{n}}$ | **Cooling method** | **Factor** | **Ref.** |
|---|---|---|---|---|---|---|---|
| 1 | $1.0 \cdot 10^3$ | 4.2 | 4.2 | 85 | | | [28] |
| 2 | 117 | 0.030 | 0.030 | 5.3 | | | [29] |
| 3 | 20 | 0.035 | 0.056 | 59 | | | [30] |
| 4 | $7.3 \cdot 10^{-3}$ | 295 | 18 | $5.1 \cdot 10^7$ | Photothermal | 16.3 | [31] |
| 5 | 22 | 0.030 | 0.035 | 33 | Backaction | | [32] |
| 6 | 0.81 | 295 | 10 | $2.6 \cdot 10^5$ | Sideband | 29.3 | [33] |
| 7 | 0.013 | 295 | 0.14 | $2.2 \cdot 10^5$ | Feedback | $2.2 \cdot 10^3$ | [34] |
| 8 | 0.28 | 295 | 10 | $7.5 \cdot 10^5$ | Sideband | 29.3 | [35] |
| 9 | 0.81 | 295 | 5.0 | $1.3 \cdot 10^5$ | Feedback | 58.6 | [36] |
| 10 | 58 | 300 | 11 | $4.0 \cdot 10^3$ | Sideband | 27.1 | [37] |
| 11 | 127 | 295 | 295 | $4.8 \cdot 10^4$ | | | [38] |
| 12 | $1.7 \cdot 10^{-4}$ | 295 | 0.80 | $9.7 \cdot 10^7$ | Sideband | 366.5 | [39] |
| 13 | $1.3 \cdot 10^{-5}$ | 295 | $6.9 \cdot 10^{-3}$ | $1.1 \cdot 10^7$ | Sideband | $4.2 \cdot 10^4$ | [40] |
| 14 | 0.55 | 300 | 175 | $6.7 \cdot 10^6$ | Photothermal | 1.7 | [41] |
| 15 | 43 | 0.25 | 1.0 | 483 | | | [42] |
| 16 | $2.6 \cdot 10^{-3}$ | 2.2 | $2.9 \cdot 10^{-3}$ | $2.3 \cdot 10^4$ | Feedback | 85.7 | [43] |
| 17 | $7.0 \cdot 10^{-3}$ | 295 | 45 | $1.3 \cdot 10^8$ | Sideband | 6.5 | [44] |
| 18 | 0.71 | 295 | 295 | $8.6 \cdot 10^6$ | | | [45] |
| 19 | 0.13 | 294 | $6.8 \cdot 10^{-3}$ | $1.1 \cdot 10^3$ | Sideband | $4.3 \cdot 10^4$ | [46] |
| 20 | 0.56 | 35 | 0.29 | $1.1 \cdot 10^4$ | Sideband | 120.0 | [47] |
| 21 | $8.5 \cdot 10^{-5}$ | 300 | 0.070 | $1.7 \cdot 10^7$ | Feedback | $4.3 \cdot 10^3$ | [48] |
| 22 | 74 | 295 | 21 | $5.9 \cdot 10^3$ | Sideband | 14.0 | [49] |
| 23 | 0.24 | 0.040 | 0.017 | $1.5 \cdot 10^3$ | Sideband | 2.3 | [50] |
| 24 | 428 | 22 | 22 | $1.1 \cdot 10^3$ | | | [51] |
| 25 | $5.0 \cdot 10^{-3}$ | 4.2 | 4.2 | $1.8 \cdot 10^7$ | | | [52] |
| 26 | 2.0 | 0.020 | 0.084 | 874 | | | [19] |
| 27 | $8.7 \cdot 10^{-4}$ | 4.2 | $2.0 \cdot 10^{-3}$ | $4.8 \cdot 10^4$ | Feedback | $2.1 \cdot 10^3$ | [53] |
| 28 | $9.1 \cdot 10^{-4}$ | 4.2 | $1.7 \cdot 10^{-4}$ | $3.9 \cdot 10^3$ | Feedback | $2.5 \cdot 10^4$ | [53] |
| 29 | $1.0 \cdot 10^3$ | 295 | 295 | $5.9 \cdot 10^3$ | | | [54] |
| 30 | 8.9 | 295 | 295 | $6.9 \cdot 10^5$ | | | [55] |
| 31 | 1.5 | 0.050 | 0.050 | 682 | | | [56] |
| 32 | 1.5 | 0.050 | 0.010 | 136 | Sideband | 5.0 | [56] |
| 33 | 8.9 | 295 | 295 | $6.9 \cdot 10^5$ | | | [57] |
| 34 | 6.3 | 300 | 58 | $1.9 \cdot 10^5$ | Feedback | 5.1 | [58] |
| 35 | 13.9 | 295 | 295 | $4.4 \cdot 10^5$ | | | [59] |
| 36 | 0.95 | 5.3 | $1.3 \cdot 10^{-3}$ | 29 | Sideband | $4.1 \cdot 10^3$ | [60] |
| 37 | 65 | 1.65 | 0.20 | 64 | Sideband | 8.2 | [61] |
| 38 | 8.2 | 360 | 7.35 | $1.9 \cdot 10^4$ | Sideband | 49.0 | [62] |
| 39 | 119 | 1.4 | 0.21 | 37 | Sideband | 6.6 | [63] |
| 40 | $1.2 \cdot 10^{-4}$ | 300 | $1.4 \cdot 10^{-6}$ | 237 | Feedback | $2.1 \cdot 10^8$ | [64] |
| 41 | 8.5 | 300 | 12.5 | $3.1 \cdot 10^4$ | Sideband | 23.9 | [65] |
| 42 | 1.04 | 0.015 | 0.130 | $2.6 \cdot 10^3$ | Sideband | | [66] |
| 43 | 8.1 | 300 | 300 | $7.7 \cdot 10^5$ | | | [67] |
| 44 | 6.3 | 0.020 | $1.2 \cdot 10^{-3}$ | 3.8 | Sideband | 17.3 | [68] |
| 45 | 8.3 | 300 | 300 | $7.5 \cdot 10^5$ | | | [69] |
| 46 | $6.2 \cdot 10^3$ | 0.025 | 0.025 | 0.07 | | | [22] |
| 47 | 2.1 | 0.015 | 0.014 | 136 | Feedback | 1.1 | [70] |
| 48 | 10.7 | 0.020 | $3.7 \cdot 10^{-4}$ | 0.34 | Sideband | 113.8 | [23] |

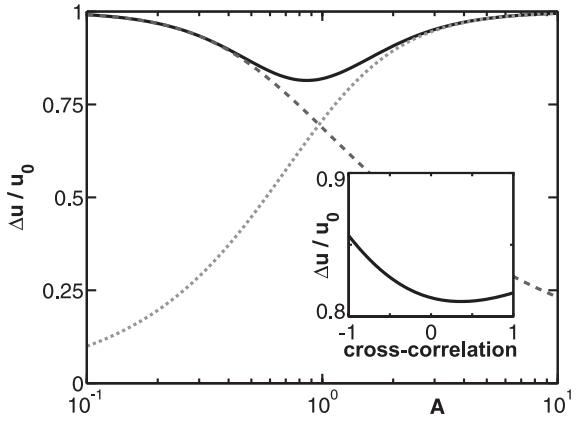


Figure 20: The quantum limit for a continuous linear position detector using the optimal estimation method. The resolution of the detector in units of the zero-point motion is plotted for different coupling strengths $A$. The solid line is the total resolution, $\Delta u$; the dotted and dashed line are the contribution of backaction, $\Delta u_{BA}$, and imprecision noise, $\Delta u_n$, respectively. The inset shows that the total resolution depends on the cross-correlation coefficient $S_{F_{BA,n}u_{BA,n}}/(S_{F_{BA,n}F_{BA,n}} \cdot S_{u_n u_n})^{1/2}$. The main panel is calculated with an optimal cross-correlation of 0.36. For all values of $A$ the total added noise is slightly less than $u_0$.

### *3.5.1. Backaction cooling*

To measure the displacement, the resonator is coupled to a detector. As shown in Sec. 3.4, this influences the resonator, and, in particular, this backaction adds force noise and it can damp the motion, which can lead to cooling. The damping rate of the resonator is then increased from its intrinsic value $\gamma_0 = \omega_0/Q_0$ to $\gamma_R = \gamma_0 + \gamma_{BA}$, where $\gamma_{BA} = -\omega_0^2 A^2 \mathrm{Im}[\lambda_F]/\omega$ is the damping induced by the detector [206]. The resonator temperature is[28] [32, 56, 212]:

$$T_R = \frac{\gamma_0 T + \gamma_{BA} T_{BA}}{\gamma_0 + \gamma_{BA}}. \tag{63}$$

The resonator temperature is thus the weighted average of the environmental temperature $T$ and the so-called backaction temperature of the detector $T_{BA}$. For strong resonator-detector coupling ($\gamma_{BA} \gg \gamma_0$) the effective temperature is $T_R = T_{BA}$. When this is below the environmental temperature, the resonator is cooled by the backaction. Eq. 56 shows that the backaction temperature is determined by the force noise exerted on the resonator: $T_{BA} = S_{F_{BA,n}F_{BA,n}}/4k_\mathrm{B} m\gamma_{BA}$. Both $S_{F_{BA,n}F_{BA,n}}$ and $\gamma_{BA}$ are proportional to $A^2$ so that $T_{BA}$ is independent of the resonator-detector coupling $A$. In other words, the backaction temperature is an intrinsic property of the detector.

Although it might not be immediately clear, this cooling mechanism corresponds to the usual notion of cooling: Cooling is done by coupling something to something else that is colder. In the case of backaction cooling the cold object is the detector. Because the resonator is not *actively* cooled, but only brought into contact with the detector, backaction cooling is therefore also called "self cooling" or "passive feedback cooling".

### *3.5.2. Active feedback cooling*

It was shown in Sec. 3.3 that the resonator temperature is proportional to its random motion. By reducing that motion the resonator gets cooled. One way to do this is using feedback. When the position of the resonator is measured and fed back to it via an external feedback loop, the motion can be amplified or suppressed. Feedback control was already used to regulate the motion of soft cantilevers [213, 214, 215] for magnetic resonance force microscopy [216], when it was realized that this technique can also be used to cool a mechanical resonator towards its ground state [217]. Actually, the lowest resonator temperature to date ($T_R = 1.4\,\mu$K, see Table 6) has been reached using this cooling method [64].

Feedback systems are usually analyzed within the linear system representation. Figure 22 shows a schematic of the process. The resonator, with frequency $\omega_0/2\pi$ and Q-factor $Q_0$, is driven by the thermal force noise $F_n(t)$ and its displacement $u(t)$ is detected. The detector output contains not only the displacement but also imprecision noise $u_n(t)$.[29] The apparent position $v$ is the signal at the output of the detector and this is thus the sum of the physical displacement and the detector noise: $v = u + u_n$. The information contained in $v$ is used to apply a force $F_{FB}$ to the resonator that damps its thermal motion[30]. The relation between the feedback force and the apparent position is described by the linear system or

[28] This assumes that the effective spring constant $k_0 - k_0 A^2 \mathrm{Re}[\lambda_F]$ does not change considerably. As shown in Sec. 3.5.2, it is in general much more difficult to alter the spring constant than to alter the damping.

[29] In this section we assume that the detector has unit gain, i.e., $A\lambda_v(\omega) = 1$. Then the imprecision noise at the output, $v_n$, and the noise referred to the input, $u_n$, are the same.

[30] In principle, also the backaction force noise of the detector has to be included [213, 53, 218]. Although this term was never important in active feedback cooling experiments so far, the effect can be included by using the damping and resonator temperature of the coupled resonator and detector instead of the intrinsic ones of the resonator alone.

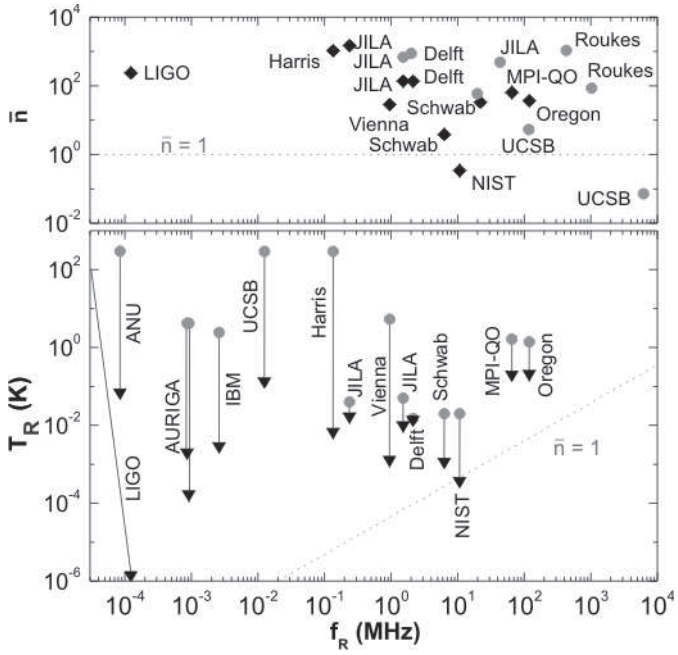


Figure 21: Overview of mechanical resonators with low temperature or occupation, compiled from Table 6. The top panel shows the experiments with the lowest occupation numbers. These are reached using conventional cooling (gray) and active feedback and sideband cooling (black). The dotted line is located at $\overline{n} = 1$. As discussed on page 29, once the thermal occupation is below this value, the resonator is cooled to the ground state. The bottom panel shows the starting temperature $T$ (gray) and the final temperature $T_R^{\min}$ (black) achieved by groups that have actively cooled their resonator below 100 mK. Note the diagonal line in the LIGO experiment which is due to a strong optical spring effect (see Sec. 3.5.3), so both the resonator temperature and frequency change when the laser power is increased [40].

filter with transfer function $H_{FB}(\omega)$. The output of the filter is multiplied by a selectable gain[31] $g$. One can think of it as a knob to crank up the gain of an amplifier. This forms a closed-loop system [199, 213] with the following equations of motion:

$$m\ddot{u}(t) + m\omega_0\dot{u}(t)/Q_0 + m\omega_0^2 u(t) = F_n(t) + F_{FB}(t), \tag{64}$$

$$F_{FB}(t) = m\omega_0^2 g \cdot h_{FB}(t) \otimes [u(t) + u_n(t)]. \tag{65}$$

The presence of the feedback results in a different displacement for a given thermal noise realization $F_n(t)$. The feedback thus changes the resonator response from $H_R$ to the closed-loop transfer function $H'_R$, given by:

$$H_R'^{-1} = H_R^{-1} - gk_0 H_{FB}, \quad \text{or} \quad H'_R = \frac{k_0^{-1}}{1 - \left(\frac{\omega}{\omega_0}\right)^2 + \frac{i}{Q_0}\frac{\omega}{\omega_0} - gH_{FB}}. \tag{66}$$

Comparing this with the response of the resonator itself, cf. Eq. 49, shows that the real part of $H_{FB}$ modifies the resonance frequency from $\omega_0$ to $\omega_R = \omega_0\sqrt{1 - g\mathrm{Re}[H_{FB}(\omega)]}$, whereas the imaginary part alters the damping rate from $\gamma_0$ to $\gamma_R = \gamma_0 - g\omega_0^2\mathrm{Im}[H_{FB}/\omega]$. Using this closed-loop transfer function, the PSDs of the physical (i.e., the real resonator displacement) and observed displacement (i.e., the detector output) are obtained:

$$\overline{S}_{uu}(\omega) = \frac{\overline{S}_{F_nF_n}/(m\omega_0^2)^2 + g^2|H_{FB}|^2\overline{S}_{u_nu_n}}{\left|1 - \left(\frac{\omega}{\omega_0}\right)^2 + \frac{i}{Q_0}\frac{\omega}{\omega_0} - gH_{FB}(\omega)\right|^2}, \tag{67}$$

$$\overline{S}_{vv}(\omega) = \frac{\overline{S}_{F_nF_n}/(m\omega_0^2)^2 + \left|1 - \left(\frac{\omega}{\omega_0}\right)^2 + \frac{i}{Q_0}\frac{\omega}{\omega_0}\right|^2\overline{S}_{u_nu_n}}{\left|1 - \left(\frac{\omega}{\omega_0}\right)^2 + \frac{i}{Q_0}\frac{\omega}{\omega_0} - gH_{FB}(\omega)\right|^2}. \tag{68}$$

The resonator displacement PSD $\overline{S}_{uu}$ shows that the resonator indeed responds to the force noise with the modified transfer function $H'_R$ instead of $H_R$. The force noise that drives the resonator (i.e., the numerator of the right-hand side of Eq. 67)

[31] The gain $g$ and filter $H_{FB}$ are defined such that $|H_{FB}(\omega_0)| = 1$. Both $g$ and $H_{FB}$ are dimensionless.

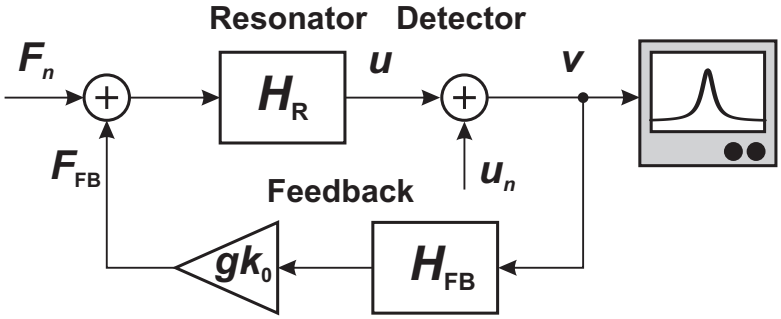


Figure 22: Linear system representation of the active feedback cooling scheme. The resonator displacement $u$ is converted by detector to its output signal $v$. This adds imprecision noise $u_n$ and the sum of this noise and the physical displacement is the signal that is measured, for example using a spectrum analyzer. This signal $v$ is also fed back to the resonator to attenuate the Brownian motion. In the feedback loop a filter with response $H_{FB}$ and a variable gain $g \cdot k_0$ are included. The resulting feedback force $F_{FB}$ adds up with the (thermal) force noise $F_n$. The resonator's response to the applied forces is determined by its transfer function $H_R = H_{HO}/k_0$.

still contains the original contribution $S_{F_nF_n}$, but now it also has a contribution due to the imprecision noise that is fed back to the resonator. Since the latter is always positive, the feedback loop adds additional force noise to the resonator. The apparent position PSD is also modified: It is not simply the sum of $\overline{S}_{uu}$ and $\overline{S}_{u_nu_n}$ because the feedback creates correlations between the imprecision noise $u_n(t)$ and the actual resonator position $u(t)$.

So far, the analysis was general for any linear feedback system and different implementations of the feedback filter $H_{FB}$ are possible, each with their advantages and drawbacks. Using optimal control theory, the best feedback filter can in principle be found [213]. In practise, often simpler, but therefore suboptimal, filters are used. The PSDs of the true and apparent resonator displacement are plotted in Fig. 23 for the two simplest feedback schemes:

- Velocity-proportional feedback where the measured displacement is used to apply a velocity-dependent force on the resonator with $h_{FB}(t) = -\omega_0^{-1} \cdot \partial/\partial t$, $H_{FB} = -i\omega/\omega_0$. In this case the damping rate increases from $\gamma_0$ to $\gamma_0 \cdot (1 + gQ_0)$ as indicated by Eq. 66. Figure 23a shows that at low gains, $\overline{S}_{uu}$ is lowered and thus that the resonator is cooled. However, when the gain is increased further, the tails of $\overline{S}_{uu}$ start to rise as the detector noise (the second term in the numerator of Eq. 67) is fed back into the resonator. Above a certain value $g = g_{\min}$, too much detector noise is fed back to the resonator and the resonator temperature increases again. Figure 24 shows the resonator temperature as a function of the feedback gain. The minimum resonator temperature in the limit $g \gg Q_0^{-1}$ is [43]:

$$T_{R,\min} = \sqrt{\frac{m\omega_0^3 T}{k_B Q_0}\overline{S}_{u_nu_n}} = \frac{2T}{\sqrt{\mathrm{SNR}}}, \text{ for } g = g_{\min} = \sqrt{\mathrm{SNR}}/Q_0. \tag{69}$$

  The minimum resonator temperature is thus set by the signal-to-noise ratio ($\mathrm{SNR} \equiv \overline{S}_{uu}(\omega_0)_{g=0}/\overline{S}_{u_nu_n}$) of the original thermal noise peak and the detector noise floor, as was illustrated in Fig. 18b. Finally, note that, unlike for backaction cooling, the resonator temperature does not saturate at a certain value when $g \to \infty$. Eventually more and more noise is added and the resonator temperature keeps on increasing with increasing gain.

- Displacement-proportional feedback where the displacement is directly fed back to the resonator, which is characterized by $h_{FB}(t) = -\delta(t)$, $H_{FB} = -1$. This changes the spring constant from $m\omega_0^2$ to $m\omega_0^2(1 + g)$ and the resonance frequency to $\omega_0 \cdot (1 + g)^{1/2}$. The stiffening of the resonator reduces its thermal motion and hence its temperature, but to achieve the same cooling factor as with the velocity-proportional feedback the gain should be $Q_0$ times larger. This, however, also feeds back much more detector noise to the resonator in the usual situation where $Q_0 \gg 1$. Cooling can therefore only be achieved when the SNR is large. Figure 23b shows that only heating instead of cooling is achieved for the choice of the parameters used to perform the calculation. For high-Q resonators velocity-proportional feedback is superior to displacement-proportional feedback.

It is important to note that the feedback creates correlations between the resonator displacement and the detector imprecision noise, which lead to a substantial change in the shape of the noise spectra. Figure 23 shows calculated noise power spectral densities for different gains. Without feedback (i.e., $g = 0$) the spectrum of the apparent motion is simply the sum of that of the harmonic oscillator, $\overline{S}_{uu}$, and a constant background level due to the noise, $\overline{S}_{u_nu_n}$. The Figure shows that, even though the peaks in $\overline{S}_{uu}$ only become broader or shift in frequency, the peaks in $\overline{S}_{vv}$ becomes distorted when the feedback is applied. The resonator temperature is no longer simply given by the area under the peak in $S_{vv}$ due to the abovementioned correlations between $u_n$ and $u$. For large gains it is even possible that the peak in the spectrum $\overline{S}_{vv}$ changes into a dip (Fig. 23a). A way to circumvent this problem of determining the resonator temperature, is to use a

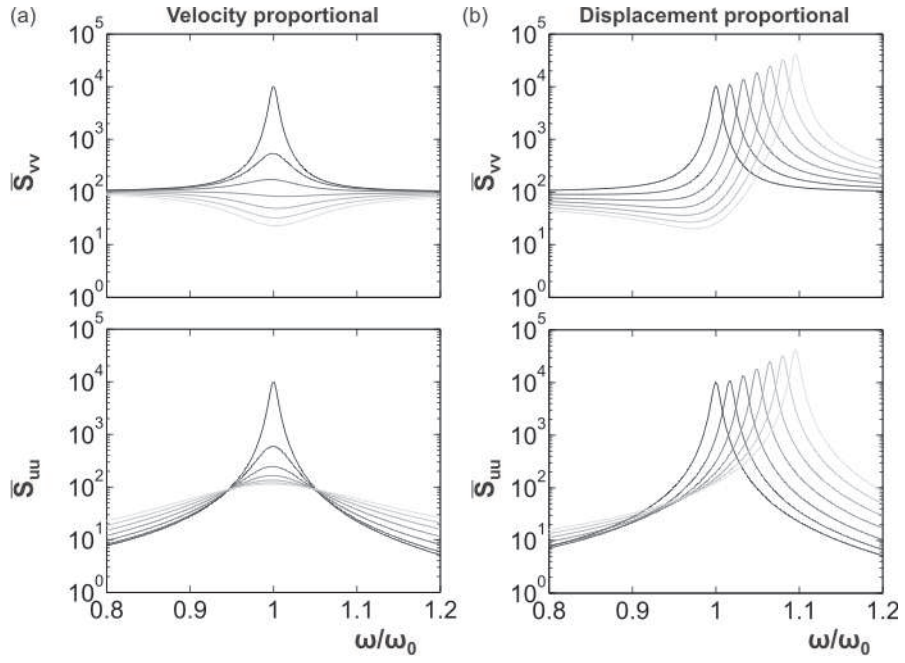


Figure 23: Feedback cooling of a resonator with $Q_0 = 100$ using velocity-proportional (a) and displacement-proportional (b) feedback. The top panels show the PSD of the observed displacement (i.e., that of the detector output) $\overline{S}_{vv}$ and the bottom panels show the real (physical) displacement PSD, $\overline{S}_{uu}$. The gain is stepped from $g = 0$ (black) to $g = 0.2$ (light gray). These plots are calculated with $\overline{S}_{u_n u_n} = 10^2$ and all PSDs are scaled by $\overline{S}_{F_n F_n}/(m\omega_0^2)^2$.

second detector to measure the resonator motion [58]. The noise of the second detector is not correlated with that of the resonator and the measured PSD is again the sum of a constant background and the resonator motion.

Active feedback cooling experiments have mainly been done on resonators in the kHz range, where one can simply measure the position, differentiate and feed the resulting signal back to the resonator. Cohadon *et al.* demonstrated the first active cooling of a mirror using feedback control [219]. They use a high-finesse cavity with a coated plano-convex resonator as the end mirror. A feedback force is applied using a 500 mW laser beam. An acousto-optical modulator is used to control the exerted radiation pressure on the resonator. Next, Kleckner and Bouwmeester actively cooled a 12.5 kHz AFM cantilever from room temperature to 0.135 K [34]. A tiny plane mirror attached to the cantilever served as the movable end mirror of the cavity and again a second high-power laser was used to apply the velocity proportional force. Arcizet *et al.* cooled a millimetre-scale resonator in an optical cavity to 5 K by applying an electrostatic feedback force on the resonator [36]. By using a piezo element to apply feedback to an ultrasoft silicon cantilever cantilever cooling from 2.2 K to 5 mK was demonstrated by Poggio and coworkers [43]. Feedback cooling has also been demonstrated with the gravitational-wave detectors AURIGA [53] and LIGO [64]. In the former experiment the 2 ton heavy detector was cooled from 4 K to 0.17 mK. The motion of the bar is measured capacitively using a resonant electric circuit coupled to a SQUID amplifier. The output of the amplifier is put through a low-pass filter to create the $\pi/2$ phase shift required for

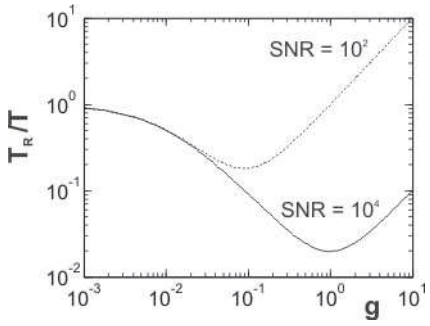


Figure 24: Resonator temperature for velocity-proportional feedback vs feedback gain $g$ for a resonator with $Q_0 = 100$. The dotted line is for $k_0^2\overline{S}_{u_n u_n}/\overline{S}_{F_n F_n} = 10^2$ which gives a signal-to-noise ratio of $10^2$ and the solid line is for $k_0^2\overline{S}_{u_n u_n}/\overline{S}_{F_n F_n} = 1$, with SNR = $10^4$. For low gains the two curves overlap. When $g \gtrsim 0.1$, the detector noise already starts to heat the resonator for the low-SNR curve, whereas the high-SNR curve still decreases. As predicted by Eq. 69 the minimum temperature is lower in the latter case, and this occurs at a higher gain.

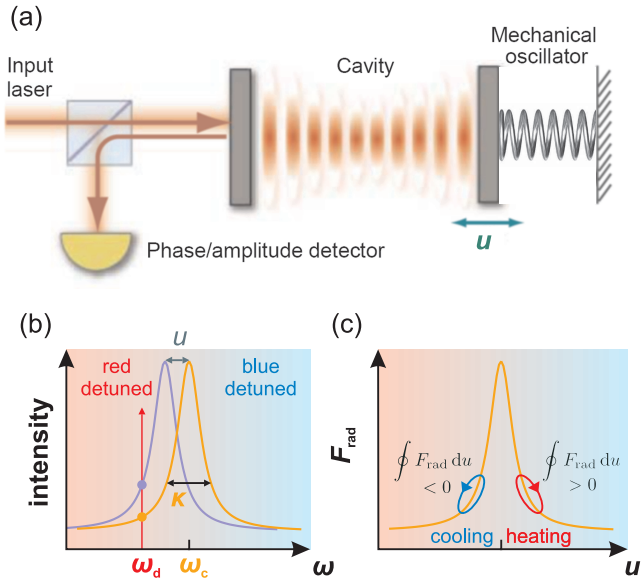


Figure 25: (a) schematic overview of an optical cavity. The cavity is driven via an input laser with frequency $\omega_d$. The left mirror is fixed, but the right mirror is a mechanical resonator that can move. The resonator displacement $u$ determines the length of the cavity and thus the cavity resonance frequency $\omega_c$. A part of the circulating power is transmitted by the left mirror to a detector. The linewidth of the cavity is $\kappa$. From T. J. Kippenberg, K. J. Vahala, Science 321 (2008) 1172–1176. Reprinted with permission from AAAS. (b) When the cavity is driven on its resonance, the intensity inside the cavity is largest, a detuning reduces the intensity. A displacement of the resonator shifts the cavity resonance (purple) and changes the intensity of the light inside the cavity (orange and purple dots). (c) The displacement dependence of the radiation pressure $F_{\rm rad}$. When the resonator oscillates, the force reacts with a delay due to a finite value of $\kappa$ as indicated by the ellipsoidal trajectories.

velocity proportional feedback and then injected into the electronic circuit. In the latter experiment the center-of-mass motion of the four mirrors of a Fabry-Perot cavity with 4 km long arms is reduced from room temperature to only 1.4 $\mu$k. This is done by adjusting the servo control of the mirrors, which creates a velocity-proportional feedback force in the right frequency range without affecting the very high signal-to-noise ratio.

When the resonator frequencies are high, say above 1 MHz, delays in the feedback circuit start to play a role. The force is then applied when the resonator has already advanced and a purely velocity-proportional feedback will have a displacement-proportional component, degrading the cooling performance. The effect of a delay is even more dramatic when it equals half the resonator period, so that the Brownian motion is actually amplified instead of attenuated. Furthermore, the bandwidth (or sampling speed in the case of a digital filter) of $H_{FB}$ should be at least a few times $\omega_R$, which is often not an issue for $\omega_R \lesssim 1\,$MHz. However, active feedback cooling has been reported for MHz resonators by either adjusting the delay [58] of the signal, or using a mixer circuit to down-convert the mechanical signal to a lower frequency [70]. Finally, note that feedback can also have other purposes than cooling. Examples are the regulation of the motion of soft cantilevers as mentioned at the beginning of this section, and feedback can be used to modify or null the nonlinearity of a resonator [220].

### *3.5.3. Sideband cooling*

Another commonly used cooling technique is sideband cooling [221, 222, 223]. In this technique the resonator is embedded in an optical [33, 61, 37, 49, 35, 39, 46, 47, 60, 63, 62] or microwave cavity [44, 50, 56, 68, 23]. These detection schemes will be discussed in detail in Sec. 4, but here a brief introduction is given. Figure 25a shows a schematic drawing of an optical cavity where the right mirror is the mechanical resonator. Both mirrors have a low transmission so that a photon is reflected many times before it can go out through the left mirror, and then toward the detector. Such a cavity has many different optical eigenmodes, but here we focus on a single one and denote its resonance frequency by $\omega_c$. In analogy with the Q-factor and linewidth $\gamma_R$ of a mechanical resonator, the cavity has an optical Q-factor $Q_{\rm opt}$ and linewidth $\kappa$. A laser sends light with frequency $\omega_d$ into the cavity. This frequency can be different from the cavity resonance frequency $\omega_c$; the light is then detuned. Because the resonance frequency of the cavity is determined by the cavity length, a displacement of the resonator changes $\omega_c$. As illustrated in Fig. 25b this leads to a change in the intensity (and phase) of the light in the cavity, which results in a change in the detector output. Optical cavities used this way are very sensitive position detectors for two reasons: first, it enhances the intensity of the light by a factor $Q_{\rm opt}$, and secondly it makes the intensity depend strongly on the displacement [222].

Each photon in the cavity carries a momentum $p_{ph} = \hbar\omega_d/c$ whose direction is reversed when it reflects off the mirror. Here $c$ is the speed of light. The resonator thus experiences a kick of $2p_{ph}$ every time a photon reflects, the so-called

radiation pressure. A single round trip of a photon in a cavity of length $L$ takes a time $2L/c$, whereas the average time that a photon spends in the cavity is $\kappa^{-1}$. The total transfer of momentum per photon is thus $p_{tot} = \hbar\omega_c/\kappa L$. The total force exerted on the resonator is also proportional to the number of photons present in the cavity, $n_c$, and equals $F_{\rm rad} = \hbar\omega_c n_c/L$. Note, that $n_c$ is proportional to $\kappa^{-1}$ and to the input power.

The radiation pressure depends on the displacement of the resonator. This is illustrated in Fig. 25c: A small change in $u$ changes the cavity frequency $\omega_c$, which in turn leads to a proportional change in radiation pressure. This thus changes the effective spring constant of the resonator to $k_R = k_0 - \partial F_{\rm rad}/\partial u$; the so-called optical spring [224, 225, 226, 227, 228, 39, 229, 230]. Similar to displacement-proportional feedback this can cool the resonator [39, 64, 231] and can even lead to bistability of the resonator position [225]. A much stronger cooling effect is, however, the fact that the number of photons does not respond immediately to a change in displacement, but that they can only slowly leak out of the cavity at a rate $\sim \kappa$. This was first realized [224] and demonstrated [232] by Braginskiĭ and coworkers. When $\kappa \gg \omega_0$, a change in the displacement changes the number of photons instantaneously and $F_{\rm rad}$ follows the orange curve in Fig. 25c. However, a finite value of $\kappa$ causes a delay in the response of the radiation pressure as indicated by the ellipsoids in Fig. 25c. In the case of red-detuned driving ($\omega_d < \omega_c$; the ellipse is traversed counterclockwise) work is done by the resonator so that it loses energy, whereas for blue-detuned driving ($\omega_d > \omega_c$; clockwise trajectory) the resonator gains energy. The increased damping for red detuning cools the resonator, as the backaction temperature associated with the detector is very low [233, 234, 223]. This process is called "dynamical backaction" and the cooling mechanism is called "sideband cooling" because the cavity is driven off-resonance, i.e., on a sideband[32] [236]. Note, that sideband cooling can also be described in the language of backaction cooling (Sec. 3.5.1) as the optical force responds with a delay to the displacement. This is thus a detector response $\lambda_v$ (Fig. 17) with a real (the optical spring) and an imaginary part (the delay).

The ultimate limit on the resonator temperature that can be reached with sideband cooling has been studied using the radiation-pressure Hamiltonian in the rotating-wave approximation [233, 234]:

$$\hat{H} = \hbar\Delta\hat{c}^\dagger\hat{c} + \hbar\omega_0\hat{a}^\dagger\hat{a} + \hbar G_{OM}\hat{c}^\dagger\hat{c}(\hat{a}^\dagger + \hat{a}). \tag{70}$$

Here, $G_{OM} = u_0\partial\omega_c/\partial u$ is the optomechanical coupling rate and $\hat{c}^\dagger$ ($\hat{c}$) is the creation (annihilation) operator for a cavity photon (from (to) a photon with frequency $\omega_d$). $\Delta = \omega_d - \omega_c$ is the detuning of the laser light with respect to the cavity resonance frequency. The quantum mechanical picture of sideband cooling is that a phonon together with a red-detuned driving photon can excite a photon in the cavity. This is a likely process because it up-converts the red-detuned driving photon to a frequency closer to the cavity resonance. This removal of phonons cools the resonator. The opposite process is also possible: a cavity photon can emit a phonon and a lower-frequency photon, thereby heating the resonator. The rate of these two processes depends on the density-of-states of the cavity at $\omega_d + \omega_0$ and $\omega_d - \omega_0$ respectively. If the detuning is at exactly at the mechanical frequency $\Delta = -\omega_0$ and the cavity linewidth is small, the lowest temperatures are obtained. The process is analogues to the doppler cooling of cold atoms. In the good-cavity limit ($\omega_m \gtrsim \kappa$) the lowest resonator occupation is $\overline{n}_{\rm min} = (\kappa/4\omega_0)^2 \ll 1$ [233, 234, 222]. Although the good-cavity limit (also called the resolved-sideband regime) was reached a few years ago [49, 56, 61, 60, 63, 237, 68], ground-state cooling was not immediately demonstrated, due to the fact that the driving could not be increased to sufficiently high powers. The cooling power should be large enough to remove the heat coming from the environment to reach the ground state and the cooling power is proportional to the input power [223]. Table 6 and Fig. 21 show the final thermal occupation numbers that have been reached up to now.

The effects of sideband cooling (i.e., frequency shift, change in damping, and cooling) were first considered in the context of gravitational wave detectors, where the effect was more-or-less viewed as a technical point with limited applications, see Refs. [224, 232, 238] and references therein. The first experiments with the aim of cooling mechanical resonators towards the ground state were reported in 2006 by Arcizet [33] and Gigan [35] cooled resonators with frequencies of a few hundred kHz by modest factors of 30 and 10 respectively. These measurements were done using free-space optical cavities which were in the unresolved sideband regime (i.e., where $\omega_R \ll \kappa$). Schliesser and co-workers used a mircotoroidal resonator vibrating at 58 MHz as cavity (see Sec. 4.1.3) and demonstrated cooling to 11 K [37], which corresponds to an occupation number of $\overline{n} = 4300$. A much larger, gram-scale mirror was cooled to a much lower temperature $T_R = 6.3\,$mK by the LIGO team [39, 40]. The resonator frequency is 1 kHz in this case (this is with the optical spring included, the bare resonance frequency is only 12.7 Hz). The thermal occupation $\overline{n} \sim 10^5$ is therefore higher than the abovementioned experiments by Schliesser. A major step forward was made in 2008 by the Kippenberg group, who were the first to reach the resolved sideband regime [49]. Their 73.5 MHz microtoroidal resonator has a cavity line width of only 3.2 MHz, placing this device deep in the good-cavity limit. The resonator was cooled to $\sim 19\,$K.

It was realized that a way to further cool resonators is to start at a lower temperature, so less phonons have to be refrigerated away to reach the groundstate. This approach was pursued by the group of Lehnert using superconducting stripline resonators (Sec. 4.1.5). Their first experiment was in the unresolved-sideband regime [50], but this was soon

[32] A recent proposal uses a displacement-dependent cavity damping instead of the usual displacement-dependent cavity frequency [235].

superseded by measurements in the good-cavity limit [56], where a 0.237 MHz resonator was cooled from a 50 mK base temperature to 10 mK. Superconduting striplines are of course always operated at low temperature, but recently a lot of effort has been done to place optical cavities at cryogenic temperatures. Gröblacher *et al.* precooled their microresonator to 5 K and subsequently cooled the 1 MHz resonator to 1.3 mK, where $\overline{n} = 32$ [60]. Around the same time, Schliesser *et al.* cooled a resonator placed in a cryostat from 1.7 K to 0.2 K where $\overline{n} = 63$. Very recently, the first actively cooled device with an occupation number smaller than one was demonstrated by Teufel *et al.* [23]. They employed sideband cooling in a resonant superconducting circuit.

### *3.5.4. Concluding remarks*

In the previous Subsections backaction cooling, active feedback cooling, and sideband cooling have been discussed. Although it might appear that these methods are unrelated, the converse is true: From the linear system representation of backaction (Fig. 17) and that of active feedback cooling (Fig. 22), it is clear that they are closely related. In the former case the delayed force, needed to achieve the largest cooling factors, is caused directly by the detector, whereas in the latter it is actively exerted by the experimenter. The coupling $A$ and the gain $g$ play the same role in the respective pictures, and so do the detector force response $\lambda_F$ and the feedback filter $H_{FB}$. Also, the lowest temperature that can be reached is determined by the noise, $\Phi_{det,n}$ and $u_n$ respectively. Note, however, that for backaction cooling the resonator approaches $T_{BA}$ when the coupling $A \to \infty$, whereas in the case of active feedback cooling the resonator temperature diverges for $g \to \infty$, and the minimum temperature occurs at a finite value of the feedback gain. It was also shown that one can describe sideband cooling in a similar fashion: namely as the (delayed) response of the optical force to the displacement, and the same is true for bolometric forces where the delayed force is due to the finite heat capacity [31, 41, 211, 239]. Finally, we note that there are cooling mechanisms in non-cavity systems, such as in superconducting single-electron transistors [32, 240] and double dots [241] that are formally identical to sideband cooling.

Another important point is illustrated in the experiments done by Teufel and coworkers (lines 31, 32 in Tables 1 and 6). When cooling the resonator, in this case using sideband cooling [56], the quality factor decreases. The resolution of the detector then degrades when the sensitivity stays the same because the resonator bandwidth $\gamma_R$ increases. In other words, one has less time to average-out the imprecision noise. The opposite occurs when the damping of the resonator is reduced: the resolution is improved, but the resonator temperature increases significantly [66]. In particular, this happens in a cavity optomechanical system for a blue-detuned laser drive, but this effect has also been observed in single-electron transistors [32], superconducting interference devices [242] and in many other detectors. In this regime energy is transferred from the cavity to the mechanical system. The oscillation amplitude grows and the resonance becomes sharper as the resonator energy increases. When the coupling is strong enough, the damping rate can vanish ($\gamma_0 + \gamma_{BA} = 0$) or even become negative. Beyond this instability the resonator exhibits self oscillations that are only bound by nonlinearities in either the resonator or the detector [224], and this can lead to complex nonlinear dynamics. Theoretical work on the classical effects in this regime has been documented in Refs. [243, 244, 245, 246]. Experimentally this instability has been observed in a variety of micro and nanomechanical systems, including microtoroidal resonators [247, 248, 37], Fabry-Perot cavities [33, 228, 40, 239], superconducting stripline resonators [56] and microspheres [249]. Devices that are self oscillating can be useful from an application point of view as ultra-high frequency, low phase-noise oscillators [51], or as memory elements [250].

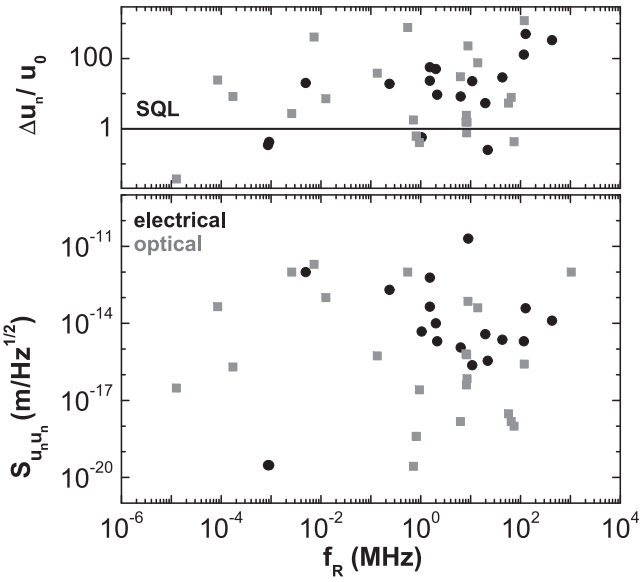


Figure 26: Resolution (top panel) and sensitivity (bottom panel) of the experiments that are listed in Table 7. Experiments with optical (electrical) detection are shown in gray (black) respectively. The solid line indicates the standard quantum limit. As discussed in Sec. 3, detectors can have an imprecision resolution below the quantum limit at the price of a large backaction force noise. There is a trend that the resolution and sensitivity degrades (their value increases) with increasing resonator frequency.

## 4. Detection methods

In this section we discuss the main detection methods for mechanical motion in nanoscale systems or in mechanical devices which aim at reaching the quantum regime. Most methods involve a linear displacement detector, i.e., the output of the detector depends linearly on the displacement of the resonator. As shown in the previous sections, such schemes inevitably introduce backaction on the resonator position, which consequently leads to the fundamental limit on the sensitivity set by quantum mechanics. We will only briefly comment on quadratic (square-law) detectors, as they have not been studied to the same extent as linear detectors. In recent years, tremendous improvement in the sensitivity has been obtained using a variety of different detection methods. Using optical cavities, displacements sensitivities as small as $10^{-20}\,\mathrm{m}/\sqrt{\mathrm{Hz}}$ (see Table 7) have been reached; using mesoscopic electromechanical devices the sensitivity can be as good as $10^{-16}\,\mathrm{m}/\sqrt{\mathrm{Hz}}$. Figure 26a shows the resolution $\Delta u_n$ due to the imprecision noise $\overline{S}_{u_n u_n}$ of the experiments listed in the Table. (For the exact definition of $\Delta u_n$ in this context we refer to Eq. B.7 in Appendix B). Note, that this quantity does not include the effects of backaction force noise and can therefore be substantially smaller than the standard quantum limit as the Figure shows. This is most clearly demonstrated by the relatively low-frequency resonators that are read-out optically [36, 33, 43, 53, 60]. Although the backaction force noise is present to ensure the SQL and thereby heating the resonator; at room temperature, this contribution is masked by the much larger thermal motion. Also in solid-state devices at low temperature, $\Delta u_n < u_0$ has been achieved [32, 66, 68] and there an increase in resonator temperature due to backaction is seen [32].

The most straightforward method to analyze the data measured in an experiment is to record the output of the linear detector as a function of time; for a photodetector in a cavity experiment (Sec. 4.1) this would be an output current and for a dc SQUID position detector (Sec. 4.5) this is the voltage over the SQUID. This signal can be fed to a spectrum analyzer and from the measured spectrum, the resonance frequency and Q-factor can directly be obtained in the linear response. From the thermal noise spectra (cf. Fig. 18b) other parameters like $S_{u_n u_n}$, $S_{F_{tot}F_{tot}}$ can be obtained as illustrated in the Figure.

An important issue in measuring the resonator dynamics is the available bandwidth of the setup. In particular this holds for the solid-state devices that often have a high impedance ($\gg 50\,\Omega$). The combination of high impedances and unavoidable stray capacitances can lead to RC times that are smaller then the resonator period $1/f_R$. There are several ways to circumvent this problem: frequency mixing, impedance matching using tank circuits, or using low-impedance devices such as superconducting quantum interference devices (SQUIDs) and microwave striplines. Yet another way relies on self-detection which yield dc information about the vibrational motion, e.g. rectification and spectroscopy measurements. These (non-linear) methods are mainly used in bottom-up devices.

In the following sections, we will discuss different detection schemes focusing on the resonator-detector coupling and on the backaction mechanism. As we concentrate on detection schemes aimed at the quantum regime, we will, for example, not consider piezo-resistive detection schemes, which are very common in MEMS and for applications, but

Table 7: Overview of the sensitivity and resolution of recent experiments. The table shows the type of detector that was used, and the displacement-imprecision noise $S_{u_n u_n}$ from which the resolution $\Delta u_n$ is calculated. The ratio of the resolution to the zero-point motion $u_0$ is also stated. The numbers of the first column correspond to the experiments listed in Table 1 and Table 6.

| | **Detector** | $\mathbf{S_{u_n u_n}}$ fm/ $\sqrt{\text{Hz}}$ | $\mathbf{\Delta u_n}$(fm) | $\mathbf{\Delta u_n / u_0}$ | **Ref.** |
|---|---|---|---|---|---|
| 1 | Magn. mot. | | | | [28] |
| 2 | SET | 2.0 | 658 | 130 | [29] |
| 3 | SET | 3.8 | 113 | 5.4 | [30] |
| 4 | Opt. cav. | $2.0 \cdot 10^3$ | $4.8 \cdot 10^3$ | 415 | [31] |
| 5 | SET | 0.35 | 5.9 | 0.25 | [32] |
| 6 | Opt. cav. | $4.0 \cdot 10^{-4}$ | $4.5 \cdot 10^{-3}$ | 0.62 | [33] |
| 7 | Opt. cav. | 100 | 38 | 7.2 | [34] |
| 8 | Opt. cav. | | | | [35] |
| 9 | Opt. cav. | $4.0 \cdot 10^{-4}$ | $4.5 \cdot 10^{-3}$ | 0.62 | [36] |
| 10 | Opt. cav. | $3.0 \cdot 10^{-3}$ | 0.53 | 5.4 | [37] |
| 11 | Piezoresist. | 39 | $1.8 \cdot 10^4$ | 506 | [38] |
| 12 | Opt. cav. | 0.2 | 0.06 | 8.3 | [39] |
| 13 | Opt. cav. | 0.03 | $9.5 \cdot 10^{-4}$ | 0.04 | [40] |
| 14 | Opt. cav. | $1.0 \cdot 10^3$ | $2.8 \cdot 10^4$ | 778 | [41] |
| 15 | APC | 2.3 | 268 | 29 | [42] |
| 16 | Opt. cav. | $1.0 \cdot 10^3$ | 271 | 2.7 | [43] |
| 17 | MW res. | | | | [44] |
| 18 | Opt. cav. | $2.7 \cdot 10^{-5}$ | $2.3 \cdot 10^{-4}$ | 1.8 | [45] |
| 19 | Opt. cav. | 0.54 | 49 | 39 | [46] |
| 20 | Opt. cav. | | | | [47] |
| 21 | Opt. cav. | 45 | 2.5 | 25 | [48] |
| 22 | Opt. cav. | $1.0 \cdot 10^{-3}$ | 0.05 | 0.42 | [49] |
| 23 | Stripline | 200 | $2.5 \cdot 10^3$ | 19 | [50] |
| 24 | Magn. mot. | 12.8 | $6.6 \cdot 10^3$ | 339 | [51] |
| 25 | QPC | $1.0 \cdot 10^3$ | 588 | 20 | [52] |
| 26 | SQUID | 10 | 132 | 51 | [19] |
| 27 | Capacitive | $3.0 \cdot 10^{-5}$ | $1.0 \cdot 10^{-6}$ | 0.34 | [53] |
| 28 | Capacitive | $3.0 \cdot 10^{-5}$ | $1.2 \cdot 10^{-6}$ | 0.42 | [53] |
| 29 | Opt. cav. | $1.0 \cdot 10^3$ | $9.5 \cdot 10^6$ | $4.8 \cdot 10^5$ | [54] |
| 30 | Opt. trans. | 72 | $6.2 \cdot 10^3$ | 232 | [55] |
| 31 | Stripline | 600 | $1.7 \cdot 10^3$ | 57 | [56] |
| 32 | Stripline | 45 | 696 | 23 | [56] |
| 33 | Capacitive | $2.0 \cdot 10^4$ | $1.9 \cdot 10^5$ | $8.5 \cdot 10^3$ | [57] |
| 34 | Opt. cav. | $1.5 \cdot 10^{-3}$ | 0.2 | 30 | [58] |
| 35 | Opt. trans. | 40 | $2.8 \cdot 10^3$ | 76 | [59] |
| 36 | Opt. cav. | 0.03 | 0.18 | 0.4 | [60] |
| 37 | Opt. cav. | $1.5 \cdot 10^{-3}$ | 0.34 | 7.9 | [61] |
| 38 | Opt. trans. | 0.04 | 11.7 | 2.4 | [62] |
| 39 | Opt. cav. | 0.26 | 61 | $1.2 \cdot 10^3$ | [63] |
| 40 | Opt. cav. | $1.0 \cdot 10^{-3}$ | | | [64] |
| 41 | Opt. cav. | 0.07 | 4.0 | 1.5 | [65] |
| 42 | Stripline | 4.8 | 15 | 0.57 | [66] |
| 43 | Opt. cav. | 0.64 | 23 | 1.6 | [67] |
| 44 | Stripline | 1.2 | 209 | 8.3 | [68] |
| 45 | Opt. cav. | 0.6 | 12.5 | 0.76 | [69] |
| 46 | Qubit | | | | [22] |
| 47 | SQUID | 2.0 | 24 | 9.3 | [70] |
| 48 | MW res. | 0.23 | 92 | 23 | [23] |

rarely used for nanoscale experiments [38, 251]. The main disadvantage of this method is that it requires a large current that is dissipated in the resonator.

### *4.1. Cavities*

Table 8: Overview of the coupling factors reached in optical and microwave cavity experiments. As explained in the text $g_{OM} = \partial\omega_c/\partial u$ quantifies how much the cavity frequency changes with the displacement and $G_{OM} = g_{OM} \times u_0$ is the vacuum coupling rate. The cavity frequency $\omega_c/2\pi$ lies in the GHz range for the microwave cavities and is $\sim 10^2$ THz for the optical cavities. $\kappa$ is the cavity linewidth. In the experiment on the last line, a superconducting qubit is used instead of a cavity. In this case, the value of vacuum Rabi rate is listed as an estimate of $G_{OM}$ [22].

| **Group** | $\frac{g_{OM}}{2\pi}\left(\frac{\text{MHz}}{\text{nm}}\right)$ | $\frac{G_{OM}}{2\pi}$ (Hz) | $\frac{\omega_c}{2\pi}$ (GHz) | $\frac{\kappa}{2\pi}$ (MHz) | $\mathbf{L}_{OM}$ (m) | **Ref.** |
|---|---|---|---|---|---|---|
| JILA | $1.16 \cdot 10^{-3}$ | 0.15 | 4.91 | 0.49 | $4.23 \cdot 10^{-3}$ | [50] |
| JILA | $4.60 \cdot 10^{-3}$ | 0.14 | 5.22 | 0.23 | $1.13 \cdot 10^{-3}$ | [56] |
| JILA | $3.20 \cdot 10^{-2}$ | 0.86 | 7.49 | 2.88 | $234 \cdot 10^{-6}$ | [66] |
| Schwab | $7.50 \cdot 10^{-3}$ | 0.18 | 5.01 | 0.49 | $668 \cdot 10^{-6}$ | [252] |
| Schwab | $8.40 \cdot 10^{-2}$ | 2.12 | 7.48 | 0.60 | $89.0 \cdot 10^{-6}$ | [68] |
| Aalto | 1.0 | 16.5 | 7.64 | | $7.64 \cdot 10^{-6}$ | [253] |
| NIST | 56 | 226 | 7.47 | 0.17 | $133 \cdot 10^{-9}$ | [254] |
| NIST | 49 | 198 | 7.54 | 0.20 | $154 \cdot 10^{-9}$ | [23] |
| Vienna | $1.13 \cdot 10^2$ | 206 | $2.82 \cdot 10^5$ | 120 | $2.50 \cdot 10^{-3}$ | [35] |
| LKB Paris | $1.17 \cdot 10^2$ | 75 | $2.82 \cdot 10^5$ | 2.08 | $2.40 \cdot 10^{-3}$ | [36] |
| LKB Paris | $1.48 \cdot 10^2$ | 0.020 | $3.70 \cdot 10^5$ | 0.26 | $2.50 \cdot 10^{-3}$ | [45] |
| Harris | 2.1 | 2.68 | $2.82 \cdot 10^5$ | 0.32 | 0.13 | [46] |
| Vienna | 15 | 6.98 | $3.85 \cdot 10^5$ | 0.20 | $25.0 \cdot 10^{-3}$ | [60] |
| MPI-QO | $1.40 \cdot 10^4$ | 599 | $3.85 \cdot 10^5$ | 19 | $27.5 \cdot 10^{-6}$ | [61] |
| Painter | $1.23 \cdot 10^5$ | $5.99 \cdot 10^5$ | $1.94 \cdot 10^5$ | 646 | $1.58 \cdot 10^{-6}$ | [62] |
| Painter | $3.38 \cdot 10^4$ | $8.79 \cdot 10^4$ | $1.97 \cdot 10^5$ | 113 | $5.84 \cdot 10^{-6}$ | [65] |
| Vienna | 11 | 2.70 | $2.82 \cdot 10^5$ | 0.22 | $25.0 \cdot 10^{-3}$ | [237] |
| MPI-QO / LMU | 10 | 145 | $1.94 \cdot 10^5$ | 4.90 | $19.4 \cdot 10^{-3}$ | [67] |
| Cornell | $9.35 \cdot 10^3$ | | $2.00 \cdot 10^5$ | 2943 | | [127] |
| MPI-QO / LMU | 40 | 660 | $3.53 \cdot 10^5$ | | $8.82 \cdot 10^{-3}$ | [69] |
| MPI-QO | $1.20 \cdot 10^4$ | $1.08 \cdot 10^3$ | $3.87 \cdot 10^5$ | 15 | $32.3 \cdot 10^{-6}$ | [255] |
| MPI-QO | | $2.68 \cdot 10^5$ | $1.93 \cdot 10^5$ | $2.0 \cdot 10^4$ | | [256] |
| Cornell | $6.00 \cdot 10^4$ | $7.32 \cdot 10^5$ | $1.89 \cdot 10^5$ | $1.0 \cdot 10^4$ | $3.14 \cdot 10^{-6}$ | [230] |
| UCSB | | $6.20 \cdot 10^7$ | 6.17 | 9.36 | | [22] |

The most popular and sensitive technique in optomechanics involve optical cavities. There are several reviews about this topic, see e.g. Refs. [257, 221, 258, 222] and we will only discuss the basic features of these devices. In a cavity, photons bounce back and forth many times before they are absorbed or escape the cavity. During this time, the light interacts with the resonator and the total interaction strength depends on the number of times that the photon reflects inside the cavity; the so-called finesse $\mathcal{F}$. The light that eventually comes out of the cavity contains the displacement signal, enabling position detection. Also, when the light interacts with the resonator, the photons exert a backaction force on the resonator; the radiation pressure that was introduced in Sec. 3.5.3. Different types of optical cavities exist that we will treat separately in the next Subsections. Cavities cannot only be realized in the optical domain where the frequencies are hundreds of THz, but they can also be made with superconducting resonant circuits that operate in the microwave frequency range (GHz). At the end of this section we will introduce these microwave cavities and compare them to their optical equivalents.

An important figure of merit for cavity-optomechanical systems is the coupling strength, which is usually defined as $g_{OM} = \partial\omega_c/\partial u$. It indicates how much the cavity frequency shifts per unit motion. Table 8 shows the coupling strength, the cavity frequency, its damping rate, and some derived quantities for recent experiments with optical and microwave cavities: The optomechanical coupling length is defined as $L_{OM} = \omega_c/g_{OM}$, which equals the physical cavity length in the case of a Fabry-Pérot cavity. $L_{OM}$ is a convenient quantity as the displacement normalized by it, directly gives the relative change in cavity frequency: $u/L_{OM} = (\omega_c(u) - \omega_c(0))/\omega_c(0)$. To obtain a high optomechanical coupling it is thus advantageous to have a small cavity. In the experiments reported in Refs. [35, 36, 45] the Fabry-Pérot cavity length is only a few millimeters. The coupling rate that appears in the cavity-resonator Hamiltonian (Eq. 70) has been introduced as $G_{OM} = g_{OM}u_0$, which indicates how much the cavity moves due to the zero-point motion of the resonator and this

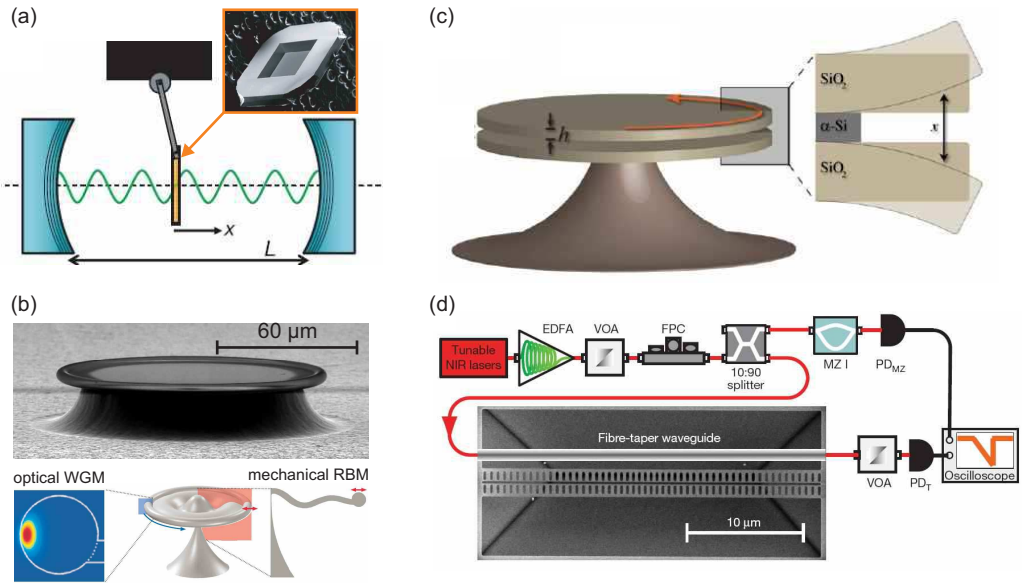


Figure 27: Different implementations of optical cavities for position detection. (a) Schematic overview of an optical cavity with a movable membrane in it. The cavity consists of two fixed mirrors at a distance $L$. The membrane at position $x$ can be located at different intensities of the standing wave in the cavity (green). The membrane (inset) is made of 50 nm thick silicon nitride and is held by a silicon substrate. The membrane reflectivity is $r_c = 0.42$. Reprinted by permission from Macmillan Publishers Ltd: Nature 452, 72–75, copyright 2008. (b) Top: scanning electron micrograph of a microtoroid. Bottom: schematic illustration of the optical whispering gallery mode (WGM) and the mechanical radial breathing mode (RBM). The WGM encircles the toroid and is mainly located at the rim. In RBM vibrations the rim of the toroid moves outward, thereby elongating the WGM cavity length. Adapted from Refs. [261] and [122]. Reprinted by permission from Macmillan Publishers Ltd: Nature 421, 925–928, copyright 2003. (c) Artist impression of a double-disk cavity. The cavity consists of two silica disks separated by a layer of amorphous silicon. Similar to the microtoroid in panel (c), WMGs exist in each of the two disks. They from bonded and antibonded modes (modes with even and odd parity respectively). The mechanical mode of interest is that where the gap between the two disks changes. Reprinted figure with permission from Q. Lin *et al*, Phys. Rev. Lett. 103 (2009) 103601. Copyright 2009 by the American Physical Society. (d) The setup used to study the mechanics and the optical properties of the zipper cavity. Near-infrared (NIR) laser light goes through an erbium-doped fiber amplifier (EDFA) and a variable optical attenuator (VOA). The polarization is adjusted in the fiber-polarization controller (FPC) and the light is split in two paths: one through a fiber Mach-Zehnder interferometer (MZI) and the other through a tapered fiber that couples the light to the zipper cavity. Finally, the photons in both paths are detected with photodetectors (PD). Reprinted by permission from Macmillan Publishers Ltd: Nature 459, 550–555, copyright 2009.

coupling rate is sometimes called the vacuum coupling rate [259]. The role of this quantity becomes clear when one considers a quantum state in which both the mechanical resonator and the cavity are in an eigenstate of the individual subsystems. In the uncoupled system (i.e., for $G_{OM} = 0$) the system remains in this state since it is also an eigenstate of the total Hamiltonian. However, this is no longer the case in the *coupled* system. The state will then oscillate between states with more energy in the mechanical resonator and states with more photons in the cavity. The rate at which this happens is proportional to $G_{OM}$. Note that this is very similar to Rabi oscillations in a two-level system coupled to a cavity [260]. Furthermore, the Hamiltonian in Eq. 70 shows that the optomechanical coupling is related to the backaction: the force exerted by a single photon in the cavity is $\hbar g_{OM}$, which can be as large as 13 fN for the on-chip cavities that we will encounter in Sec. 4.1.4. Finally, we note that the coupling strengths $g_{OM}$ and $G_{OM}$ are solely determined by the device geometry and are independent of the optical and mechanical Q-factors.

### *4.1.1. Fabry-Pérot cavities*

A schematic picture of a typical Fabry-Pérot setup has already been shown in Fig. 25a and was discussed in Sec. 3.5.3. Briefly, the cavity consists of two mirrors, one of which can move, whereas the other one is fixed. When the moveable mirror is displaced, the cavity length changes and therefore also the cavity resonance wavelength. An important property of the cavity is the reflectivity of the mirrors. A large reflectivity means that the optical quality factor[33] is high, i.e., the light bounces back and forth many times so that the interaction between mechanical motion and the photon is strongly enhanced. A small fraction of the light is allowed to come out of the cavity and is guided to a photo-detector. These can detect individual photons and therefore the position detection sensitivity can be shot noise limited.

There are two main implementations to measure the light that comes out of the cavity. The first method, shown in Fig. 25a, uses a polarized beam splitter in combination with a $\lambda/4$-plate to separate the incoming laser light from the light that

[33]The quality factor indicate the number of oscillations of the optical field before it leaves the cavity or before it is dissipated. In optics, one usually speaks about the finesse $\mathcal{F}$ of the cavity, which is the number of *reflections* of the field before it is lost. The finesse is related to the optical quality factor: $\mathcal{F} \equiv \Delta\omega_c/\kappa = Q \times \Delta\omega_c/\omega_c$. Here, $\Delta\omega_c$ is the free spectral range of the cavity, i.e. the distance between subsequent cavity resonances ($\Delta\omega_c = \pi c/L$). Typical numbers for $\mathcal{F}$ range from $10^3$ to $10^5$ for high-quality cavities [222].

comes out of the cavity. The advantage of this setup is its compactness. The second setup consists of two arms with cavities that are illuminated by a single laser via a beam splitter. Light that comes out of the two arms interferes destructively at the beam splitter when the length of the two arms is identical. However when one of the mirrors displaces, this is no longer the case and photons arrive at the photo-detector. This implementation is a so-called Michelson interferometer and is used to search for gravitational waves [262]. With two 4 km arms, displacements of kg-scale resonators (i.e., mirrors) are detectable to within $10^{-19}\,\mathrm{m}/\sqrt{\mathrm{Hz}}$ [64].

For a Fabry-Pérot cavity the coupling constant is $g_{OM} = \omega_c/L$, where $L$ is the cavity length [122] as explained in Sec. 4.1. For a cm-long cavity and light with a visible wavelength this gives $g_{OM} \sim 2\pi \cdot 10\,\mathrm{MHz/nm}$ (see Table 8). In the presence of a strong coherent pump laser, the *effective* coupling rate is enhanced by the square root of the number photons in the cavity $\sqrt{n_c}$. The optomechanical strong coupling regime where $G_{OM} \cdot n_c^{1/2} \gg \omega_R, \kappa_c$ was first reached in a 25 mm long Fabry-Pérot cavity [237], as evidenced by the mode splitting [263] of the mechanical resonator and the detuning of the cavity. Strong coupling has now also been demonstrated in other optomechanical systems [254, 255, 264].

Fabry-Pérot cavities are very sensitive position detectors and have already been used for a while to approach the quantum limit on position detection, see for example Ref. [209]. Their properties (shot-noise limited sensitivity, backaction etc.) are therefore well known. The most sensitive implementation of the Fabry-Pérot interferometer reaches the impressive sensitivity of $10^{-20}\,\mathrm{m}/\sqrt{\mathrm{Hz}}$ for the motion of the differential motion of the two mirrors forming a 0.25 mm long cavity with a finesse of 230 000 [45]. Currently, a lot of effort is put in reaching true strong coupling where $G_{OM} > \kappa, \omega_R$ and in the observation of quantum backaction [265, 266].

*4.1.2. Movable membrane inside the cavity*

Another use of cavities in optomechanics, is the setup pioneered by the group of Harris, where a flexible membrane is positioned inside a rigid cavity [46]. A schematic drawing of this setup is shown in Fig. 27a. One of the advantages of this implementation is that the mechanical resonator and the mirrors of the cavity are separated, so that a high-quality cavity can be made without degrading the mechanical properties of the resonator. The membrane, with a low (field) reflectivity $r_c$, can be positioned at different locations $x$ inside that cavity, i.e., at nodes or at anti-nodes of the standing light-field waves. Depending on where the membrane is placed, the coupling is different: At an anti-node, the membrane strongly interacts with the cavity, whereas at a node, it does not. In a way this system can be viewed as two coupled cavities. For a particular optical mode, the light is predominantly on one side of the membrane exerting a radiation pressure on it from that side. From the above it is clear that the cavity frequency $\omega_c$ should be a periodic function of the membrane position $x_m$ and so is the optomechanical coupling. Using a one-dimensional model [46] the coupling strength is obtained: $g_{OM} \approx 4\pi|r_c|c/(L\lambda)\sin(4\pi x_m/\lambda)$ assuming $|r_c| \ll 1$. This optomechanical system thus exhibits a tuneable coupling.

At a node of the optical field ($x_m = n\lambda/2$), the linear coupling term between the cavity and the resonator vanishes and a small quadratic term remains. Interestingly, this quadratic term can be greatly enhanced by slightly tilting ($\sim 1$ mrad) the membrane [267]. In this case, avoided crossings of different optical cavity modes occur and near these avoided crossings the cavity frequency depends strongly on the position of the membrane squared (i.e., square-law position detection). In the realization of Ref. [267] the tilting results in an increase in the coupling from $30\,\mathrm{kHz/nm^2}$ to $\gtrsim 30\,\mathrm{MHz/nm^2}$, which might enable direct measurements of the quantization of the membrane's energy (see the discussion in Sec. 3 and Appendix C) [268, 269].

*4.1.3. Optical cavities on the micro scale*

As we have discussed before, it is advantageous to have a cavity with a high finesse (or the related optical quality factor, see footnote 33) in combination with a high mechanical Q-factor. In the experiments described in Sec. 4.1.2 this was done by physically separating the mirrors from the mechanical resonator. A different approach is to use microtoroids (see Fig. 27b), which can have optical Q-factors in excess of $10^8$ or equivalently $\mathcal{F} > 10^6$ [261]. Light can be coupled into these devices via free-space evanescent coupling by positioning a tapered fiber close ($\sim 1\,\mu$m) to it [270]. The light travels around the outer edge of the toroid in, what is called, a whispering-gallery mode (WGM) (see Fig. 27b, lower left panel). The light in this mode is strongly coupled to the mechanical vibrations of the toroid, in particular to its radial breathing mode (RBM). In this mode, the toroid expands and retracts in the radial direction, thereby changing its diameter slightly in time. The mechanical RBM frequencies are of the order of 10 to 100 MHz; the mechanical quality factor can be as high as 32000 and depends on the exact device geometry [271]. The coupling length is in this case the toroid radius, $L_{OM} = R$ [122], and the coupling constant $g_{OM} = \omega_c/R$ can reach $2\pi \cdot 10\,\mathrm{GHz/nm}$ (see Table 8). This high value can be understood from the much smaller dimensions of the toroid cavity: The cm-long Fabry-Pérot cavities are now replaced a by toroid with a circumference of a few hundred $\mu$m.

A very similar system are silica microspheres [270, 249, 63], where again the whispering-gallery mode couples strongly to the mechanical breathing modes with a frequency of the order of 100 MHz for a typical diameter of $\sim 30\,\mu$m. The optical quality factor of these devices exceeds $10^7$ and typical values for the mechanical Q-factor are $10^4$. Light is coupled into the WGM by focussing a laser beam close to the sphere. Similar to the fiber taper, the light enters the sphere via the evanescent field and this causes a detectable phase shift in the transmitted light [63].

Cooling has been extensively studied in the microtoroid systems [37, 49, 58] and an advantage is that they can be integrated and precooled to helium temperatures in cryostats [61, 63]. In the latter experiments, thermal occupation numbers as low as $n = 70$ and 37 have been achieved respectively. The small scale of these devices also bears another advantage in that it can be coupled to other mechanical resonator by placing them in the near vicinity of the toroid. An example is described in Refs. [67, 69], in which the flexural modes of a nanomechanical SiN string are probed via the toroid with a position sensitivity that is two times below the standard quantum limit. The coupling $g_{OM}$ decreases exponentially with the distance between the string and the toroid and a maximum value of $g_{OM} = 2\pi \times 10\,\mathrm{MHz/nm}$ has been reported. Finally, it was demonstrated that microtoroid can be actuated electrostatically using gradient forces, making it an optoelectromechanical system [272]. A recent review summarizes the achievements in cavity optomechanics with whispering-gallery modes [122].

*4.1.4. On-chip optical cavities*

A clever way to further increase the optomechanical coupling has been realized by Painter and co-workers [62, 123, 65]. The basic idea is as follows: When placing two optical waveguides in close vicinity (submicron scale), symmetric and anti-symmetric optical modes form with a mode volume of the order of $\lambda^3$. The optical coupling length, $L_{OM}$, can be viewed as the length scale over which a photon's momentum is transferred, which, in this case, is reduced to a length scale of the order of the optical wavelength, $\lambda$. Thus, the coupling can be estimated to be $g_{OM} \sim \omega_c/\lambda$. Since the wavelength is about $1.5\,\mu$m, the coupling can be at least an order of magnitude larger than in the micro-cavities discussed above (see Table 8). Two implementations have been built. In one version [127, 65], a pair of silica (or SiN) disks separated by nanometre-scale gaps was used as shown in Fig. 27c. The coupling depends on the separation between the disks and for an air-gap of 138 nm, the coupling was found to be $g_{OM} = 2\pi \cdot 33\,\mathrm{GHz/nm}$. Efficient cooling of the mechanical mode was achieved [65], and static and dynamic mechanical wavelength routing was demonstrated [231]. Furthermore, Wiederhecker *et al.* demonstrated attractive and repulsive forces between the disks [127] and optomechanical tuning of the cavity modes over more than 30 nm [230] in a similar device.

An even larger coupling is obtained with two stoichiometric silicon nitride ladder structures with a photonic crystal structure ("zipper cavities") as illustrated in Fig. 27d. With a separation of 120 nm between the two waveguides, a coupling of $g_{OM} = 2\pi \cdot 123\,\mathrm{GHz}$ has been achieved [62]. The strong coupling yields a large optical spring effect (see Sec. 3.5.3), where the resonance frequency is mainly determined by the laser field instead of by the structural properties of the resonator. This effect shows up as a change in resonance frequency if the input power and detuning are changed. Interestingly, the optical spring only acts on the differential motion of the beams. The common-mode vibrations are not affected by the light field. By varying the detuning of the driving light, Lin *et al.* could shift the differential mode through the resonance frequency of the common mode. The observed Fano-like lineshape indicates coherent mixing of the mechanical excitations [196].

Another advantage of optomechanical crystals is the control over the location of the optical and mechanical modes [123]. Since the spatial extent of modes differs, the coupling strength can be engineered. Thus, the simultaneous confinement of optical (photonic crystals) and mechanical modes (phononic crystal) leads to strong, controllable light-matter interactions [273]. Finally, note that in on-chip optomechanical devices the optical gradient force is typically much larger than the photon pressure [55, 274, 65, 127, 275].

*4.1.5. Superconducting microwave cavities*

Instead of using an optical cavity, electromagnetic waves can also be confined in a superconducting microwave cavity [276]. The electromagnetic cavity mode is sensitive to capacitive changes and this principle has been used to measure nanomechanical motion [50, 66, 68]. The device used in the first realization of such a transmission-line position detector [50] is shown in Fig. 28.

The working principle is as follows: In the superconducting transmission line with an inductance and capacitance per unit length, radiation propagates. On one side microwaves are injected via a capacitively coupled feedline; the other end can be open or shorted to ground (so-called $\lambda/2$ and $\lambda/4$ microwave cavities respectively). In the first case standing waves with a voltage anti-node at the end form, whereas in the latter case waves with a node at the end form. The mechanical resonator is connected to the stripline and positioned close to the ground plane. Its displacement couples to the cavity capacitance and this in turn changes the cavity resonance frequency which can accurately be probed via transmission or reflectivity measurements. In the realization of the group of Lehnert (i.e., the one shown in Fig. 28) this is done via the transmission of the feedline [50, 223, 56, 66]; in the Schwab-group implementation the transmission through the cavity is measured [68, 252].

Typical lengths of these on-chip resonators are in the millimetre range so that the microwave resonance frequency is a few GHz. The electric quality factor is typically $10^4$; in the experiments, the dissipation is determined by the coupling to the feedline and not by internal losses (i.e., they are overcoupled) [50]. An overview of the key parameters of these devices is given in Table 8. Large optomechanical coupling is obtained for thin, long doubly clamped beams that are positioned as close as possible near the ground plane. A coupling of $g_{OM} = 2\pi \cdot 84\,\mathrm{kHz/nm}$ is reported [68] for a 170

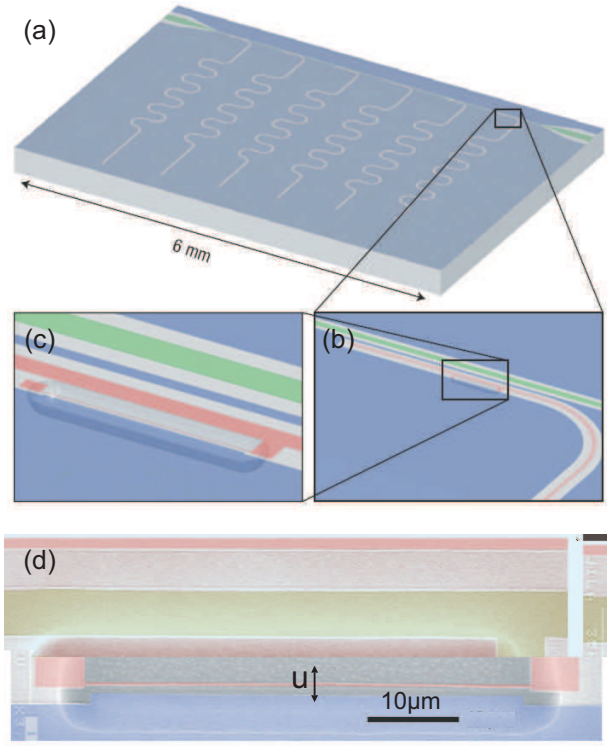


Figure 28: Illustration of the stripline resonators used by Regal *et al.* (a) Chip with 6 meandering stripline resonators (pink) and the straight feedline (green). The $\lambda/4$ resonators have a slightly different length, which allows for frequency multiplexing. (b) The resonators are coupled to the feedline by a capacitive elbow coupler. (c) and (d) zooms of the resonator. The 50 $\mu$m long aluminum beam resonator is under tensile stress which is induced by annealing at an elevated temperature. A movement of the beam changes the capacitance of the stripline to the ground plane (blue) and thereby the cavity resonance frequency. Reprinted by permission from Macmillan Publishers Ltd: Nature Physics 4, 555–560, copyright 2008.

nm wide and 140 nm thick beam, that is formed from 60 nm of stoichiometric, high-stress silicon nitride and 80 nm of aluminum. The resonator is located 75 nm from the gate electrode. Further substantial improvements in the coupling strength are difficult with this particular geometry and fabrication technology. Sulkko *et al.* [253] used a focussed ion beam to create a very small gap of about 10 nm between a mechanical resonator and a resonant microwave circuit and obtained $g_{OM} = 2\pi \cdot 1\,\mathrm{MHz/nm}$, thus increasing the coupling considerably (see Table 8).

An important difference with optical cavities is that there are no single photon detectors available for microwave frequencies. In optical systems these do exist, and the detection of the light in itself is quantum-limited. Present commercial microwave amplifiers, however, always add substantially more noise than required by quantum mechanics since they are not shot-noise limited. This problem can largely be overcome by using a Josephson parametric amplifier. Teufel *et al.* [66] have made a nearly shot-noise-limited microwave interferometer and demonstrated nanomechanical motion detection with an imprecision below the standard quantum limit. On the other hand, similar to their optical equivalents, the photon-pressure backaction of the stripline position-detectors on the mechanical resonator has been observed [56] and even backaction-evading measurements have been reported [252]. In the latter experiment, a single-quadrature measurement of motion with a sensitivity of four times the zero-point motion has been demonstrated. Sideband cooling has been performed in a series of experiments [56, 68, 252]. Very recently Teufel *et al.* were the first ones to demonstrate ground state cooling using a superconducting LC resonator [23], in which a movable membrane both acts as the capacitor of the LC circuit and as the mechanical oscillator ("drum resonator" geometry). They obtained a thermal occupation of $\overline{n} = 0.34$, where the drum resonator is in the ground state for 57% of the time. In the same type of device they also observed strong coupling between the mechanical resonator and the LC resonator [254].

It should be noted that mechanical resonators have also been coupled to non-superconducting resonant circuits [44, 277]. Sideband cooling from room temperature to 45 K and 100 K respectively has been demonstrated in these systems. The first method differs from the abovementioned superconducting cavities in that it consists of a stripline resonator with lower frequency (100 MHz) and lower quality factor (234). In the second experiment, the resonator is an open-ended coaxial cable with a resonance frequency of 11 GHz and a $Q$ of 80.

### *4.2. Transmission modulation based detection methods*

Mechanical motion can also be detected by measuring the transmission of electrons or photons through devices which embed a movable part. The motion of the mechanical resonator modulates the electron or photon transmission and the

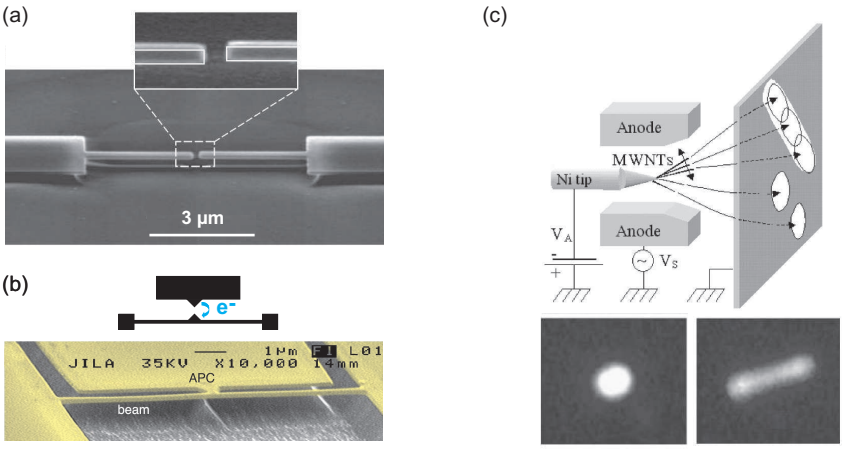


Figure 29: (a) Readout using the light transmitted from one waveguide (left) to another one (right). When one of the cantilevers moves, the transmission of the light changes. This is a non-interferometric optical method to detect mechanical motion. Reprinted by permission from Macmillan Publishers Ltd: Nature Nanotechnology 4, 377–382, copyright 2009. (b) An atomic-point-contact displacement detector. A tunnel contact between the beam and a nearby electrode is made using electromigration. When the Au beam is far from the electrode, the tunneling probability for electrons (see inset) is low and the resistance is high. Closer to the electrode, the transmission increases and the resistance is lower. Reprinted figure with permission from N. E. Flowers-Jacobs, D. R. Schmidt, K. W. Lehnert, Intrinsic noise properties of atomic point contact displacement detectors, Phys. Rev. Lett. 98 (9) (2007) 096804. Copyright 2007 by the American Physical Society. (c) Setup to measure multi-walled nanotube vibrations via field emission. Electrons are emitted by applying a voltage $V_A = -500$ to $-900$ V between the nanotube and a nearby (3 cm) screen. The electrons hit the screen at a certain position and show up a bright spot. The insets at the bottom show the spots for a silicon-carbide resonator that is driven off-resonance (left) and on resonance (right). In the latter case the spot is blurred due to the motion of the resonator. Adapted from Refs. [278] and [90]. Reprinted with permission from S. T. Purcell *et al.* Tuning of nanotube mechanical resonances by electric field pulling, Phys. Rev. Lett. 89 (27) (2002) 276103. Copyright 2002 by the American Physical Society and S. Perisanu *et al.* Appl. Phys. Lett. 90 (4) (2007) 043113. Copyright 2007, American Institute of Physics.

output signal contains spectral information about the resonator dynamics. Below we will discuss in detail two basic configurations of this detection scheme: optical waveguides and electron tunneling devices, including electron shuttles.

### *4.2.1. Optical waveguides*

As mentioned above, light can be guided on a chip using optical waveguides. These are pieces of transparent material (e.g. Si, $SiO_2$ or SiN) which are carved out of the underlying substrate. Light can propagate through these waveguides and can be directed to any place on the chip. Just outside the waveguide the electromagnetic field is not zero and decays exponentially with the distance from the waveguide. When two waveguides are placed close together, light can be transmitted from one to the other[34]. The transmission between the waveguides depends on the distance between them and they can be employed as a position detector. The method is also compatible with operation in water [280], which is important for (bio)sensor applications, and it has also been used to make optoelectronic switches [281]. Li *et al.* [59] have used the transmission-modulation principle to measure the mechanical motion of cantilever structures made in a silicon-on-insulator platform with high sensitivity. In particular, they placed the suspended ends of two waveguides facing each other at a distance of 200 nm as shown in Fig. 29a. The transmission of photons through the gap depends on the distance and the exact position of the cantilevers (misalignment). The thermal motion of the cantilevers modulates the transmission and the transmitted light is fed into a photodiode. The spectrum clearly reveals multiple resonances of the cantilevers with a sensitivity of 40 fm/ $\sqrt{\text{Hz}}$ at room temperature. An advantage of this method over optical cavities is that the detection scheme allows for transduction of nanomechanical motion over a wide range of optical frequencies, instead of working only at certain well-defined wavelengths.

### *4.2.2. Electron tunneling*

When two metallic electrodes are placed close (up to a few nanometer) to each other, electrons can tunnel through the gap between them. With a voltage applied between both electrodes, a net current flows that depends exponentially on their distance. This exponential distance dependence can be used to measure displacements of mechanical resonators. Flowers-Jacobs *et al.* [42] have measured the displacement of the doubly-clamped gold beam shown in Fig. 29b using an atomic point contact (APC) made by electromigration [282]. Since the tunneling resistance between the APC and the beam is high, a tank circuit is used for impedance matching to 50 Ω high-frequency amplifiers. The Brownian motion of the beam is observed at a temperature of 250 mK with a shot-noise limited imprecision of 2.3 fm/ $\sqrt{\text{Hz}}$. From the

[34] A related, but different method is demonstrated in Ref. [279], where photons are transferred from one waveguide to another, which runs parallel to the former. The coupling between the waveguides depends on the distance between them (i.e., on the displacement) and photons that enter the second waveguide are "lost" and not detected at end of the first waveguide.

temperature dependence of the thermal noise spectra, a backaction temperature of 0.7 K is found, which is larger than expected from the momentum carried by the tunneling electrons. Kan *et al.* used a similar technique where an STM tip was positioned above a MEMS resonator [283]. The current modulation due to the resonator motion was down-mixed (Sec. 4.3.3) to overcome bandwidth limitations. Based on these methods an interesting new type of detector is proposed [284]. By incorporating the movable tunnel junction into a loop threaded by a magnetic flux, the APC can be used to measure the *momentum* instead of the position of the resonator. Also, other more sophisticated schemes are envisioned for detecting entanglement in the mechanical quantum oscillator [285].

Another method is based on field emission of electrons from a vibrating tip. Consider, for instance, a multi-walled carbon nanotube [278] mounted under vacuum in a field emission setup (see Fig. 29c). A large voltage is applied between the carbon nanotube and an observation screen which lights up at the position where electrons are impinging. Electrons are accelerated from the tip of the nanotube to the screen by the electric field. Motion of the nanotube cantilever results in a small blurring of the spot at the screen. The thermal motion of the nanotube already blurs the spot a bit, but when the vibration amplitude is enlarged by applying a RF driving signal on nearby electrodes the blurring of the spot becomes more pronounced on resonance. The electric field also pulls on the nanotube, thereby increasing the resonance frequency [278]. The method has been used to build a nanotube radio [74], a mass sensor with atomic resolution [77], and high $Q$ silicon carbide nanowire resonators at room temperature [90].

In more complicated circuits shuttling of electrons has been considered [286, 125, 287]. These devices operate as follows: there are two electrodes with a movable metallic island in between. When the resonator is closer to one of the electrodes, the transmission between the island and this electrode increases, allowing for electrons to jump on the island. The electrostatic force drives the island with the negatively-charged electrons to the other electrode. This way, they are transported to the other electrode by the resonator (mechanical transport of electrons). In steady state this shuttling occurs at the resonance frequency of the oscillating island. Interestingly, the voltage applied between the two electrodes can amplify this motion and lead to large amplitude oscillations; an example of an electomechanical instability[35]. This subject has been extensively reviewed by Gorelik *et al.* [288] and we refer to this work for further reading.

### *4.3. Capacitive detectors*

In many nano-electromechanical devices, movable metallic parts form capacitances with nearby metallic electrodes or ground planes. Displacement of the mechanical structure inevitable leads to a change in these capacitances which can be detected electrically if they are large enough. Likewise, the motion of the mechanical resonator can be actuated by applying voltages between the different electrodes as we have discussed in Sec. 2.4.4. This capacitive actuation and read-out of mechanical motion has been applied in several ways. Here, we will discuss three popular methods.

#### *4.3.1. Single-electron transistors*

One of the first mesoscopic devices that was used for position detection was the single-electron transistor (SET) [29]. This device consists of a metallic island that is connected by tunnel contacts to a source and drain electrode. The total capacitance of the island is so small that the energy required to add one electron surpasses the thermal energy [289] and electrons can only enter and leave the island one by one (sequential tunneling). The resulting single-electron current through the island is very sensitive to the electrostatic environment. Thus, if a nearby resonator is capacitively coupled to the island, and it has a different electrostatic potential, the device can be used as a displacement sensor, as illustrated in Fig. 30. The first realization of such a device was made by Knobel and Cleland [29], where the SET measured the position of a 116 MHz beam resonator with a sensitivity of 2 fm/ $\sqrt{\text{Hz}}$. This value corresponds to a position resolution a factor of 100 above the standard quantum limit, as is indicated in Table 7. The SET was operated as a mixer, a technique that we will discuss in more detail in Sec. 4.3.3. Subsequent work by LaHaye *et al.* [30] demonstrated, using a superconducting radio-frequency SET, a sensitivity of four times the standard quantum limit. The role of the RF SET is to provide impedance matching for the high-frequency resonator signal (19.7 MHz).

Using an improved version of this device (Fig. 30b), Naik *et al.* [32] observed the backaction of the superconducting SET on the mechanical resonator; a change in the capacitance leads to a change in the average charge ("occupation") [290], which in turn leads to a change in the electrostatic force the resonator experiences. Depending on the bias conditions (gate voltage) of the SET, shifts in the resonance frequency and the damping rate were observed. Thus the backaction force on the detector, characterized by the function $\lambda_F$ that was introduced in Sec. 3.4.1, is bias dependent for this type of detector [240, 212, 291, 292]. The effective resonator temperature has been measured for different coupling strengths between the resonator and the SET. In the experiment this is done by varying the voltage difference between the resonator and the SET. For small couplings, the resonator temperature equals that of the sample chip i.e., close to

[35] This shuttling instability can thus be viewed as an example of backaction induced self-oscillations as discussed in the previous Section. When pursuing the quantum limit in these devices, people refer to the ability to transport exactly one charge carrier per cycle from source to drain; the zero-point motion does not play a crucial role in achieving this.

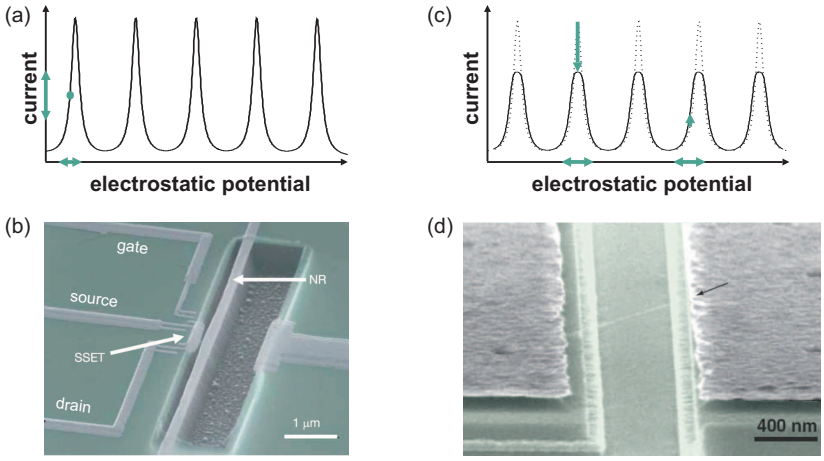


Figure 30: (a) Illustration of the dependence of the current through a SET on the electrostatic potential. The current is almost zero in the Coulomb blockade regime and displays so-called Coulomb peaks where the blockade is absent. The resonator motion modulates the potential (horizontal arrow) and this leads to a proportional change in the current. (b) The device used in the Schwab group. The superconducting single-electron transistor (SSET) is made from aluminum and is connected to a source and drain electrode. The potential of the SET can be varied using a gate electrode and is also influenced by the position of the beam resonator. From M. D. LaHaye *et al.*, Science 304 (2004) 74–77. Reprinted with permission from AAAS. (c) Illustration of self-detection via rectification. Motion of the resonator leads to a decrease in the *average* current on top of the Coulomb peak, whereas deep in the blockade region it leads to a (small) increase. (d) SEM picture of a ultra-high quality factor nanotube resonator. From G. A. Steele *et al.*, Science 325 (2009) 1103–1107. Reprinted with permission from AAAS.

the base temperature of the dilution refrigerator. For higher couplings, the resonator temperature is set by the backaction temperature of the SET, and is raised to about 200 mK.

It should also be possible to use a SET to sense the vibrations of a suspended carbon nanotube, but the small capacitive coupling between the nanotube and the SET island makes this a challenging task [293]. It is more advantageous to use the suspended carbon nanotube *itself* as a self-detecting SET. Using current rectification and frequency mixing, information about the driven motion of the suspended nanotube has been obtained [81, 82, 106]. In these experiments, a strong coupling between mechanical motion and the charge on the nanotube has been observed. The strong coupling is due to the electrostatic force generated by individual electrons tunneling onto the nanotube. For the devices used in these experiments, the change in equilibrium position of the nanotube after adding a single electron easily surpasses the zero-point motion. Typically, the single-electron tunnel rate is much larger than the resonance frequency, indicating that the backaction is determined by the average number of electrons ("occupation") on the nanotube. This backaction leads to frequency shifts and changes in damping as a function of gate voltage. To be more specific, the damping increases dramatically with the amount of current flowing through as the electron tunneling produces a large stochastic backaction force.

In Refs. [81, 106] readout using current rectification[36] is employed. While the nanotube motion is actuated by a RF signal on a nearby antenna, the detected signal is at DC. The key to understand this is the notion that nanotube motion effectively translates into an oscillating gate voltage, which smears out the sharp features of the SET current, as illustrated in Fig. 30c [295]. The technique is of special interest as it constitutes a square-law detector (see Appendix C). Moreover, it allows for the motion detection with small currents, enabling the observation of ultra high Q-factors, exceeding 100,000 at millikelvin temperatures. The low dissipation enables the observation of *single-electron tuning* and frequency tuning oscillations, analogous to the Coulomb oscillations in the SET current. Recently, this self-detecting rectification scheme has also been employed for a thin aluminum beam [296].

### *4.3.2. Quantum-point contacts*

A quantum-point contact (QPC) is a narrow constriction in a two-dimensional electron gas, whose conductance can be adjusted using electrostatic potentials [297]: Every time another channel for electrons becomes available, the conductance increases by one conductance quantum $2e^2/h$. In practice these sharp steps are smoothed by temperature and when the QPC is biased near such a step it is very sensitive to changes in the electrostatic potential. If mechanical vibrations modulate the electrostatic fields, the QPC can also be used as a position detector. Cleland *et al.* have used this principle to

[36] The rectification and mixing measuring method have in common that they both rely on the nonlinearity of the current-voltage or current-gate-voltage characteristics [294]; the experimental implementation is, however, different. It should also be noted that rectification is more commonly used to detect displacement in mechanical resonators. For example, in the experiments of Ref. [74, 77] (Sec. 4.2) the dc tunnel current contains information about the vibrating carbon nanotubes since a time-dependent displacement changes the source-drain distance and thereby the averaged current.

measure the vibrations of a beam made out of a single-crystal GaAs heterostructure with a sensitivity of 3 pm/ $\sqrt{\text{Hz}}$ [298]. In this case the QPC is part of the beam and frequency mixing (Sec. 4.3.3) is used to detect the displacement through the voltage across the QPC. The signal is amplified through the piezoelectric effect in GaAs that will be discussed in more detail in Sec. 4.4.

A similar sensitivity has been achieved in a completely different setup by Poggio and coworkers [52]. Now a 5 kHz micromechanical resonator is hanging above a QPC that is located on a different substrate. Thermal noise specta have been recorded and the authors have mapped out the transduction factor as a function of cantilever position relative to the QPC. Furthermore, they observe that the cantilever Q-factor is not affected by the QPC source-drain current, indicating weak coupling and therefore negligible backaction.

A QPC can also be used to probe vibrational modes of the host crystal itself [299]. This substrate is a truly three-dimensional resonator that consists of on the order of $10^{20}$ atoms. Strictly speaking, the latter example does not constitute of a capacitive detector as the transduction is through the piezoelectric effect; the motion directly influences the source-drain voltage and not the conductance of the QPC.

*4.3.3. Frequency mixing*

Frequency mixing has been adopted in top-down solid-state devices as a versatile technique to convert high-frequency motion into a low-frequency signal [298, 29, 300]. It is most often used in combination with capacitive detection techniques, although it is also used in combination with electron tunneling (Sec. 4.2) and piezoelectric resonators (Sec. 4.4). The basic principle is as follows. Consider the generic relation between the input (i.e., the displacement $u$) and the detector output $v$ introduced in Sec. 3: $v(\omega) = \lambda_v(\omega)u(\omega)$. By modulating the transduction $\lambda_v$ at a frequency $f_{LO}$ (often called the local oscillator frequency), the displacement at frequency $f_R$ is converted into a signal with frequencies $f_R + f_{LO}$ and $f_R - f_{LO}$. The latter component at the difference frequency can be chosen to be at a frequency far below the resonator frequency: for example in the kHz range. The signal at this frequency is not affected by the RC time of the measurement setup and can therefore be measured straightforwardly.

The technique has become of particular interest for detecting vibrational motion of bottom-up devices. Sazonova *et al.* [73] were the first to apply frequency mixing to suspended carbon nanotube resonators. They observed multiple gate-tunable resonances with Q-factors on the order of 100 at room temperature. Subsequently Witkamp *et al.* [20] identified the bending mode vibrations of a carbon nanotube. Nowadays the technique has been employed by many groups, not only restricted to carbon nanotubes [76, 78, 126, 82, 83, 85], but also applied to suspended graphene sheets [103, 104], free-hanging semiconducting nanowires [94, 96] and charge-density-wave sheets [105]. Furthermore, several variations to the original mixing scheme have been implemented, including FM [85] and AM modulation [126].

A more detailed understanding of this self-detecting method can be obtained by considering, for example, the suspended carbon nanotube of Fig. 10. The conductance of a semiconducting nanotube depends on the induced charge, which is the product of the gate voltage and the gate capacitance, i.e. $G = G(C_g V_g)$. As we have shown before, the gate capacitance is position dependent and therefore the conductance varies in time with the resonator frequency. In nanotube mixing experiments, the current is measured, which is the product of the conductance and the bias voltage: $I = V_b\, \partial G/\partial u \cdot u$, from which we identify $\lambda_v = V_b\, \partial G/\partial u$. The modulation of the transduction can thus be done by applying an ac bias voltage: $V_b = V_{ac}\cos(\omega_{LO} t)$, as explained in Fig. 31. In these experiments backaction comes again from the electrons flowing through the nanotube [82].

*4.4. Piezoelectric resonators*

A different mechanism to transduce a displacement into an electrical signal uses piezoelectricity. In a piezoelectric material a stress induces an electric polarization, or equivalently, an electric displacement $\mathcal{D}$ [137]. This results in a voltage difference across the resonator that can be used to infer the displacement. Piezoelectric resonators are different from most other methods discussed in this Section as no separate detectors are needed; they detect their own motion instead. Moveover, they are also different from the other self-detecting resonators (e.g. the suspended carbon nanotubes and graphene resonators that were described above) since no external signal needs to be applied in order to measure the displacement (for example, in the nanotube experiments of Sections 4.3.1 and 4.3.3 one has to apply a source-drain voltage to transduce the displacement). Still, from the discussion in Sec. 3.4 it is clear that backaction forces should also act on a piezoelectric resonators when measuring the generated voltage. This happens through the converse piezoelectric effect, where an electric field generates a strain in the material. Referring back to the definition of stress and strain in Sec. 2, the direct and converse piezoelectric effect are [137]:

$$\mathcal{D}_i = d_{ijk}\sigma_{jk}, \qquad \gamma_{ij} = d_{ijk}\mathcal{E}_k. \tag{71}$$

Here $\mathbf{d}$ is the third-rank tensor with the piezoelectric coefficients. Similar to the properties of the elasticity tensor, many of the elements $d_{ijk}$ are zero, or related to other elements, depending on the symmetries of the crystal structure of the material. A necessary requirement to have at least one nonzero element is that the material's unit cell does not have an

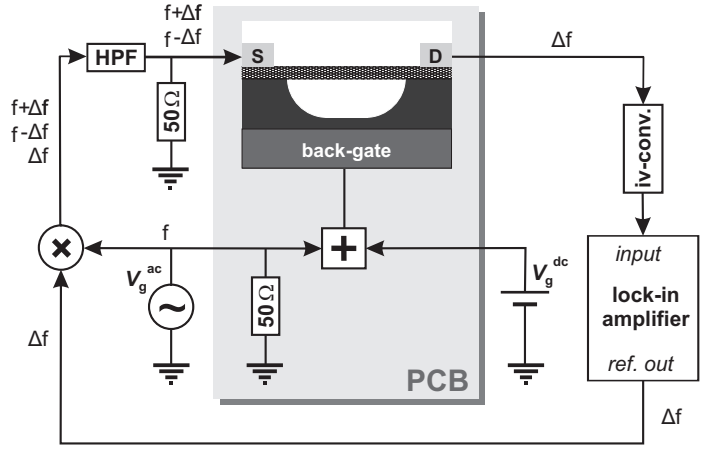


Figure 31: Schematic overview of the measurement electronics used by Witkamp *et al.* for position detection of a suspended nanotube using frequency mixing [20]. A radio frequency (RF) generator applies an ac voltage to the back-gate electrode to drive the suspended nanotube. A dc gate voltage is added via a bias-T (indicated by the "+"). The same generator is used to generate the ac bias voltage by mixing its output with the reference output of the lock-in amplifier. At the source electrode the voltage has spectral components at $f + \Delta f$ and $f - \Delta f$, whereas the gate voltage is oscillating at frequency $f$. The nanotube mixes both signals, which results in an output current at the drain electrode with spectral components at $\Delta f$, $f + \Delta f$, $f - \Delta f$, $2f + \Delta f$ and $2f - \Delta f$. The $\Delta f$ part of the current flowing through the nanotube is converted into a voltage and is measured with a lock-in amplifier. The printed circuit board (PCB) with the sample, bias-T and 50Ω terminator is located inside the vacuum chamber of a probe station.

inversion center. For most piezoelectric materials, including GaAs and AlN, the piezoelectric coefficients are of the order of pC/N and they can have both positive and negative values.

Piezoelectric displacement detection of small structures has first been employed with AFM cantilevers [301, 302, 303], before extending the technique to the nanomechanical domain. Tang *et al.* used this detection scheme[37] to detect the motion of GaAs/AlGaAs beams [304]. The beams are made asymmetric to ensure that the piezoelectric signal is not nulled by the opposite stresses at both sides of the neutral plane (Sec. 2.3). Cleland *et al.* used piezoelectricity to detect the motion of GaAs beams with an integrated QPC in it. There, a deflection of the beam induces in-plane stress and the resulting out-of-plain field $\mathcal{D}$ acts as an effective gate voltage. This then changes the current through the QPC [298]. An important consideration is that piezoelectric materials cannot generate large currents. The resonator should therefore be connected to a high-impedance load, such as the gate electrode of the QPC [298], to the gate of a SET [305], or a high-impedance amplifier [304].

Mahboob and Yamaguchi used the two-dimensional electron gas in a flexural beam resonator made of a GaAs/AlGaAs heterostructure to measure the displacement and they demonstrated parametric amplification by modulating the beam's resonance frequency using the converse piezo-electric effect [306]. The converse piezo-electric effect was also used to tune the frequency of a doubly-clamped zinc-oxide nanowire by Zhu and coworkers [94]. Okamoto *et al.* found an enhancement of backaction effects due to excitation of carriers in an piezoelectric GaAs resonator [307]. Many of the abovementioned effects were combined by Masmanidis and coworkers who used a three-layer structure, consisting of p-doped, intrinsically doped, and n-doped GaAs to demonstrate piezoelectric actuation, frequency tuning, and nanomechanical bit operations [308]. By electrically shifting the carriers with respect to the neutral plane, the strength of the actuation could be adjusted. Finally, by capacitively coupling a bulk AlN resonator to a qubit, O'Connell *et al.* obtained the high coupling rates required to perform quantum operations on a mechanical resonator [22]. This experiment was already mentioned in the Introduction and will be discussed in more detail in Sec. 5.2.

### *4.5. Flux-based position detectors*

#### *4.5.1. SQUIDs*

Superconducting quantum interference devices (SQUIDs) are well known for detecting small magnetic signals, such as those generated by our brains. These devices consist of a superconducting ring in which one or more Josephson junctions are incorporated [309]. The voltage across the loop depends on the amount of magnetic flux that threads the loop, $\Phi_{mag}$. This flux-dependence[38] has been employed to sense the motion of a cantilever with a small magnetic particle attached to it [310].

It is, however, also possible to detect displacements by *incorporating* a mechanical resonator in the SQUID loop [311, 312, 313, 314, 315, 316, 317, 186, 318, 319, 320]: In the presence of a constant magnetic field, a change in the

[37] In this experiment the measured signal contained both piezoelectric and piezoresistive components.

[38] SQUIDs are also used indirectly for position detection, where the SQUID is used as low-noise voltage amplifier that amplifies the signal generated by capacitive detection [53]. In this section, we only focus on direct position detection with SQUIDs.

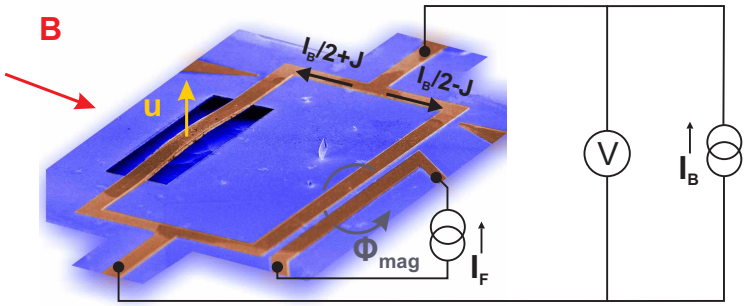


Figure 32: Schematic overview of a dc SQUID position detector, including the suspended beam resonator and measurement setup. The SQUID loop is indicated in brown. The output voltage of the SQUID depends on the bias current $I_B$ that is sent through the SQUID and also on the amount of flux $\Phi_{mag}$ through the loop. A magnetic field $B$ transduces a beam displacement $u$ into a change in magnetic flux and subsequently in a change in the output voltage $V$. The flux $\Phi_{mag}$ is fine-tuned with a stripline current $I_F$. Backaction results from the circulating current in the SQUID loop $J$. Reprinted figure with permission from M. Poot *et al.*, Phys. Rev. Lett. 105 (2010) 207203. Copyright 2010 by the American Physical Society.

resonator displacement changes the loop area and thereby the flux through the loop. This is illustrated in Fig. 32. Recently, Etaki *et al.* have used a dc SQUID as a sensitive detector of the position of an integrated mechanical resonator. They detected the driven and thermal motion of a 2-MHz buckled-beam resonator with femtometre resolution at millikelvin temperatures [19] and employed active feedback cooling to cool the resonator to 20 mK [70]. In the present experiments, the sensitivity is limited by the cryogenic amplifier and not yet by the, in principle quantum limited SQUID itself.

Backaction has also been observed, leading to tunable shifts in the resonance frequency and damping of the resonator [242]. Different from the backaction in the capacitive readout schemes, the backaction of the SQUID has an inductive character as it is caused by the Lorentz force generated by the current circulating in the loop of the SQUID. This current also runs through the resonator (Fig. 32) and the magnetic field that couples displacement and flux, generates a Lorentz force on the resonator.

### *4.5.2. Magnetomotive*

A fast and relatively easy way to actuate and read-out nanomechanical motion in clamped-clamped resonators is the magnetomotive technique [321, 322, 28, 194]. Nowadays, this method is mainly used to determine the vibrational frequencies and to characterize dynamic properties such as the Q-factor and nonlinear behavior. It is, however, of limited use for QEMS experiments and we will therefore only briefly describe the mechanism: An ac current $I_{ac}$ is sent through the conducting (part of the) beam which is placed in a strong static magnetic field. The ac current causes an ac Lorentz force that drives the beam $\mu_n B\ell I_{ac}$. At the same time, motion of the beam induces a time-varying voltage (Faraday's law) at the driving frequency $V_{emf} = \mu_n B\ell\dot{u}$. By sweeping the driving frequency, the resonance can be found by measuring the frequency response of the voltage over the beam. The required large magnetic field is typically generated using superconducting magnets in a cryogenic environment, but recently room temperature magnetomotive actuation and detection has been demonstrated with a 2 T permanent magnet [323]. An important feature of this technique is that observed mechanical modes can be distinguished from electronic resonances by varying the magnetic field. Since both the driving force and the detector signal are proportional to $B$, the mechanical signal scales as $B^2$ [324].

## *4.6. Level spectroscopy in suspended quantum dots*

At low temperatures, suspended quantum dots may reveal information about their vibrational states: in the parameter regime dominated by Coulomb blockade physics, the quantum mechanical level spectrum of the confined electronic system can be characterized by transport measurements. The levels show up as steps in the current-voltage characteristics. A more accurate measurement involves the recording of a so-called stability diagram in which the differential conductance dI/dV plotted as function of gate voltage $V_G$ and source-drain voltage $V$. Now the excitations (due to electronic or vibrational degrees of freedom) show up as lines, whose energy can directly be read out [325] as illustrated in Fig. 33. In the case of vibrational states these are also called vibrational side bands and when the harmonics of a particular vibration are excited, the lines form a spectrum with equidistant spacing. Thus, electron tunneling through suspended quantum dots can excite vibrational modes and these modes can then be detected as steps in the current-voltage characteristics. Their observation involves, however, two important considerations: the energy resolution and the electron-vibron coupling. Concerning the energy resolution of transport spectroscopy measurements one must have $\hbar\omega_R > k_B T$ so that measurements are always performed in the quantum limit of the mechanical mode.

Secondly, the electron-vibron coupling must be high enough; it can be characterized by a dimensionless parameter

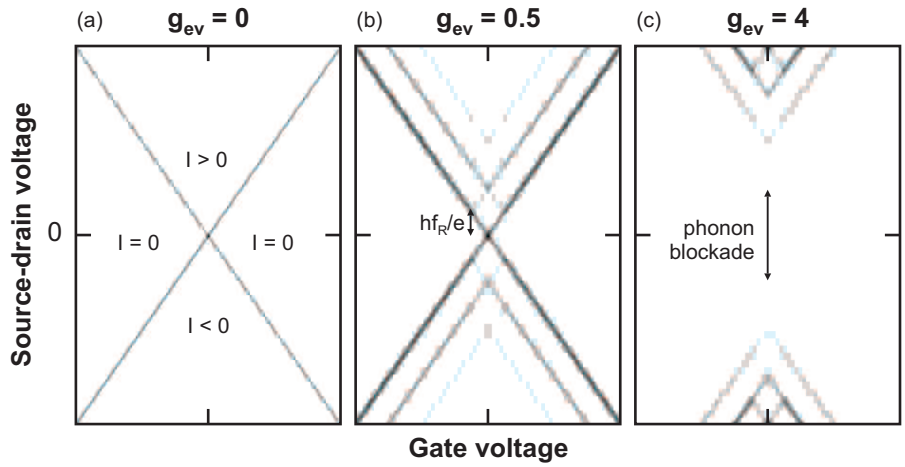


Figure 33: Stability diagrams for zero (a), intermediate (b), and large (c) electron-vibron coupling $g_{ev}$. A stability diagram is a grayscale plot of the differential conductance plotted against the gate and source-drain voltage. Coulomb peaks (Fig. 30) appear here as dark lines, whereas regions with low differential conductance d$I$/d$V$ are white. (a) shows a regular stability diagram without signatures of the mechanical resonator. There are regions where the current is blocked and regions where current flows. These are separated by the high-conductance lines (dark). In (b) a finite electron-vibron coupling is present and mechanical excitations appear as lines parallel to the original lines of high conductance (vibrational sidebands). The source-drain voltage where these lines cross the Coulomb diamond edges, equals $hf_R/e$ as indicated. For large $g_{ev}$ the current is blocked at low source-drain voltage as shown in (c) and vibrational excitations can only been seen at high bias voltage.

$g_{ev} = \frac{1}{2}(\Delta u/u_0)^2$, where $\Delta u$ is the shift of the resonator position[39] induced by adding one elementary charge, and $u_0$ is the zero point motion of the mechanical oscillator [326]. The parameter $g_{ev}$ determines the step height in the current-voltage characteristic. We can consider three regimes in describing the influence of vibrational modes on transport: the weak electron-vibron coupling regime with $g_{ev} \ll 1$, the intermediate regime with $0.1 < g_{ev} < 1$ and the strong coupling ($g_{ev} \gg 1$) limit. The boundaries of the intermediate regime are, however, somewhat arbitrary. Figure 33 shows calculated stability diagrams for three different values of the electron-vibron coupling. In the weak coupling regime (see panel (a)) only the regular Coulomb step is present (no side bands are visible) and consequently vibrational modes cannot be detected in a transport experiment. Only for sufficiently large electron-vibron coupling, one or multiple so-called Franck-Condon steps can be observed in the current, which show up as lines in the stability diagram (the intermediate regime, panel (b)). This was first demonstrated in molecular junctions exciting $C_{60}$ radial breathing modes [327], and later in suspended carbon nanotubes probing the radial breathing mode [328], or the longitudinal, stretching modes [329]. In the strong electron-vibron coupling limit, the vibrational induced excitations are only seen for larger bias voltages as the height of the first steps is exponentially suppressed. In panel (c) this is clearly visible: the grey lines representing the vibrational excitations are only present for high source-drain voltages. Importantly, the suppression holds for any gate voltage and as a result the current at low bias is suppressed in the whole gate range [330, 331]. Degeneracy points in the Coulomb diamonds are no longer visible in the stability diagrams and one speaks of phonon blockade of transport. Phonon blockade has been observed in suspended quantum dots embedded in a freestanding GaAs/AlGaAs membrane [332] and subsequently in suspended carbon nanotube quantum dots [333].

Recently, is has been shown that inelastic electron tunneling spectroscopy (IETS) can also be used to gain information about vibrational modes in suspended quantum dots. Hüttel *et al.* [334] observed a harmonic excitation spectrum connected to the longitudinal stretching modes of a suspended carbon nanotube in the Coulomb-blockaded regime, while temperature only allows the observation of a single excitation. The non-equilibrium occupation of the modes is explained by the pumping via electronic states, revealing a subtle interplay between electronic and vibrational degrees of freedom.

[39] Actually, this is the shift in the location of the minimum of the potential energy of the resonator. The tunneling of the electron is assumed to take place on a timescale that is much faster than the resonator can react.

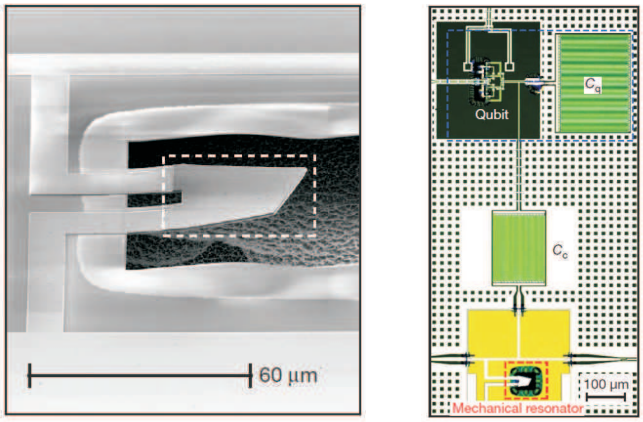


Figure 34: A mechanical resonator coupled to a Josephson qubit. The mechanical resonator (left) is cooled cryogenically to its ground state and manipulation of its quantum state at the single phonon level has been demonstrated. The quantum properties of the resonator are probed by the superconducting qubit which is positioned on the top side of the right panel. Reprinted by permission from Macmillan Publishers Ltd: Nature 464, 697–703, copyright 2010.

## 5. Prospects

So far, we have mainly concentrated on the limits of (linear) displacement detection. As discussed before, there are other ways of demonstrating quantum behavior. For example, square-law detection would directly probe the energy eigenstates of the mechanical resonator (Sec. 3 and App. C). Another approach is to couple a mechanical quantum oscillator to another quantum system such as the well-studied Josephson qubit [335]: the state of the mechanical resonator changes the state of the qubit, which can then be probed to provide information about the mechanical states. A general problem in such schemes is that the coupling needs to be sufficiently strong so that the exchange of quantum states occurs before decoherence sets in. In April 2010, the first experimental realization of a coupled quantum system involving a mechanical resonator (see Fig. 34) has been reported by the groups of A. Cleland and J. Martinis [22]. They demonstrated the superposition and coherent control of the quantum states of a mechanical resonator. The key aspect of their experiment is the use of a piezoelectric material for the resonator which boosts the coupling; it would be extremely hard to reach similar coupling strengths by using electrostatic forces alone (see also Table 8). We will briefly come back to this ground breaking experiment in the second part of this Section when discussing coupling mechanical systems to other quantum systems from a more general point of view (see Sec. 5.2).

Also concerning the linear detection schemes many challenges lie ahead. Strong coupling, ground-state preparation and detection imprecision below the quantum limit have all been reached now. These achievements set the stage for further studies on controlling and detecting non-classical states of mechanical motion; eventually one would like to have a mechanical resonator in its ground state which is strongly coupled to a single photon so that quantum state of single phonons and photons can be exchanged. Large coupling strengths and high Q-factors are necessary ingredients for reaching this goal. It is not a priori clear which detector scheme will be the best suited. The optical and superconducting cavities have the advantage that the underlying concepts are well known and have studied in detail; for detection schemes based on other (mesoscopic) devices (e.g. superconducting SQUIDs, carbon-based resonators) the understanding is clearly not at the same level. For example, the backaction mechanisms in these cases are not understood in all details as these coupled detector-resonator systems cannot be mapped directly onto the Hamiltonian describing cavity dynamics (Eq. 70). More theoretical and experimental research is needed to elucidate on the underlying mechanisms and physics. In the next subsection, we will briefly discuss some of the issues and challenges of linear detectors in more detail.

### *5.1. NEMS as quantum-limited sensitive detectors*

It is clear that in the coming years more efficient read-out and cooling techniques will be employed. For optical systems challenges lie in increasing the coupling strength and to construct optical setups that can be incorporated in dilution refrigerators. In that respect, the recently developed on-chip optic experiments are promising. In the gravitational wave community the next generation of LIGO will use squeezed states to further improve the displacement sensitivity [336]. For the electronic systems, reduction of detector noise is a major issue which can be achieved by the implementation of quantum-limited amplifiers (SQUIDs [337, 338], point contacts [206, 339, 340] or Josephson parametric amplifiers [341, 66]). Furthermore, nonlinear (quantum) effects (see e.g. Refs. [342, 343, 344]) have so far received less attention and this may become an interesting research line.

For cooling experiments high signal-to-noise ratios are important as well as high Q-factors. Since Q-factors are limited by material properties, mechanical oscillators of new materials (preferably in a crystalline form) will have to be fabricated

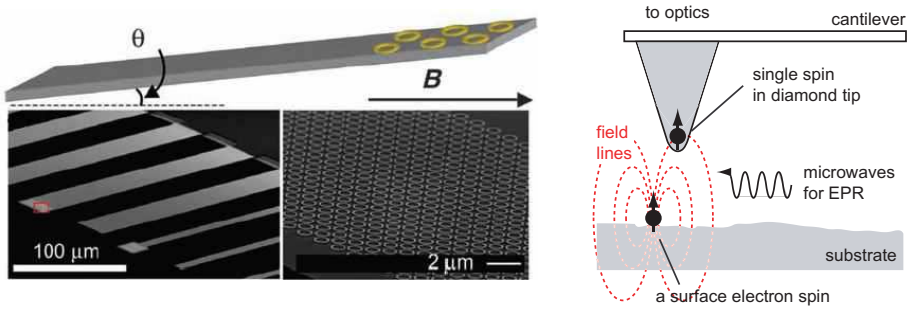


Figure 35: Left: a cantilever resonator containing normal metal rings to study persistent currents. In a magnetic field, the currents produce a torque on the cantilever which shifts the cantilever frequency. By measuring the resonance frequency, the persistent currents could be studied with unprecedented sensitivity. From A. C. Bleszynski-Jayich *et al.*, Science 326 (2009) 272–275. Reprinted with permission from AAAS. Right: Schematic representation of the diamond-based scanning spin microscope proposed in Refs. [345, 346, 347]. The single spin of a NV defect in a diamond tip is a sensitive magnetometer for the local magnetic field with nanoscale spatial resolution. Magnetic fields near the surface shift the electron spin resonance (EPR) frequency of the NV center, which can for example be detected by exciting the EPR transition with a microwave field and monitoring the change in photoluminescence of the probe spin. Reprinted with permission from C. L. Degen, Appl. Phys. Lett. 92 (24) (2008) 243111. Copyright 2008, American Institute of Physics.

and characterized. We should add here that the understanding of the mechanisms controlling dissipation in mechanical resonators is also still open. For example, the role of tension in elevating the Q-factor is not completely understood. The temperature dependence of the Q-factor is another open-standing problem; in some cases a very strong dependence is observed, while in other cases the dependence is weak. What limits dissipation and what is the role of microscopic defect such as two-level fluctuators [16, 71, 72]? Furthermore, for low-mass resonators new effects may start to play a role such as the influence of adsorbents on the resonator surface and nonlinear damping terms associated with the induced tension introduced in Sec. 2.4.4.

The push for refining detection schemes will undoubtedly lead to the construction of better sensors, which eventually will be quantum-limited. These will lead to new applications aimed at both solving fundamental science questions as well as the development of commercial products. An example of the former direction is the recent detection of persistent currents in metal rings fabricated on nanoscale cantilevers [348], illustrated in Fig. 35a. The precision is one order of magnitude better than previous experiments on persistent currents, which are mainly based on SQUIDs. It is also expected that the newly developed optics techniques (i.e., on-chip optics) will find their way in novel applications in controlling, stopping and storing light [349, 350]. Another promising example is the detection of single spins using magnetic resonance force microscopy analogous to the magnetic resonance imaging. Single electron spins have already been detected [351]; the next step is the detection of nuclear spins which requires a thousand fold increase in the sensitivity. An interesting recent proposal (Fig. 35b) is the use of NV centers so that operation at room temperature becomes feasible [347]. If successful, this would yield a revolution in imaging: Many chemical elements carry a nuclear magnetic moment, so that a sensitive enough detector can determine their identity and arrangement in more complex molecules. Finally, NEMS may find an application in mass sensing [352, 353, 78, 77, 76, 354, 97, 355]: the state-of-the art is that single gold atoms can be measured (see Sec. 4). The goal is to be able to detect masses with resolution better than 1 Dalton (the mass of a hydrogen atom) so that each element can be identified making it a mass spectrometer [356].

### *5.2. Hybrid quantum mechanical systems*

In most of this review we have treated optical systems with movable parts as stand-alone systems. Interesting new quantum systems can be built when coupling optical set-ups to other quantum systems such as an ensemble of atoms in a Bose-Einstein condensate. The coupled system would form a hybrid quantum system in which hybrid strong coupling would enable the creation of atom-oscillator entanglement and quantum state transfer. A theoretical proposal appeared in 2007 [357] and in 2008 the interaction between a Bose-Einstein condensate and the optical field in cavity was studied experimentally [358] demonstrating strong backaction dynamics. Subsequent theoretical work showed that strong coupling between a mechanical resonator and a single atom should be feasible [359]. Strong coupling with a single atom has indeed been observed in the blue-detuned cavity regime: Experiments with a single, trapped $Mg^+$ ion interacting with two laser beams showed the stimulated emission of centre-of-mass phonons [360]. At high driving, coherent oscillating behavior is observed, which can be viewed as the mechanical analogue to an optical laser, i.e., a phonon laser. In another approach, the coupling between vibrations of a micromechanical oscillator and the motion of Bose-condensed atoms on a chip are mediated by surface forces experienced by the atoms placed at one micron from the mechanical structure [361]. As illustrated in Fig. 36, the Bose-Einstein condensate probes the vibration of a cantilever. By adjusting the magnetic trapping potential, the discrete eigenmodes of the condensate can be tuned, which in turn tunes the coupling to the cantilever. Systems of many resonators coupled to each other via atoms in an optical lattice are envisioned [362].

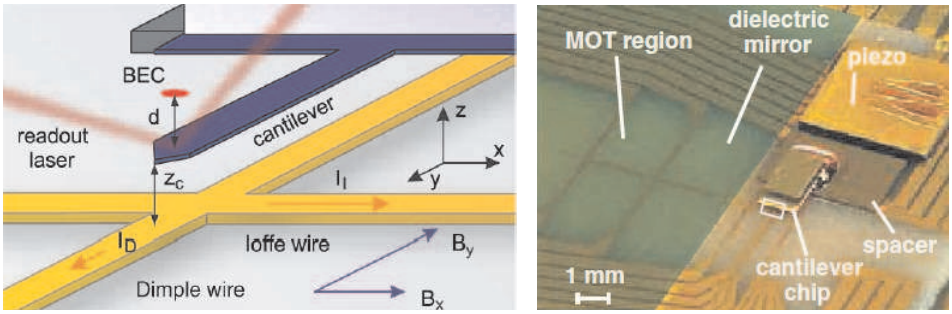


Figure 36: Bose-Einstein condensate (BEC) on an atom-chip couples to a cantilever. The cantilever motion modulates the potential of the atoms, thereby coupling the cantilever position to atomic motion. Left: schematic overview of the setup. The atoms of the BEC detect the cantilever vibrations which can independently measured via the readout laser. Right: photograph of the atom chip. Reprinted figures with permission from D. Hunger *et al.*, Phys. Rev. Lett. 104 (2010) 143002. Copyright 2010 by the American Physical Society

A different approach to create entangled states of mechanical motion by coupling a mechanical quantum oscillator to a solid state device. In the experiment of the group of Cleland and Martinis [22], a Josephson qubit served as a two-level system probing the mechanical states of a 3 ng FBAR resonator (c.f. Fig. 34). With a mechanical frequency of 6 GHz, a mechanical Q-factor of about 100 and a coupling of 62 MHz, there was just enough time to perform a few quantum operations on the mechanical resonator before the quantum state decohered.

If it would be possible to increase the Q-factor while maintaining a strong coupling, quantum mechanical manipulation of long-lived phonon states comes into reach. For example, with a Q-factor of $10^5$ and a frequency of 1 GHz, the mechanical state would survive for 100 $\mu$s before it significantly decoheres. This time is typically much longer than the coherence time of a superconducting qubit, indicating that quantum information can be stored in the mechanical motion and transferred back when needed. The long phonon life times should also be contrasted to the short-lived states in optical cavities: with a frequency of several hundreds of THz and a state-of-the-art optical $Q$ of $10^6$, the photon lifetime is a few ns. Also in this case the mechanical states can be used as storage or delay unit for quantum information if efficient exchange of photons and phonons can be achieved (i.e., strong coupling). From a more general point of view and as a clear direction for the future, one can envision the construction of hybrid systems involving quantum mechanical oscillators that exploit and combine the strengths of the individual quantum systems. The mechanical quantum resonators would then serve as reservoirs of long-lived states with the advantage that they can be well coupled to a variety of other quantum systems.

As a final note, let us return to the crossover between quantum and classical systems as discussed in the Introduction. The quantum experiments of Refs. [22, 23] were performed on mechanical oscillators with a mass of 3 ng and 48 pg respectively. This means that a mechanical object consisting of about $10^{12}$ atoms can still behave quantum mechanically. The crossover has thus not been reached in experiments and continues therefore to be a subject of future studies. Again this aspect shows that the field of mechanical systems in the quantum regime is still largely unexplored: It will still rapidly develop in the years to come bringing many exciting new experiments and discoveries.

## 6. Acknowledgements

We thank Andreas Hüttel and Daniel Schmid for their suggestions about the manuscript. We are indebted to Samir Etaki, Benoit Witkamp, Yaroslav Blanter, Francois Konschelle, Miles Blencowe, Jack Harris, and Hong Tang for the discussions on a wide range of the topics covered in this Report, and for their suggested improvements. This work was supported by FOM, NWO (VICI grant), NanoNed, and the EU FP7 STREP projects QNEMS and RODIN.

## A. Complex Green's function and displacement

One is often interested in knowing the amplitude $A(t)$ and phase $\varphi(t)$ of the displacement when it is written as $u(t) = A(t)\cos(\omega_R t + \varphi(t))$. Since this is only one equation for two functions, the amplitude and phase are not uniquely defined. Consider, for example, the solution $A(t) = u(t)/\cos(\omega_R t)$ and $\varphi(t) = 0$. Already for a pure sine wave $u(t) = sin(\omega_R t)$ this results in a rapidly varying amplitude. The usual notion of the amplitude and phase are that when the signal is close to sinusoidal, the amplitude and phase are that of the sine wave. This can be realized using the complex displacement, which is defined as $u_c(t) \equiv A_c \exp(i\omega_R t)$ with the requirement that $\mathrm{Re}[u_c(t)] = u(t)$. A convenient way of implementing this, is using the complex extension of the resonator Green's function, cf. Eq. 47:

$$u_c(t) = h_c(t) \otimes F(t)/k_R, \qquad h_c(t) = -ie^{i\omega_R t} \cdot e^{-\frac{\omega_R t}{2Q}}\Theta(t), \tag{A.1}$$

so that $\mathrm{Re}[h_c] = h_{HO}$. The amplitude and phase of the resonator displacement are in this case given by the modulus and argument of the complex amplitude: $A(t) = |A_c|$ and $\varphi(t) = \angle A_c$ respectively.

Another notion that is often used in the literature is that of quadratures. Now the displacement is written as $u(t) = U(t)\cos(\omega_R t) + P(t)\sin(\omega_R t)$. Here $U$ is the in-phase component and $P$ is the out-of-phase component (sometimes called quadrature). The quadrature representation is related to the amplitude-and-phase representation by: $U = A\cos\varphi$, $P = A\sin\varphi$, and by $A^2 = U^2 + P^2$, $\tan\varphi = P/U$. The quadratures are also readily calculated using the complex Green's function: $U = \mathrm{Re}[u_c]$ and $P = \mathrm{Im}[u_c]$. Finally, we note that if the displacement is in the in-phase quadrature, i.e. $u(t) = A\cos(\omega_R t)$, then the velocity $\mathrm{d}u/\mathrm{d}t \approx -\omega_R A\sin(\omega_R t)$ is in the out-of-phase quadrature.

## B. Optimal filtering of $v(t)$

In the presence of both position (imprecision) and force noise, one wants to reconstruct the resonator motion in the absence of the detector, $u_i(t) = h_R(t) \otimes F_n(t)$, as good as possible from the measured time trace $v(t)$ of the detector output. This is done by finding the estimator $\hat{u} = g(t) \otimes v(t)$ that minimizes the resolution squared: $\Delta u^2 = \mathbb{E}[(u_i - \hat{u})^2]$. Using the autocorrelation functions and converting these into noise PSDs using the Wiener-Khinchin theorem [200, 207] the resolution is written as:

$$\Delta u^2 = R_{u_i u_i}(0) - 2R_{u_i \hat{u}}(0) + R_{\hat{u}\hat{u}}(0) = \frac{1}{2\pi}\int_{-\infty}^{\infty}\left[S_{u_i u_i}(\omega) - 2G(\omega)S_{u_i v}(\omega) + |G(\omega)|^2 S_{vv}\right]\mathrm{d}\omega. \tag{B.1}$$

Minimizing this w.r.t. $G$, yields the optimal filter $G_{\mathrm{opt}} = S_{vu_i}/S_{vv}$ [200], where:

$$\begin{aligned} S_{vu_i} = S^*_{u_i v} &= AH_R(H'_R)^*\lambda_v^* S_{F_n F_n}, && \text{(B.2)}\\ S_{vv} = S^*_{vv} &= A^2|H'_R|^2|\lambda_v|^2\left(S_{F_n F_n} + A^2 S_{\Phi_{det,n}\Phi_{det,n}}\right) \\ &+ S_{v_n v_n} + 2A^2\mathrm{Re}\left[\lambda_v (H'_R)^* S_{\Phi_{det,n} v_n}\right], && \text{(B.3)} \end{aligned}$$

so that the squared resolution is given by:

$$\Delta u^2 = \frac{1}{2\pi}\int_0^{\infty}\left[\overline{S}_{u_i u_i}(\omega) - |G_{\mathrm{opt}}(\omega)|^2\overline{S}_{vv}\right]\mathrm{d}\omega. \tag{B.4}$$

Depending on the properties of the detector and the coupling $A$, two important limits can be distinguished:

- The detector exerts backaction force noise, but the displacement noise is negligible: $\overline{S}_{v_n v_n} = 0$. In this case the integral in Eq. B.4 is easily solved and one finds:

$$\Delta u_{BA}^2 = \langle u_i^2\rangle \cdot \left(1 + \frac{\overline{S}_{F_n F_n}}{A^2\overline{S}_{\Phi_{det,n}\Phi_{det,n}}}\right)^{-1} = \langle u_i^2\rangle \cdot \left(1 + \frac{\overline{S}_{F_n F_n}}{\overline{S}_{F_{BA,n}F_{BA,n}}}\right)^{-1}. \tag{B.5}$$

  The resolution thus increases (gets worse) with increasing $A$ as the influence of the detector, i.e. the force noise $F_{BA,n}(t)$, on the resonator motion grows. For small values of $A$ this goes as $\Delta u_{BA} \propto A$.

- The detector adds displacement imprecision noise whereas the backaction noise is very small, i.e. $\overline{S}_{\Phi_{det,n}\Phi_{det,n}} = 0$. In this case Eq. B.4 reduces to:

$$\Delta u_n^2 = \langle u_i^2\rangle \cdot J(\mathrm{SNR}, Q), \text{ with } \mathrm{SNR} = \frac{Q^2}{k_R^2}\frac{\overline{S}_{F_n F_n}}{\overline{S}_{u_n u_n}}, \tag{B.6}$$

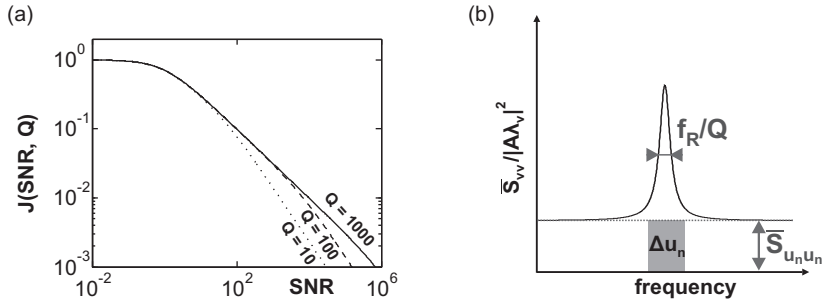


Figure B.37: Plots of the function $J(\mathrm{SNR}, Q)$ for three different values of $Q$. The right side of the plot where $\mathrm{SNR} \gg 1$ corresponds to the situation where the resonator peak is well above the detector noise level and the resolution is good. On the other hand, on the left side (i.e. for $\mathrm{SNR} \ll 1$) the mechanical signal is buried in the imprecision noise and the error is as large as the resonator signal giving $J = 1$. (b) An alternative definition of $\Delta u_n^2$ (cf. Eq. B.7) is the area of the gray rectangle indicated in the noise spectrum.

under the assumption that the detector noise PSD referred to the detector input $\overline{S}_{u_n u_n} = \overline{S}_{v_n v_n}/A^2|\lambda_v|^2$ is white. $J(\mathrm{SNR}, Q)$ is a function (see the plots in Fig. B.37a) that depends on the quality factor and the signal-to-noise ratio, SNR. $J$ tends to 1 when the signal-to-noise ratio is well below unity. In that case, the signal contains so much noise that it hardly contains information about the displacement and using the signal $v(t)$ is not going to give much more information then just assuming that the resonator is at $u = 0$. The average error that is made in the latter case is $\langle u_i^2 \rangle^{1/2}$.

When $\mathrm{SNR} \to \infty$ the function $J(\mathrm{SNR}, Q)$ goes to zero as $Q/(2^{1/2}\,\mathrm{SNR}^{3/4})$. The resolution improves with increasing coupling as the resonator signal is amplified more and more with respect to the noise floor $\overline{S}_{v_n v_n}$.

For practical purposes it is convenient to use a slightly different definition of the resolution [291, 30, 19] that does not involve the signal-to-noise ratio dependent estimator:

$$\Delta u_n^2 \equiv \overline{S}_{u_n u_n} \frac{\pi}{2} \frac{f_R}{Q} = \frac{\langle u_i^2 \rangle}{\mathrm{SNR}}, \tag{B.7}$$

which is readily extracted from the measured noise spectra as indicated in Fig. B.37b. This definition is based on the fact that one can measure the position during a time $\sim Q/f_R$ before the resonator has forgotten its initial amplitude and phase (see also Fig. 15). Note again, that this is the imprecision noise of the detector which does not take the effect of backaction noise into account.

### C. Square-law detection

In a $u$-squared detector the output of the detector depends quadratically on the displacement. In analogy with Eq. 60 the detector output is now $v(t) = A\lambda_v^{(2)}(t) \otimes u(t)^2 + v_n^{(2)}(t)$, where the superscript indicates that this is the response of the square-law detector. A resonator oscillating with frequency $f_R$, results in a detector output with frequency components at $2f_R$ and at dc. As with every detector, the output also contains imprecision noise, $v_n^{(2)}$. Again, by increasing the coupling strength $A$ the signal-to-noise ratio can be improved. In Sec. 3.4 it was shown that for a linear detector this leads to an increased backaction on the resonator, so it is interesting to see if the square-law detector has backaction. The backaction of a detector can vanish when the commutator of the quantity that is measured ($\hat{u}^2 = u_0^2(\hat{a}^\dagger + \hat{a})^2$) at different times is zero [4]. In the Heisenberg representation [2] we have $[\hat{u}^2(t_1), \hat{u}^2(t_2)] = 4iu_0^2 \sin(\omega_R\{t_2 - t_1\}) \cdot (\hat{u}(t_1)\hat{u}(t_2) + \hat{u}(t_2)\hat{u}(t_1)) \neq 0$ for the square detector. Quantum mechanics thus requires that the detector exerts a backaction force noise on the resonator to comply with the uncertainty principle. Also the quantum limit on the resolution for a square detector can in principle be derived using the formalism outlined in Sec. 3.4.

In many implementations, however, the detector has a narrow bandwidth and its output does not contain the signal at frequency $2f_R$, but only the dc component (see e.g. Ref. [81]). The operator corresponding to the $u^2$-detection can be written as $\hat{u}^2 = u_0^2(\hat{a}^2 + \hat{a}^{\dagger 2} + \hat{a}\hat{a}^\dagger + \hat{a}^\dagger\hat{a})$. The first two terms oscillate at twice the resonator frequency and when they are discarded, one finds that this detector detects $\hat{a}\hat{a}^\dagger + \hat{a}^\dagger\hat{a} = 2\hat{n} + 1$. In other words, it detects the number of quanta or the energy in the resonator [269]. Using the fact that $\mathrm{d}\hat{n}/\mathrm{d}t = 0$, one finds that $[n(t_1), n(t_2)] = 0$ and that this detector can be backaction evading [4]. The measurement of the resonator energy will change the phase of resonator, but leaves the energy unaffected [269].

## References


[1] S. Carroll, *Spacetime and Geometry: An Introduction to General Relativity* (Addison Wesley, 2004).
[2] D. J. Griffiths, *Introduction to Quantum Mechanics* (Prentice Hall, 1995).
[3] C. M. Caves, K. S. Thorne, R. W. P. Drever, V. D. Sandberg, and M. Zimmermann, *On the measurement of a weak classical force coupled to a quantum-mechanical oscillator. I. Issues of principle*, Rev. Mod. Phys. **52**, 341 (1980).
[4] V. B. Braginsky, Y. I. Vorontsov, and K. S. Thorne, *Quantum Nondemolition Measurements*, Science **209**, 547 (1980).
[5] S. L. Adler and A. Bassi, *Is Quantum Theory Exact?*, Science **325**, 275 (2009).
[6] J. Dunningham, A. Rau, and K. Burnett, *From Pedigree Cats to Fluffy-Bunnies*, Science **307**, 872 (2005).
[7] I. Katz, R. Lifshitz, A. Retzker, and R. Straub, *Classical to quantum transition of a driven nonlinear nanomechanical resonator*, New J. Phys. **10**, 125023 (20pp) (2008).
[8] A. J. Leggett, *The Quantum Measurement Problem*, Science **307**, 871 (2005).
[9] A. Einstein, B. Podolsky, and N. Rosen, *Can Quantum-Mechanical Description of Physical Reality Be Considered Complete?*, Phys. Rev. **47**, 777 (1935).
[10] W. H. Zurek, *Decoherence, einselection, and the quantum origins of the classical*, Rev. Mod. Phys. **75**, 715 (2003).
[11] S. Bose, K. Jacobs, and P. L. Knight, *Scheme to probe the decoherence of a macroscopic object*, Phys. Rev. A **59**, 3204 (1999).
[12] C. H. van der Wal, A. C. J. ter Haar, F. K. Wilhelm, R. N. Schouten, C. J. P. M. Harmans, T. P. Orlando, S. Lloyd, and J. E. Mooij, *Quantum Superposition of Macroscopic Persistent-Current States*, Science **290**, 773 (2000).
[13] M. Arndt, O. Nairz, J. Vos-Andreae, C. Keller, G. van der Zouw, and A. Zeilinger, *Wave-particle duality of $C_{60}$ molecules*, Nature **401**, 680 (1999).
[14] L. Hackermüller, K. Hornberger, B. Brezger, A. Zeilinger, and M. Arndt, *Decoherence of matter waves by thermal emission of radiation*, Nature **427**, 711 (2004).
[15] A. Cleland, *Foundations of Nanomechanics* (Springer, 2003).
[16] K. L. Ekinci and M. L. Roukes, *Nanoelectromechanical systems*, Rev. Sci. Instrum. **76**, 061101 (pages 12) (2005).
[17] W. Marshall, C. Simon, R. Penrose, and D. Bouwmeester, *Towards Quantum Superpositions of a Mirror*, Phys. Rev. Lett. **91**, 130401 (2003).
[18] D. Roodenburg, J. W. Spronck, H. S. J. van der Zant, and W. J. Venstra, *Buckling beam micromechanical memory with on-chip readout*, Appl. Phys. Lett. **94**, 183501 (pages 3) (2009).
[19] S. Etaki, M. Poot, I. Mahboob, K. Onomitsu, H. Yamaguchi, and H. S. J. van der Zant, *Motion detection of a micromechanical resonator embedded in a d.c. SQUID*, Nat Phys **4**, 785 (2008).
[20] B. Witkamp, M. Poot, and H. S. J. van der Zant, *Bending-mode vibration of a suspended nanotube resonator*, Nano Lett. **6**, 2904 (2006).
[21] *Breakthrough of the year: Bridging the quantum and the classical worlds*, Science Magazine: `http://sciencecareers.sciencemag.org/career_magazine/previous_issues/articles/2010_12_17/caredit.a1000120` (2010).
[22] A. D. O'Connell, M. Hofheinz, M. Ansmann, R. C. Bialczak, M. Lenander, E. Lucero, M. Neeley, D. Sank, H. Wang, M. Weides, et al., *Quantum ground state and single-phonon control of a mechanical resonator*, Nature **464**, 697 (2010).
[23] J. D. Teufel, T. Donner, D. Li, J. W. Harlow, M. S. Allman, K. Cicak, A. J. Sirois, J. D. Whittaker, K. W. Lehnert, and R. W. Simmonds, *Sideband cooling of micromechanical motion to the quantum ground state*, Nature **475**, 359 (2011).
[24] K. S. Thorne, *Gravitational-wave research: Current status and future prospects*, Rev. Mod. Phys. **52**, 285 (1980).
[25] H. Billing, K. Maischberger, A. Rudiger, R. Schilling, L. Schnupp, and W. Winkler, *An argon laser interferometer for the detection of gravitational radiation*, J. Phys. E **12**, 1043 (1979).
[26] J. Weber, *Advances in gravitational radiation detection*, Gen. Rel. and Grav. **3**, 59 (1972).
[27] V. B. Braginsky and F. Y. Khalili, *Quantum measurement* (Nature Publishing Group, 1992).
[28] X. M. H. Huang, C. A. Zorman, M. Mehregany, and M. L. Roukes, *Nanoelectromechanical systems: Nanodevice motion at microwave frequencies*, Nature **421**, 496 (2003).
[29] R. G. Knobel and A. N. Cleland, *Nanometre-scale displacement sensing using a single electron transistor*, Nature **424**, 291 (2003).
[30] M. D. LaHaye, O. Buu, B. Camarota, and K. C. Schwab, *Approaching the Quantum Limit of a Nanomechanical Resonator*, Science **304**, 74 (2004).
[31] C. Metzger Höhberger and K. Karrai, *Cavity cooling of a microlever*, Nature **432**, 1002 (2004).
[32] A. Naik, O. Buu, M. D. LaHaye, A. D. Armour, A. A. Clerk, M. P. Blencowe, and K. C. Schwab, *Cooling a nanomechanical resonator with quantum back-action*, Nature **443**, 193 (2006).
[33] O. Arcizet, P.-F. Cohadon, T. Briant, M. Pinard, and A. Heidmann, *Radiation-pressure cooling and optomechanical instability of a micromirror*, Nature **444**, 71 (2006).
[34] D. Kleckner and D. Bouwmeester, *Sub-kelvin optical cooling of a micromechanical resonator*, Nature **444**, 75 (2006).
[35] S. Gigan, H. R. Bohm, M. Paternostro, F. Blaser, G. Langer, J. B. Hertzberg, K. C. Schwab, D. Bauerle, M. Aspelmeyer, and A. Zeilinger, *Self-cooling of a micromirror by radiation pressure*, Nature **444**, 67 (2006).
[36] O. Arcizet, P.-F. Cohadon, T. Briant, M. Pinard, A. Heidmann, J.-M. Mackowski, C. Michel, L. Pinard, O. Français, and L. Rousseau, *High-Sensitivity Optical Monitoring of a Micromechanical Resonator with a Quantum-Limited Optomechanical Sensor*, Phys. Rev. Lett. **97**, 133601 (pages 4) (2006).
[37] A. Schliesser, P. Del'Haye, N. Nooshi, K. J. Vahala, and T. J. Kippenberg, *Radiation Pressure Cooling of a Micromechanical Oscillator Using Dynamical Backaction*, Phys. Rev. Lett. **97**, 243905 (pages 4) (2006).
[38] M. Li, X. H.Tang, and M. L. Roukes, *Ultra-sensitive NEMS-based cantilevers for sensing, scanned probe and very high-frequency applications*, Nat Nano **2**, 114 (2007).
[39] T. Corbitt, Y. Chen, E. Innerhofer, H. Müller-Ebhardt, D. Ottaway, H. Rehbein, D. Sigg, S. Whitcomb, C. Wipf, and N. Mavalvala, *An All-Optical Trap for a Gram-Scale Mirror*, Phys. Rev. Lett. **98**, 150802 (pages 4) (2007).
[40] T. Corbitt, C. Wipf, T. Bodiya, D. Ottaway, D. Sigg, N. Smith, S. Whitcomb, and N. Mavalvala, *Optical Dilution and Feedback Cooling of a Gram-Scale Oscillator to 6.9 mK*, Phys. Rev. Lett. **99**, 160801 (2007).
[41] I. Favero, C. Metzger, S. Camerer, D. König, H. Lorenz, J. P. Kotthaus, and K. Karrai, *Optical cooling of a micromirror of wavelength size*, Appl. Phys. Lett. **90**, 104101 (pages 3) (2007).
[42] N. E. Flowers-Jacobs, D. R. Schmidt, and K. W. Lehnert, *Intrinsic Noise Properties of Atomic Point Contact Displacement Detectors*, Phys. Rev. Lett. **98**, 096804 (pages 4) (2007).
[43] M. Poggio, C. L. Degen, H. J. Mamin, and D. Rugar, *Feedback Cooling of a Cantilever's Fundamental Mode below 5 mK*, Phys. Rev. Lett. **99**, 017201 (pages 4) (2007).
[44] K. R. Brown, J. Britton, R. J. Epstein, J. Chiaverini, D. Leibfried, and D. J. Wineland, *Passive Cooling of a Micromechanical Oscillator with a Resonant Electric Circuit*, Phys. Rev. Lett. **99**, 137205 (pages 4) (2007).

[45] T. Caniard, P. Verlot, T. Briant, P.-F. Cohadon, and A. Heidmann, *Observation of Back-Action Noise Cancellation in Interferometric and Weak Force Measurements*, Phys. Rev. Lett. **99**, 110801 (pages 4) (2007).
[46] J. D. Thompson, B. M. Zwickl, A. M. Jayich, F. Marquardt, S. M. Girvin, and J. G. E. Harris, *Strong dispersive coupling of a high-finesse cavity to a micromechanical membrane*, Nature **452**, 72 (2008).
[47] S. Gröblacher, S. Gigan, H. R. Bhm, A. Zeilinger, and M. Aspelmeyer, *Radiation-pressure self-cooling of a micromirror in a cryogenic environment*, EPL **81**, 54003 (2008).
[48] C. M. Mow-Lowry, A. J. Mullavey, S. Goßler, M. B. Gray, and D. E. McClelland, *Cooling of a Gram-Scale Cantilever Flexure to 70 mK with a Servo-Modified Optical Spring*, Phys. Rev. Lett. **100**, 010801 (2008).
[49] A. Schliesser, R. Riviere, G. Anetsberger, O. Arcizet, and T. Kippenberg, *Resolved-sideband cooling of a micromechanical oscillator*, Nat Phys **4**, 415 (2008).
[50] C. A. Regal, J. D. Teufel, and K. W. Lehnert, *Measuring nanomechanical motion with a microwave cavity interferometer*, Nat Phys **4**, 555 (2008).
[51] X. L. Feng, C. J. White, A. Hajimiri, and M. L. Roukes, *A self-sustaining ultrahigh-frequency nanoelectromechanical oscillator*, Nat Nano **3**, 342 (2008).
[52] M. Poggio, M. P. Jura, C. L. Degen, M. A. Topinka, H. J. Mamin, D. Goldhaber-Gordon, and D. Rugar, *An off-board quantum point contact as a sensitive detector of cantilever motion*, Nat Phys **4**, 635 (2008).
[53] A. Vinante, M. Bignotto, M. Bonaldi, M. Cerdonio, L. Conti, P. Falferi, N. Liguori, S. Longo, R. Mezzena, A. Ortolan, et al., *Feedback Cooling of the Normal Modes of a Massive Electromechanical System to Submillikelvin Temperature*, Phys. Rev. Lett. **101**, 033601 (pages 4) (2008).
[54] N. Liu, F. Giesen, M. Belov, J. Losby, J. Moroz, E. A. Fraser, G. McKinnon, J. T. Clement, V. Sauer, K. W. Hiebert, et al., *Time-domain control of ultrahigh-frequency nanomechanical systems*, Nat Nano **3**, 715 (2008).
[55] M. Li, W. H. P. Pernice, C. Xiong, T. Baehr-Jones, M. Hochberg, and H. X. Tang, *Harnessing optical forces in integrated photonic circuits*, Nature **456**, 480 (2008).
[56] J. D. Teufel, J. W. Harlow, C. A. Regal, and K. W. Lehnert, *Dynamical Backaction of Microwave Fields on a Nanomechanical Oscillator*, Phys. Rev. Lett. **101**, 197203 (pages 4) (2008).
[57] Q. P. Unterreithmeier, E. M. Weig, and J. P. Kotthaus, *Universal transduction scheme for nanomechanical systems based on dielectric forces*, Nature **458**, 1001 (2009).
[58] K. H. Lee, T. G. McRae, G. I. Harris, J. Knittel, and W. P. Bowen, *Cooling and Control of a Cavity Optoelectromechanical System*, Phys. Rev. Lett. **104**, 123604 (2010).
[59] M. Li, W. H. P. Pernice, and X. H. Tang, *Broadband all-photonic transduction of nanocantilevers*, Nat Nano **4**, 377 (2009).
[60] S. Gröblacher, J. B. Hertzberg, M. R. Vanner, G. D. Cole, S. Gigan, K. C. Schwab, and M. Aspelmeyer, *Demonstration of an ultracold micro-optomechanical oscillator in a cryogenic cavity*, Nat Phys **5**, 485 (2009).
[61] A. Schliesser, O. Arcizet, R. Riviere, G. Anetsberger, and T. J. Kippenberg, *Resolved-sideband cooling and position measurement of a micromechanical oscillator close to the Heisenberg uncertainty limit*, Nat Phys **5**, 509 (2009).
[62] M. Eichenfield, R. Camacho, J. Chan, K. J. Vahala, and O. Painter, *A picogram- and nanometre-scale photonic-crystal optomechanical cavity*, Nature **459**, 550 (2009).
[63] Y.-S. Park and H. Wang, *Resolved-sideband and cryogenic cooling of an optomechanical resonator*, Nat Phys **5**, 489 (2009).
[64] B. Abbott *et al.*, *Observation of a kilogram-scale oscillator near its quantum ground state*, New J. Phys. **11**, 073032 (2009).
[65] Q. Lin, J. Rosenberg, X. Jiang, K. J. Vahala, and O. Painter, *Mechanical Oscillation and Cooling Actuated by the Optical Gradient Force*, Phys. Rev. Lett. **103**, 103601 (2009).
[66] J. D. Teufel, T. Donner, M. A. Castellanos-Beltran, J. W. Harlow, and K. W. Lehnert, *Nanomechanical motion measured with an imprecision below that at the standard quantum limit*, Nat Nano **4**, 820 (2009).
[67] G. Anetsberger, O. Arcizet, Q. P. Unterreithmeier, R. Riviere, A. Schliesser, E. M. Weig, J. P. Kotthaus, and T. J. Kippenberg, *Near-field cavity optomechanics with nanomechanical oscillators*, Nat Phys **5**, 909 (2009).
[68] T. Rocheleau, T. Ndukum, C. Macklin, J. B. Hertzberg, A. A. Clerk, and K. C. Schwab, *Preparation and detection of a mechanical resonator near the ground state of motion*, Nature **463**, 72 (2010).
[69] G. Anetsberger, E. Gavartin, O. Arcizet, Q. P. Unterreithmeier, E. M. Weig, M. L. Gorodetsky, J. P. Kotthaus, and T. J. Kippenberg, *Measuring nanomechanical motion with an imprecision below the standard quantum limit*, Phys. Rev. A **82**, 061804 (2010).
[70] M. Poot, S. Etaki, H. Yamaguchi, and H. S. J. van der Zant, *Discrete-time quadrature feedback cooling of a radio-frequency mechanical resonator*, Appl. Phys. Lett. **99**, 013113 (2011).
[71] M. Imboden, P. Mohanty, A. Gaidarzhy, J. Rankin, and B. W. Sheldon, *Scaling of dissipation in megahertz-range micromechanical diamond oscillators*, Appl. Phys. Lett. **90**, 173502 (pages 3) (2007).
[72] Q. P. Unterreithmeier, T. Faust, and J. P. Kotthaus, *Damping of Nanomechanical Resonators*, Phys. Rev. Lett. **105**, 027205 (2010).
[73] V. Sazonova, Y. Yaish, H. Üstünel, D. Roundy, T. A. Arias, and P. L. McEuen, *A tunable carbon nanotube electromechanical oscillator*, Nature **431**, 284 (2004).
[74] K. Jensen, J. Weldon, H. Garcia, and A. Zettl, *Nanotube Radio*, Nano Lett. **7**, 3508 (2007).
[75] D. Garcia-Sanchez, A. S. Paulo, M. J. Esplandiu, F. Perez-Murano, L. Forró, A. Aguasca, and A. Bachtold, *Mechanical Detection of Carbon Nanotube Resonator Vibrations*, Phys. Rev. Lett. **99**, 085501 (pages 4) (2007).
[76] B. Lassagne, D. Garcia-Sanchez, A. Aguasca, and A. Bachtold, *Ultrasensitive Mass Sensing with a Nanotube Electromechanical Resonator*, Nano Lett. **8**, 3735 (2008).
[77] K. Jensen, K. Kim, and A. Zettl, *An atomic-resolution nanomechanical mass sensor*, Nat Nano **3**, 533 (2008).
[78] H.-Y. Chiu, P. Hung, H. W. C. Postma, and M. Bockrath, *Atomic-Scale Mass Sensing Using Carbon Nanotube Resonators*, Nano Lett. **8**, 4342 (2008).
[79] L. B. Biedermann, R. C. Tung, A. Raman, and R. G. Reifenberger, *Flexural vibration spectra of carbon nanotubes measured using laser Doppler vibrometry*, Nanotechnology **20**, 035702 (2009).
[80] A. Eriksson, S. Lee, A. A. Sourab, A. Isacsson, R. Kaunisto, J. M. Kinaret, and E. E. B. Campbell, *Direct Transmission Detection of Tunable Mechanical Resonance in an Individual Carbon Nanofiber Relay*, Nano Lett. **8**, 1224 (2008).
[81] A. K. Hüttel, G. A. Steele, B. Witkamp, M. Poot, L. P. Kouwenhoven, and H. S. J. van der Zant, *Carbon Nanotubes as Ultrahigh Quality Factor Mechanical Resonators*, Nano Lett. **9**, 2547 (2009).
[82] B. Lassagne, Y. Tarakanov, J. Kinaret, D. Garcia-Sanchez, and A. Bachtold, *Coupling Mechanics to Charge Transport in Carbon Nanotube Mechanical Resonators*, Science **325**, 1107 (2009).
[83] Z. Wang, J. Wei, P. Morse, J. G. Dash, O. E. Vilches, and D. H. Cobden, *Phase Transitions of Adsorbed Atoms on the Surface of a Carbon Nanotube*, Science **327**, 552 (2010).
[84] H. Cho, M.-F. Yu, A. F. Vakakis, L. A. Bergman, and D. M. McFarland, *Tunable, Broadband Nonlinear Nanomechanical Resonator*, Nano Lett. **10**, 1793 (2010).

[85] V. Gouttenoire, T. Barois, S. Perisanu, J.-L. Leclercq, S. T. Purcell, P. Vincent, and A. Ayari, *Digital and FM Demodulation of a Doubly Clamped Single-Walled Carbon-Nanotube Oscillator: Towards a Nanotube Cell Phone*, Small **6**, 1060 (2010).
[86] A. Husain, J. Hone, H. W. C. Postma, X. M. H. Huang, T. Drake, M. Barbic, A. Scherer, and M. L. Roukes, *Nanowire-based very-high-frequency electromechanical resonator*, Appl. Phys. Lett. **83**, 1240 (2003).
[87] X. L. Feng, R. He, P. Yang, and M. L. Roukes, *Very High Frequency Silicon Nanowire Electromechanical Resonators*, Nano Lett. **7**, 1953 (2007).
[88] C.-Y. Nam, P. Jaroenapibal, D. Tham, D. E. Luzzi, S. Evoy, and J. E. Fischer, *Diameter-Dependent Electromechanical Properties of GaN Nanowires*, Nano Lett. **6**, 153 (2006).
[89] T. Henry, K. Kim, Z. Ren, C. Yerino, J. Han, and H. X. Tang, *Directed Growth of Horizontally Aligned Gallium Nitride Nanowires for Nanoelectromechanical Resonator Arrays*, Nano Lett. **7**, 3315 (2007).
[90] S. Perisanu, P. Vincent, A. Ayari, M. Choueib, S. T. Purcell, M. Bechelany, and D. Cornu, *High Q factor for mechanical resonances of batch-fabricated SiC nanowires*, Appl. Phys. Lett. **90**, 043113 (pages 3) (2007).
[91] M. Belov, N. J. Quitoriano, S. Sharma, W. K. Hiebert, T. I. Kamins, and S. Evoy, *Mechanical resonance of clamped silicon nanowires measured by optical interferometry*, J. Appl. Phys. **103**, 074304 (pages 7) (2008).
[92] M. Li, R. B. Bhiladvala, T. J. Morrow, J. A. Sioss, K.-K. Lew, J. M. Redwing, C. D. Keating, and T. S. Mayer, *Bottom-up assembly of large-area nanowire resonator arrays*, Nat Nano **3**, 88 (2008).
[93] R. He, X. L. Feng, M. L. Roukes, and P. Yang, *Self-Transducing Silicon Nanowire Electromechanical Systems at Room Temperature*, Nano Lett. **8**, 1756 (2008).
[94] R. Zhu, D. Wang, S. Xiang, Z. Zhou, and X. Ye, *Piezoelectric characterization of a singlezinc oxide nanowire using a nanoelectromechanical oscillator*, Nanotechnology **19**, 285712 (2008).
[95] J. M. Nichol, E. R. Hemesath, L. J. Lauhon, and R. Budakian, *Displacement detection of silicon nanowires by polarization-enhanced fiber-optic interferometry*, Appl. Phys. Lett. **93**, 193110 (2008).
[96] W. Y. Fung, E. N. Dattoli, and W. Lu, *Radio frequency nanowire resonators and in situ frequency tuning*, Appl. Phys. Lett. **94**, 203104 (pages 3) (2009).
[97] E. Gil-Santos, D. Ramos, J. Martinez, M. Fernandez-Regulez, R. Garcia, A. San Paulo, M. Calleja, and J. Tamayo, *Nanomechanical mass sensing and stiffness spectrometry based on two-dimensional vibrations of resonant nanowires*, Nat Nano **5**, 641 (2010).
[98] J. S. Bunch, A. M. van der Zande, S. S. Verbridge, I. W. Frank, D. M. Tanenbaum, J. M. Parpia, H. G. Craighead, and P. L. McEuen, *Electromechanical resonators from graphene sheets*, Science **315**, 490 (2007).
[99] D. Garcia-Sanchez, A. M. van der Zande, A. S. Paulo, B. Lassagne, P. L. McEuen, and A. Bachtold, *Imaging Mechanical Vibrations in Suspended Graphene Sheets*, Nano Letters **8**, 1399 (2008).
[100] J. S. Bunch, S. S. Verbridge, J. S. Alden, A. M. van der Zande, J. M. Parpia, H. G. Craighead, and P. L. McEuen, *Impermeable Atomic Membranes from Graphene Sheets*, Nano Lett. **8**, 2458 (2008).
[101] J. T. Robinson, M. Zalalutdinov, J. W. Baldwin, E. S. Snow, Z. Wei, P. Sheehan, and B. H. Houston, *Wafer-scale Reduced Graphene Oxide Films for Nanomechanical Devices*, Nano Letters **8**, 3441 (2008).
[102] S. Shivaraman, R. A. Barton, X. Yu, J. Alden, L. Herman, M. Chandrashekhar, J. Park, P. L. McEuen, J. M. Parpia, H. G. Craighead, et al., *Free-Standing Epitaxial Graphene*, Nano Letters **9**, 3100 (2009).
[103] C. Chen, S. Rosenblatt, K. I. Bolotin, W. Kalb, P. Kim, I. Kymissis, H. L. Stormer, T. F. Heinz, and J. Hone, *Performance of monolayer graphene nanomechanical resonators with electrical readout*, Nat Nano **4**, 861 (2009).
[104] V. Singh, S. Sengupta, H. S. Solanki, R. Dhall, A. Allain, S. Dhara, P. Pant, and M. M. Deshmukh, *Probing thermal expansion of graphene and modal dispersion at low-temperature using graphene nanoelectromechanical systems resonators*, Nanotechnology **21**, 165204 (2010).
[105] S. Sengupta, H. S. Solanki, V. Singh, S. Dhara, and M. M. Deshmukh, *Electromechanical resonators as probes of the charge density wave transition at the nanoscale in $NbSe_2$*, Phys. Rev. B **82**, 155432 (2010).
[106] G. A. Steele, A. K. Huttel, B. Witkamp, M. Poot, H. B. Meerwaldt, L. P. Kouwenhoven, and H. S. J. van der Zant, *Strong Coupling Between Single-Electron Tunneling and Nanomechanical Motion*, Science **325**, 1103 (2009).
[107] M. Poot and H. S. J. van der Zant, *Nanomechanical properties of few-layer graphene membranes*, Appl. Phys. Lett. **92**, 063111 (pages 3) (2008).
[108] H. W. Kroto, J. R. Heath, S. C. O'Brien, R. F. Curl, and R. E. Smalley, *C60: Buckminsterfullerene*, Nature **318**, 162 (1985).
[109] S. Iijima, *Helical microtubules of graphitic carbon*, Nature **354**, 56 (1991).
[110] K. S. Novoselov, A. K. Geim, S. V. Morozov, D. Jiang, Y. Zhang, S. V. Dubonos, I. V. Grigorieva, and A. A. Firsov, *Electric Field Effect in Atomically Thin Carbon Films*, Science **306**, 666 (2004).
[111] K. S. Novoselov, D. Jiang, F. Schedin, T. J. Booth, V. V. Khotkevich, S. V. Morozov, and A. K. Geim, *Two-dimensional atomic crystals*, Proc. Natl. Acad. Sci. U. S. A. **102**, 10451 (2005).
[112] A. K. Geim, *Graphene: Status and Prospects*, Science **324**, 1530 (2009).
[113] S. Bae, H. Kim, Y. Lee, X. Xu, J.-S. Park, Y. Zheng, J. Balakrishnan, T. Lei, H. Ri Kim, Y. I. Song, et al., *Roll-to-roll production of 30-inch graphene films for transparent electrodes*, Nat Nano **5**, 574 (2010).
[114] L. D. Landau and E. M. Lifshitz, *Statistical Physics, Part I* (Pergamon Press, Oxford, 1980).
[115] J. C. Meyer, A. K. Geim, M. I. Katsnelson, K. S. Novoselov, T. J. Booth, and S. Roth, *The structure of suspended graphene sheets*, Nature **446**, 60 (2007).
[116] A. Fasolino, J. H. Los, and M. I. Katsnelson, *Intrinsic ripples in graphene*, Nat Mater **6**, 858 (2007).
[117] P. Liu and Y. W. Zhang, *Temperature-dependent bending rigidity of graphene*, Appl. Phys. Lett. **94**, 231912 (pages 3) (2009).
[118] D. Gazit, *Theory of the spontaneous buckling of doped graphene*, Phys. Rev. B **79**, 113411 (pages 4) (2009).
[119] L. Sekaric, J. M. Parpia, H. G. Craighead, T. Feygelson, B. H. Houston, and J. E. Butler, *Nanomechanical resonant structures in nanocrystalline diamond*, Appl. Phys. Lett. **81**, 4455 (2002).
[120] J. Wang, J. Butler, T. Feygelson, and C.-C. Nguyen, in *Micro Electro Mechanical Systems, 2004. 17th IEEE International Conference on. (MEMS)* (2004), pp. 641 – 644.
[121] A. Gaidarzhy, M. Imboden, P. Mohanty, J. Rankin, and B. W. Sheldon, *High quality factor gigahertz frequencies in nanomechanical diamond resonators*, Appl. Phys. Lett. **91**, 203503 (pages 3) (2007).
[122] A. Schliesser and T. J. Kippenberg (Academic Press, 2010), vol. Volume 58, pp. 207–323, URL `http://www.sciencedirect.com/science/article/B8JD4-50DVWSK-B/2/bab4cd708e81b940b6b862ba8feefaa1`.
[123] M. Eichenfield, J. Chan, R. M. Camacho, K. J. Vahala, and O. Painter, *Optomechanical crystals*, Nature **462**, 78 (2009).
[124] T. Dunn, J.-S. Wenzler, and P. Mohanty, *Anharmonic modal coupling in a bulk micromechanical resonator*, Appl. Phys. Lett. **97**, 123109 (pages 3) (2010).
[125] A. Erbe, C. Weiss, W. Zwerger, and R. H. Blick, *Nanomechanical Resonator Shuttling Single Electrons at Radio Frequencies*, Phys. Rev. Lett. **87**, 096106 (2001).
[126] B. Witkamp, M. Poot, H. Pathangi, A. K. Hüttel, and H. S. J. van der Zant, *Self-detecting gate-tunable nanotube paddle resonators*, Appl. Phys.

Lett. **93**, 111909 (pages 3) (2008).
[127] G. S. Wiederhecker, L. Chen, A. Gondarenko, and M. Lipson, *Controlling photonic structures using optical forces*, Nature **462**, 633 (2009).
[128] W. H. P. Pernice, M. Li, K. Y. Fong, and H. X. Tang, *Modeling of the optical force between propagating lightwaves in parallel 3D waveguides*, Opt. Express **17**, 16032 (2009).
[129] M. Dequesnes, S. V. Rotkin, and N. R. Aluru, *Calculation of pull-in voltages for carbon-nanotube-based nanoelectromechanical switches*, Nanotechnology **13**, 120 (2002).
[130] J. Patrick Wilber, C. B. Clemons, G. W. Young, A. Buldum, and D. D. Quinn, *Continuum and atomistic modeling of interacting graphene layers*, Phys. Rev. B **75**, 045418 (2007).
[131] C. D. Reddy, S. Rajendran, and K. M. Liew, *Equilibrium configuration and continuum elastic properties of finite sized graphene*, Nanotechnology **17**, 864 (2006).
[132] K. Samadikhah, J. Atalaya, C. Huldt, A. Isacsson, and J. Kinaret, *General Elasticity Theory for Graphene Membranes Based on Molecular Dynamics*, Mater. Res. Soc. Symp. Proc. **1057**, 20 (2008).
[133] F. Scarpa, S. Adhikari, and A. S. Phani, *Effective elastic mechanical properties of single layer graphene sheets*, Nanotechnology **20**, 065709 (2009).
[134] M. Neek-Amal and R. Asgari, *Nano-indentation of circular graphene flakes*, arXiv:0903.5035 (2009).
[135] R. Lefèvre, M. F. Goffman, V. Derycke, C. Miko, L. Forró, J. P. Bourgoin, and P. Hesto, *Scaling Law in Carbon Nanotube Electromechanical Devices*, Phys. Rev. Lett. **95**, 185504 (pages 4) (2005).
[136] T. J. Chung, *Applied Continuum Mechanics* (Cambridge University Press, 1996).
[137] R. E. Newnham, *Properties of materials: anisotropy, symmetry, structure* (Oxford University Press, 2005).
[138] L. D. Landau and E. M. Lifshitz, *Theory of elasticity* (Butterworth-Heineman, 1986).
[139] K. Yamazaki, T. Yamaguchi, and H. Yamaguchi, *Modulation of Young's Modulus of Poly(methyl methacrylate) Nanobeam Due to Electron-Beam Exposure*, Japanese Journal of Applied Physics **46**, L1225 (2007).
[140] D. R. Lide, ed., *Handbook of Chemistry and Physics* (GRC press, 1974).
[141] J. Turley and G. Sines, *The anisotropy of Young's modulus, shear modulus and Poisson's ratio in cubic materials*, J. Phys. D **4**, 264 (1971).
[142] J. C. Slonczewski and P. R. Weiss, *Band Structure of Graphite*, Phys. Rev. **109**, 272 (1958).
[143] O. L. Blakslee, D. G. Proctor, E. J. Seldin, G. B. Spence, and T. Weng, *Elastic Constants of Compression-Annealed Pyrolytic Graphite*, J. Appl. Phys. **41**, 3373 (1970).
[144] K. H. Michel and B. Verberck, *Theory of the elastic constants of graphite and graphene*, Phys. Stat. Sol. (b) **245**, 2177 (2008).
[145] M. E. Gurtin, J. Weissmüler, and F. Larché, *A general theory of curved deformable interfaces in solids at equilibrium*, Philosophical Magazine A **78**, 1093 (1998).
[146] M. J. Lachut and J. E. Sader, *Effect of Surface Stress on the Stiffness of Cantilever Plates*, Phys. Rev. Lett. **99**, 206102 (2007).
[147] A. N. Cleland, M. Pophristic, and I. Ferguson, *Single-crystal aluminum nitride nanomechanical resonators*, Appl. Phys. Lett. **79**, 2070 (2001).
[148] K. Babaei Gavan, E. W. J. M. van der Drift, W. J. Venstra, M. R. Zuiddam, and van der Zant H. S. J., *Effect of undercut on the resonant behaviour of silicon nitride cantilevers*, Journal of Micromechanics and Microengineering **19**, 035003 (2009).
[149] H. Yamaguchi, K. Kato, Y. Nakai, K. Onomitsu, S. Warisawa, and S. Ishihara, *Improved resonance characteristics of GaAs beam resonators by epitaxially induced strain*, Appl. Phys. Lett. **92**, 251913 (pages 3) (2008).
[150] T. Watanabe, K. Onomitsu, and H. Yamaguchi, *Feedback Cooling of a Strained GaAs Micromechanical Beam Resonator*, Appl. Phys. Expr. **3**, 065201 (2010).
[151] S. S. Verbridge, D. F. Shapiro, H. G. Craighead, and J. M. Parpia, *Macroscopic Tuning of Nanomechanics: Substrate Bending for Reversible Control of Frequency and Quality Factor of Nanostring Resonators*, Nano Lett. **7**, 1728 (2007).
[152] S. S. Verbridge, J. M. Parpia, R. B. Reichenbach, L. M. Bellan, and H. G. Craighead, *High quality factor resonance at room temperature with nanostrings under high tensile stress*, Journal of Applied Physics **99**, 124304 (pages 8) (2006).
[153] S. S. Verbridge, H. G. Craighead, and J. M. Parpia, *A megahertz nanomechanical resonator with room temperature quality factor over a million*, Applied Physics Letters **92**, 013112 (pages 3) (2008).
[154] K. Y. Fong, W. H. P. Pernice, M. Li, and H. X. Tang, *High Q optomechanical resonators in silicon nitride nanophotonic circuits*, Appl. Phys. Lett. **97**, 073112 (2010).
[155] S. Carr, W. Lawrence, and M. Wybourne, *Static buckling and actuation of free-standing mesoscale beams*, IEEE T. Nanotechnol. **4**, 655 (2005).
[156] W. E. Lawrence, M. N. Wybourne, and S. M. Carr, *Compressional mode softening and Euler buckling patterns in mesoscopic beams*, New J. Phys. **8**, 223 (2006).
[157] A. H. Nayfeh, W. Kreider, and T. J. Anderson, *Investigation of natural frequencies and mode shapes of bukcled beams*, AIAA Journal **33**, 1121 (1995).
[158] S. Sapmaz, Y. M. Blanter, L. Gurevich, and H. S. J. van der Zant, *Carbon nanotubes as nanoelectromechanical systems*, Phys. Rev. B **67**, 235414 (2003).
[159] M. Poot, B. Witkamp, M. A. Otte, and H. S. J. van der Zant, *Modelling suspended carbon nanotube resonators*, Phys. Stat. Sol. (b) **244**, 4252 (2007).
[160] P. Poncharal, Z. L. Wang, D. Ugarte, and W. A. de Heer, *Electrostatic Deflections and Electromechanical Resonances of Carbon Nanotubes*, Science **283**, 1513 (1999).
[161] D. J. Griffiths, *Introduction to Electrodynamics* (Prentice Hall, Upper Saddle River, 1999).
[162] Y. K. Kwok, *Applied complex variables for scientists and engineers* (Cambridge University Press, Cambridge, 2002).
[163] I. Kozinsky, H. W. C. Postma, I. Bargatin, and M. L. Roukes, *Tuning nonlinearity, dynamic range, and frequency of nanomechanical resonators*, Appl. Phys. Lett. **88**, 253101 (pages 3) (2006).
[164] H. J. R. Westra, M. Poot, H. S. J. van der Zant, and W. J. Venstra, *Nonlinear Modal Interactions in Clamped-Clamped Mechanical Resonators*, Phys. Rev. Lett. **105**, 117205 (2010).
[165] M. Poot, *Mechanical systems at the nanoscale*, Ph.D. thesis, Delft University of Technology (2009), URL `http://resolver.tudelft.nl/uuid:4dae1617-37e1-4b1f-8013-f6455a6678fb`.
[166] T. W. Tombler, C. Zhou, L. Alexseyev, J. Kong, H. Dai, L. Liu, C. S. Jayanthi, M. Tang, and S.-Y. Wu, *Reversible electromechanical characteristics of carbon nanotubes under local-probe manipulation*, Nature **405**, 769 (2000).
[167] E. D. Minot, Y. Yaish, V. Sazonova, J.-Y. Park, M. Brink, and P. L. McEuen, *Tuning Carbon Nanotube Band Gaps with Strain*, Phys. Rev. Lett. **90**, 156401 (2003).
[168] D. A. Walters, L. M. Ericson, M. J. Casavant, J. Liu, D. T. Colbert, K. A. Smith, and R. E. Smalley, *Elastic strain of freely suspended single-wall carbon nanotube ropes*, Appl. Phys. Lett. **74**, 3803 (1999).
[169] D. Bozovic, M. Bockrath, J. H. Hafner, C. M. Lieber, H. Park, and M. Tinkham, *Plastic deformations in mechanically strained single-walled carbon nanotubes*, Phys. Rev. B **67**, 033407 (2003).

[170] Q. Zhao, M. B. Nardelli, and J. Bernholc, *Ultimate strength of carbon nanotubes: A theoretical study*, Phys. Rev. B **65**, 144105 (2002).
[171] T. J. Booth, P. Blake, R. R. Nair, D. Jiang, E. W. Hill, U. Bangert, A. Bleloch, M. Gass, K. S. Novoselov, M. I. Katsnelson, et al., *Macroscopic Graphene Membranes and Their Extraordinary Stiffness*, Nano Lett. **8**, 2442 (2008).
[172] C. Lee, X. Wei, J. W. Kysar, and J. Hone, *Measurement of the Elastic Properties and Intrinsic Strength of Monolayer Graphene*, Science **321**, 385 (2008).
[173] I. W. Frank, D. M. Tanenbaum, A. M. van der Zande, and P. L. McEuen (AVS, 2007), vol. 25, pp. 2558–2561, URL `http://link.aip.org/link/?JVB/25/2558/1`.
[174] F. Traversi, F. J. Gzman-Vzquez, L. G. Rizzi, V. Russo, C. S. Casari, C. Gmez-Navarro, and R. Sordan, *Elastic properties of graphene suspended on a polymer substrate by e-beam exposure*, New J. Phys. **12**, 023034 (2010).
[175] C. Gómez-Navarro, M. Burghard, and K. Kern, *Elastic Properties of Chemically Derived Single Graphene Sheets*, Nano Lett. **8**, 2045 (2008).
[176] C. Li, Y. Bando, C. Zhi, Y. Huang, and D. Golberg, *Thickness-dependent bending modulus of hexagonal boron nitride nanosheets*, Nanotechnology **20**, 385707 (2009).
[177] L. Song, L. Ci, H. Lu, P. B. Sorokin, C. Jin, J. Ni, A. G. Kvashnin, D. G. Kvashnin, J. Lou, B. I. Yakobson, et al., *Large Scale Growth and Characterization of Atomic Hexagonal Boron Nitride Layers*, Nano Lett. **10**, 3209 (2010).
[178] B. I. Yakobson, C. J. Brabec, and J. Bernholc, *Nanomechanics of Carbon Tubes: Instabilities beyond Linear Response*, Phys. Rev. Lett. **76**, 2511 (1996).
[179] A. H. Castro Neto, F. Guinea, N. M. R. Peres, K. S. Novoselov, and A. K. Geim, *The electronic properties of graphene*, Rev. Mod. Phys. **81**, 109 (pages 54) (2009).
[180] K.-T. Wan, S. Guo, and D. A. Dillard, *A theoretical and numerical study of a thin clamped circular film under an external load in the presence of a tensile residual stress*, Thin Solid Films **425**, 150 (2003).
[181] D. Norouzi, M. M. Mueller, and M. Deserno, *How to determine local elastic properties of lipid bilayer membranes from atomic-force-microscope measurements: A theoretical analysis*, Phys. Rev. E **74**, 061914 (2006).
[182] J. Atalaya, A. Isacsson, and J. M. Kinaret, *Continuum Elastic Modeling of Graphene Resonators*, Nano Lett. **8**, 4196 (2008).
[183] D. Rugar and P. Grütter, *Mechanical parametric amplification and thermomechanical noise squeezing*, Phys. Rev. Lett. **67**, 699 (1991).
[184] R. Almog, S. Zaitsev, O. Shtempluck, and E. Buks, *Noise Squeezing in a Nanomechanical Duffing Resonator*, Phys. Rev. Lett. **98**, 078103 (2007).
[185] W. Y. Huo and G. L. Long, *Generation of squeezed states of nanomechanical resonator using three-wave mixing*, Appl. Phys. Lett. **92**, 133102 (pages 3) (2008).
[186] J. Zhang, Y. xi Liu, and F. Nori, *Cooling and squeezing the fluctuations of a nanomechanical beam by indirect quantum feedback control*, Phys. Rev. A **79**, 052102 (pages 14) (2009).
[187] K. Jähne, C. Genes, K. Hammerer, M. Wallquist, E. S. Polzik, and P. Zoller, *Cavity-assisted squeezing of a mechanical oscillator*, Phys. Rev. A **79**, 063819 (2009).
[188] G. Filatrella, N. Pedersen, and K. Wiesenfeld, *High-Q cavity-induced synchronization in oscillator arrays*, Phys. Rev. E **61**, 2513 (2000).
[189] M. C. Cross, A. Zumdieck, R. Lifshitz, and J. L. Rogers, *Synchronization by Nonlinear Frequency Pulling*, Phys. Rev. Lett. **93**, 224101 (2004).
[190] D. Chang and N. Popplewell, *A non-uniform, axially loaded euler-bernoulli beam having complex ends*, Q. J. Mech. Appl. Math. **49**, 353 (1996).
[191] A. N. Cleland and M. L. Roukes, *Noise processes in nanomechanical resonators*, J. Appl. Phys. **92**, 2758 (2002).
[192] H. W. C. Postma, I. Kozinsky, A. Husain, and M. L. Roukes, *Dynamic range of nanotube- and nanowire-based electromechanical systems*, Appl. Phys. Lett. **86**, 223105 (pages 3) (2005).
[193] R. B. Karabalin, M. C. Cross, and M. L. Roukes, *Nonlinear dynamics and chaos in two coupled nanomechanical resonators*, Phys. Rev. B **79**, 165309 (pages 5) (2009).
[194] S.-B. Shim, M. Imboden, and P. Mohanty, *Synchronized Oscillation in Coupled Nanomechanical Oscillators*, Science **316**, 95 (2007).
[195] H. Okamoto, T. Kamada, K. Onomitsu, I. Mahboob, and H. Yamaguchi, *Optical Tuning of Coupled Micromechanical Resonators*, Applied Physics Express **2**, 062202 (2009).
[196] Q. Lin, J. Rosenberg, D. Chang, R. Camacho, M. Eichenfield, K. J. Vahala, and O. Painter, *Coherent mixing of mechanical excitations in nano-optomechanical structures*, Nat Photon **4**, 236 (2010).
[197] M. I. Dykman and M. A. Krivoglaz, *THEORY OF NONLINEAR OSCILLATOR INTERACTING WITH A MEDIUM*, Sov. Sci. Rev. A Phys **5**, 265 (1984).
[198] S. H. Strogatz, *Nonlinear dynamics and chaos* (Persues books publishing, LLC, 2000).
[199] A. V. Oppenheim, A. S. Willsky, and S. Hamid, *Signals and Systems*, Prentice Hall signal processing series (Prentice Hall, 1997), 2nd ed.
[200] K. S. Shanmugan and A. M. Breipohl, *Random Signals: Detection, Estimation and Data Analysis* (John Wiley and Sons, 1988).
[201] C. Kittel and H. Kroemer, *Thermal Physics* (W. H. Freeman, 2000).
[202] H. Nyquist, *Thermal Agitation of Electric Charge in Conductors*, Phys. Rev. **32**, 110 (1928).
[203] J. Weber, *Fluctuation Dissipation Theorem*, Phys. Rev. **101**, 1620 (1956).
[204] H. B. Callen and T. A. Welton, *Irreversibility and Generalized Noise*, Phys. Rev. **83**, 34 (1951).
[205] K. Jacobs and D. A. Steck, *A straightforward introduction to continuous quantum measurement*, Contemporary Physics **47**, 279 (2006).
[206] A. A. Clerk, *Quantum-limited position detection and amplification: A linear response perspective*, Phys. Rev. B **70**, 245306 (2004).
[207] A. A. Clerk, M. H. Devoret, S. M. Girvin, F. Marquardt, and R. J. Schoelkopf, *Introduction to quantum noise, measurement, and amplification*, Rev. Mod. Phys. **82**, 1155 (2010).
[208] C. M. Caves, *Quantum limits on noise in linear amplifiers*, Phys. Rev. D **26**, 1817 (1982).
[209] I. Tittonen, G. Breitenbach, T. Kalkbrenner, T. Müller, R. Conradt, S. Schiller, E. Steinsland, N. Blanc, and N. F. de Rooij, *Interferometric measurements of the position of a macroscopic body: Towards observation of quantum limits*, Phys. Rev. A **59**, 1038 (1999).
[210] H. A. Haus and J. A. Mullen, *Quantum Noise in Linear Amplifiers*, Phys. Rev. **128**, 2407 (1962).
[211] G. Jourdan, F. Comin, and J. Chevrier, *Mechanical Mode Dependence of Bolometric Backaction in an Atomic Force Microscopy Microlever*, Phys. Rev. Lett. **101**, 133904 (pages 4) (2008).
[212] A. A. Clerk and S. Bennett, *Quantum nanoelectromechanics with electrons, quasi-particles and Cooper pairs: effective bath descriptions and strong feedback effects*, New J. Phys. **7**, 238 (2005).
[213] J. L. Garbini, K. J. Bruland, W. M. Dougherty, and J. A. Sidles, *Optimal control of force microscope cantilevers. I. Controller design*, J. Appl. Phys. **80**, 1951 (1996).
[214] K. J. Bruland, J. L. Garbini, W. M. Dougherty, and J. A. Sidles, *Optimal control of force microscope cantilevers. II. Magnetic coupling implementation*, J. Appl. Phys. **80**, 1959 (1996).
[215] J. Mertz, O. Marti, and J. Mlynek, *Regulation of a microcantilever response by force feedback*, Appl. Phys. Lett. **62**, 2344 (1993).
[216] D. Rugar, C. S. Yannoni, and J. A. Sidles, *Mechanical detection of magnetic resonance*, Nature **360**, 563 (1992).
[217] A. Hopkins, K. Jacobs, S. Habib, and K. Schwab, *Feedback cooling of a nanomechanical resonator*, Phys. Rev. B **68**, 235328 (2003).
[218] S. Mancini, D. Vitali, and P. Tombesi, *Optomechanical Cooling of a Macroscopic Oscillator by Homodyne Feedback*, Phys. Rev. Lett. **80**, 688

(1998).
[219] P. F. Cohadon, A. Heidmann, and M. Pinard, *Cooling of a Mirror by Radiation Pressure*, Phys. Rev. Lett. **83**, 3174 (1999).
[220] J. M. Nichol, E. R. Hemesath, L. J. Lauhon, and R. Budakian, *Controlling the nonlinearity of silicon nanowire resonators using active feedback*, Appl. Phys. Lett. **95**, 123116 (pages 3) (2009).
[221] T. J. Kippenberg and K. J. Vahala, *Cavity optomechanics: Back-action at the mesoscale*, Science **321**, 1172 (2008).
[222] F. Marquardt and S. M. Girvin, *Optomechanics*, Physics **2**, 40 (2009).
[223] J. D. Teufel, C. A. Regal, and K. W. Lehnert, *Prospects for cooling nanomechanical motion by coupling to a superconducting microwave resonator*, New J. Phys **10**, 095002 (11pp) (2008).
[224] V. B. Braginskiĭ and A. B. Manukin, *Ponderomotive Effects of Electromagnetic Radiation*, Soviet Journal of Experimental and Theoretical Physics **25**, 653 (1967).
[225] A. Dorsel, J. D. McCullen, P. Meystre, E. Vignes, and H. Walther, *Optical Bistability and Mirror Confinement Induced by Radiation Pressure*, Phys. Rev. Lett. **51**, 1550 (1983).
[226] A. Buonanno and Y. Chen, *Signal recycled laser-interferometer gravitational-wave detectors as optical springs*, Phys. Rev. D **65**, 042001 (2002).
[227] B. S. Sheard, M. B. Gray, C. M. Mow-Lowry, D. E. McClelland, and S. E. Whitcomb, *Observation and characterization of an optical spring*, Phys. Rev. A **69**, 051801 (2004).
[228] T. Corbitt, D. Ottaway, E. Innerhofer, J. Pelc, and N. Mavalvala, *Measurement of radiation-pressure-induced optomechanical dynamics in a suspended Fabry-Perot cavity*, Phys. Rev. A **74**, 021802 (pages 4) (2006).
[229] M. Hossein-Zadeh and K. J. Vahala, *Observation of optical spring effect in a microtoroidal optomechanical resonator*, Opt. Lett. **32**, 1611 (2007).
[230] G. S. Wiederhecker, S. Manipatruni, S. Lee, and M. Lipson, *Broadband tuning of optomechanical cavities*, Opt. Express **19**, 2782 (2011).
[231] J. Rosenberg, Q. Lin, and O. Painter, *Static and dynamic wavelength routing via the gradient optical force*, Nat Photon **3**, 478 (2009).
[232] V. B. Braginskiĭ, A. B. Manukin, and M. Y. Tikhonov, *Investigation of dissipative ponderomotive effects of electromagnetic radiation*, Soviet Journal of Experimental and Theoretical Physics **31**, 829 (1970).
[233] I. Wilson-Rae, N. Nooshi, W. Zwerger, and T. J. Kippenberg, *Theory of Ground State Cooling of a Mechanical Oscillator Using Dynamical Backaction*, Phys. Rev. Lett. **99**, 093901 (pages 4) (2007).
[234] F. Marquardt, J. P. Chen, A. A. Clerk, and S. M. Girvin, *Quantum Theory of Cavity-Assisted Sideband Cooling of Mechanical Motion*, Phys. Rev. Lett. **99**, 093902 (pages 4) (2007).
[235] F. Elste, S. M. Girvin, and A. A. Clerk, *Quantum Noise Interference and Backaction Cooling in Cavity Nanomechanics*, Phys. Rev. Lett. **102**, 207209 (pages 4) (2009).
[236] M. I. Dykman, *Heating and cooling of local and quasilocal vibrations by a nonresonance field*, Sov. Phys. Solid State **20**, 1306 (1978).
[237] S. Gröblacher, K. Hammerer, M. R. Vanner, and M. Aspelmeyer, *Observation of strong coupling between a micromechanical resonator and an optical cavity field*, Nature **460**, 724 (2009).
[238] N. P. Linthorne, P. J. Veitch, and D. G. Blair, *Interaction of a parametric transducer with a resonant bar gravitational radiation detector*, J. Phys. D **23**, 1 (1990).
[239] C. Metzger, M. Ludwig, C. Neuenhahn, A. Ortlieb, I. Favero, K. Karrai, and F. Marquardt, *Self-Induced Oscillations in an Optomechanical System Driven by Bolometric Backaction*, Phys. Rev. Lett. **101**, 133903 (2008).
[240] M. P. Blencowe, J. Imbers, and A. D. Armour, *Dynamics of a nanomechanical resonator coupled to a superconducting single-electron transistor*, New J. Phys. **7**, 236 (2005).
[241] S. Zippilli, A. Bachtold, and G. Morigi, *Ground-state-cooling vibrations of suspended carbon nanotubes with constant electron current*, Phys. Rev. B **81**, 205408 (2010).
[242] M. Poot, S. Etaki, I. Mahboob, K. Onomitsu, H. Yamaguchi, Y. M. Blanter, and H. S. J. van der Zant, *Tunable Backaction of a DC SQUID on an Integrated Micromechanical Resonator*, Phys. Rev. Lett. **105**, 207203 (2010).
[243] V. B. Braginsky, S. E. Strigin, and S. P. Vyatchanin, *Parametric oscillatory instability in Fabry-Perot interferometer*, Phys. Lett. A **287**, 331 (2001).
[244] P. Meystre, E. M. Wright, J. D. McCullen, and E. Vignes, *Theory of radiation-pressure-driven interferometers*, J. Opt. Soc. Am. B **2**, 1830 (1985).
[245] F. Marquardt, J. G. E. Harris, and S. M. Girvin, *Dynamical Multistability Induced by Radiation Pressure in High-Finesse Micromechanical Optical Cavities*, Phys. Rev. Lett. **96**, 103901 (2006).
[246] M. Ludwig, B. Kubala, and F. Marquardt, *The optomechanical instability in the quantum regime*, New Journal of Physics **10**, 095013 (2008).
[247] T. J. Kippenberg, H. Rokhsari, T. Carmon, A. Scherer, and K. J. Vahala, *Analysis of Radiation-Pressure Induced Mechanical Oscillation of an Optical Microcavity*, Phys. Rev. Lett. **95**, 033901 (2005).
[248] T. Carmon, H. Rokhsari, L. Yang, T. J. Kippenberg, and K. J. Vahala, *Temporal Behavior of Radiation-Pressure-Induced Vibrations of an Optical Microcavity Phonon Mode*, Phys. Rev. Lett. **94**, 223902 (2005).
[249] R. Ma, A. Schliesser, P. Del'Haye, A. Dabirian, G. Anetsberger, and T. J. Kippenberg, *Radiation-pressure-driven vibrational modes in ultrahigh-Q silica microspheres*, Opt. Lett. **32**, 2200 (2007).
[250] M. Bagheri, M. Poot, M. Li, W. P. H. Pernice, and H. X. Tang, *Dynamic manipulation of nanomechanical resonators in the high-amplitude regime and non-volatile mechanical memory operation*, Nat Nano **ADVANCE ONLINE PUBLICATION** (2011).
[251] I. Mahboob, H. Okamoto, M. Ueki, and H. Yamaguchi, *Electron phase modulation in a suspended InAs/AlGaSb nanomechanical beam*, Appl. Phys. Lett. **89**, 192106 (pages 3) (2006).
[252] J. B. Hertzberg, T. Rocheleau, T. Ndukum, M. Savva, A. A. Clerk, and K. C. Schwab, *Back-action-evading measurements of nanomechanical motion*, Nat Phys **6**, 213 (2010).
[253] J. Sulkko, M. A. Sillanpää, P. Häkkinen, L. Lechner, M. Helle, A. Fefferman, J. Parpia, and P. J. Hakonen, *Strong Gate Coupling of High-Q Nanomechanical Resonators*, Nano Letters **10**, 4884 (2010).
[254] J. D. Teufel, D. Li, M. S. Allman, K. Cicak, A. J. Sirois, J. D. Whittaker, and R. W. Simmonds, *Circuit cavity electromechanics in the strong-coupling regime*, Nature **471**, 204 (2011).
[255] S. Weis, R. Rivire, S. Delglise, E. Gavartin, O. Arcizet, A. Schliesser, and T. J. Kippenberg, *Optomechanically Induced Transparency*, Science **330**, 1520 (2010).
[256] E. Gavartin, R. Braive, I. Sagnes, O. Arcizet, A. Beveratos, T. J. Kippenberg, and I. Robert-Philip, *Optomechanical Coupling in a Two-Dimensional Photonic Crystal Defect Cavity*, Phys. Rev. Lett. **106**, 203902 (2011).
[257] T. J. Kippenberg and K. J. Vahala, *Cavity Opto-Mechanics*, Opt. Express **15**, 17172 (2007).
[258] I. Favero and K. Karrai, *Optomechanics of deformable optical cavities*, Nat Photon **3**, 201 (2009).
[259] M. L. Gorodetsky, A. Schliesser, G. Anetsberger, S. Deleglise, and T. J. Kippenberg, *Determination of the vacuum optomechanical coupling rate using frequency noise calibration*, Opt. Express **18**, 23236 (2010).
[260] H. Walther, B. T. H. Varcoe, B.-G. Englert, and T. Becker, *Cavity quantum electrodynamics*, Reports on Progress in Physics **69**, 1325 (2006).
[261] D. K. Armani, T. J. Kippenberg, S. M. Spillane, and K. J. Vahala, *Ultra-high-Q toroid microcavity on a chip*, Nature **421**, 925 (2003).

[262] A. Abramovici, W. E. Althouse, R. W. P. Drever, Y. Gursel, S. Kawamura, F. J. Raab, D. Shoemaker, L. Sievers, R. E. Spero, K. S. Thorne, et al., *LIGO: The Laser Interferometer Gravitational-Wave Observatory*, Science **256**, 325 (1992).
[263] J. M. Dobrindt, I. Wilson-Rae, and T. J. Kippenberg, *Parametric Normal-Mode Splitting in Cavity Optomechanics*, Phys. Rev. Lett. **101**, 263602 (2008).
[264] A. H. Safavi-Naeini, T. P. M. Alegre, J. Chan, M. Eichenfield, M. Winger, Q. Lin, J. T. Hill, D. E. Chang, and O. Painter, *Electromagnetically induced transparency and slow light with optomechanics*, Nature **472**, 69 (2011).
[265] P. Verlot, A. Tavernarakis, T. Briant, P.-F. Cohadon, and A. Heidmann, *Scheme to Probe Optomechanical Correlations between Two Optical Beams Down to the Quantum Level*, Phys. Rev. Lett. **102**, 103601 (2009).
[266] K. Børkje, A. Nunnenkamp, B. M. Zwickl, C. Yang, J. G. E. Harris, and S. M. Girvin, *Observability of radiation-pressure shot noise in optomechanical systems*, Phys. Rev. A **82**, 013818 (2010).
[267] J. C. Sankey, C. Yang, B. M. Zwickl, A. M. Jayich, and J. G. E. Harris, *Strong and tunable nonlinear optomechanical coupling in a low-loss system*, Nat Phys **6**, 707 (2010).
[268] K. Jacobs, P. Lougovski, and M. Blencowe, *Continuous Measurement of the Energy Eigenstates of a Nanomechanical Resonator without a Nondemolition Probe*, Phys. Rev. Lett. **98**, 147201 (2007).
[269] K. Jacobs, A. N. Jordan, and E. K. Irish, *Energy measurements and preparation of canonical phase states of a nano-mechanical resonator*, EPL (Europhysics Letters) **82**, 18003 (2008).
[270] M. Cai, O. Painter, and K. J. Vahala, *Observation of Critical Coupling in a Fiber Taper to a Silica-Microsphere Whispering-Gallery Mode System*, Phys. Rev. Lett. **85**, 74 (2000).
[271] G. Anetsberger, R. Riviere, A. Schliesser, O. Arcizet, and T. J. Kippenberg, *Ultralow-dissipation optomechanical resonators on a chip*, Nat Photon **2**, 627 (2008).
[272] T. G. McRae, K. H. Lee, G. I. Harris, J. Knittel, and W. P. Bowen, *Cavity optoelectromechanical system combining strong electrical actuation with ultrasensitive transduction*, Phys. Rev. A **82**, 023825 (2010).
[273] T. P. M. Alegre, A. Safavi-Naeini, M. Winger, and O. Painter, *Quasi-two-dimensional optomechanical crystals with a complete phononic bandgap*, Opt. Express **19**, 5658 (2011).
[274] M. Li, P. H. P., and T. X., *Tunable bipolar optical interactions between guided lightwaves*, Nat Photon **3**, 464 (2009).
[275] J. Roels, I. De Vlaminck, L. Lagae, B. Maes, D. Van Thourhout, and R. Baets, *Tunable optical forces between nanophotonic waveguides*, Nat Nano **4**, 510 (2009).
[276] P. K. Day, H. G. LeDuc, B. A. Mazin, A. Vayonakis, and J. Zmuidzinas, *A broadband superconducting detector suitable for use in large arrays*, Nature **425**, 817 (2003).
[277] L. Hao, J. C. Gallop, and D. Cox, *Excitation, detection, and passive cooling of a micromechanical cantilever using near-field of a microwave resonator*, Appl. Phys. Lett. **95**, 113501 (pages 3) (2009).
[278] S. T. Purcell, P. Vincent, C. Journet, and V. T. Binh, *Tuning of Nanotube Mechanical Resonances by Electric Field Pulling*, Phys. Rev. Lett. **89**, 276103 (2002).
[279] I. D. Vlaminck, J. Roels, D. Taillaert, D. V. Thourhout, R. Baets, L. Lagae, and G. Borghs, *Detection of nanomechanical motion by evanescent light wave coupling*, Appl. Phys. Lett. **90**, 233116 (pages 3) (2007).
[280] M. Nordström, D. A. Zauner, M. Calleja, J. Hübner, and A. Boisen, *Integrated optical readout for miniaturization of cantilever-based sensor system*, Appl. Phys. Lett. **91**, 103512 (pages 3) (2007).
[281] M. W. Pruessner, N. Siwak, K. Amarnath, S. Kanakaraju, W.-H. Chuang, and R. Ghodssi, *End-coupled optical waveguide MEMS devices in the indium phosphide material system*, J. Micromech. Microeng. **16**, 832 (2006).
[282] H. Park, A. K. L. Lim, A. P. Alivisatos, J. Park, and P. L. McEuen, *Fabrication of metallic electrodes with nanometer separation by electromigration*, Appl. Phys. Lett. **75**, 301 (1999).
[283] M. R. Kan, D. C. Fortin, E. Finley, K.-M. Cheng, M. R. Freeman, and W. K. Hiebert, *Super-rolloff electron tunneling transduction of nanomechanical motion using frequency downmixing*, Appl. Phys. Lett. **97**, 253108 (pages 3) (2010).
[284] C. B. Doiron, B. Trauzettel, and C. Bruder, *Measuring the Momentum of a Nanomechanical Oscillator through the Use of Two Tunnel Junctions*, Phys. Rev. Lett. **100**, 027202 (2008).
[285] T. L. Schmidt, K. Børkje, C. Bruder, and B. Trauzettel, *Detection of Qubit-Oscillator Entanglement in Nanoelectromechanical Systems*, Phys. Rev. Lett. **104**, 177205 (2010).
[286] A. Erbe, R. H. Blick, A. Tilke, A. Kriele, and J. P. Kotthaus, *A mechanically flexible tunneling contact operating at radio frequencies*, Appl. Phys. Lett. **73**, 3751 (1998).
[287] D. R. Koenig, E. M. Weig, and J. P. Kotthaus, *Ultrasonically driven nanomechanical single-electron shuttle*, Nat Nano **3**, 482 (2008).
[288] R. I. Shekhter, L. Y. Gorelik, M. Jonson, Y. M. Galperin, and V. M. Vinokur, *Nanomechanical shuttle transfer of electrons*, J. Comput. Theor. Nanosci. **4**, 860 (2007).
[289] H. Grabert and M. H. Devoret, eds., *Single charge tunneling : Coulomb blockade phenomena in nanostructures*, NATO ASI Series (Plenum, 1992).
[290] A. D. Armour, *Current noise of a single-electron transistor coupled to a nanomechanical resonator*, Phys. Rev. B **70**, 165315 (2004).
[291] M. Blencowe, *Quantum electromechanical systems*, Phys. Rep. **395**, 159 (2004).
[292] V. Koerting, T. L. Schmidt, C. B. Doiron, B. Trauzettel, and C. Bruder, *Transport properties of a superconducting single-electron transistor coupled to a nanomechanical oscillator*, Phys. Rev. B **79**, 134511 (2009).
[293] A. K. Hüttel, M. Poot, B. Witkamp, and H. S. J. van der Zant, *Nanoelectromechanics of suspended carbon nanotubes*, New J. Phys. **10**, 095003 (2008).
[294] R. Knobel, C. S. Yung, and A. N. Cleland, *Single-electron transistor as a radio-frequency mixer*, Appl. Phys. Lett. **81**, 532 (2002).
[295] N. M. Chtchelkatchev, W. Belzig, and C. Bruder, *Charge transport through a single-electron transistor with a mechanically oscillating island*, Phys. Rev. B **70**, 193305 (2004).
[296] Y. A. Pashkin, T. F. Li, J. P. Pekola, O. Astafiev, D. A. Knyazev, F. Hoehne, H. Im, Y. Nakamura, and J. S. Tsai, *Detection of mechanical resonance of a single-electron transistor by direct current*, Appl. Phys. Lett. **96**, 263513 (pages 3) (2010).
[297] C. Beenakker and H. van Houten, in *Semiconductor Heterostructures and Nanostructures*, edited by H. Ehrenreich and D. Turnbull (Academic Press, 1991), vol. Volume 44, pp. 1–228, URL `http://www.sciencedirect.com/science/article/B8GXT-4S9NXKP-6/2/36f3628c2e82673200f1996718bf2495`.
[298] A. N. Cleland, J. S. Aldridge, D. C. Driscoll, and A. C. Gossard, *Nanomechanical displacement sensing using a quantum point contact*, Appl. Phys. Lett. **81**, 1699 (2002).
[299] J. Stettenheim, M. Thalakulam, F. Pan, M. Bal, Z. Ji, W. Xue, L. Pfeiffer, K. W. West, M. P. Blencowe, and A. J. Rimberg, *A macroscopic mechanical resonator driven by mesoscopic electrical back-action*, Nature **466**, 86 (2010).
[300] I. Bargatin, E. B. Myers, J. Arlett, B. Gudlewski, and M. L. Roukes, *Sensitive detection of nanomechanical motion using piezoresistive signal*

*downmixing*, Appl. Phys. Lett. **86**, 133109 (2005).
[301] R. G. Beck, M. A. Eriksson, M. A. Topinka, R. M. Westervelt, K. D. Maranowski, and A. C. Gossard, *GaAs/AlGaAs self-sensing cantilevers for low temperature scanning probe microscopy*, Appl. Phys. Lett. **73**, 1149 (1998).
[302] S. Watanabe and T. Fujii, *Micro-fabricated piezoelectric cantilever for atomic force microscopy*, Rev. Sci. Instrum. **67**, 3898 (1996).
[303] T. Itoh and T. Suga, *Scanning force microscope using a piezoelectric microcantilever*, Journal of Vacuum Science & Technology B **12**, 1581 (1994).
[304] H. X. Tang, X. M. H. Huang, M. L. Roukes, M. Bichler, and W. Wegscheider, *Two-dimensional electron-gas actuation and transduction for GaAs nanoelectromechanical systems*, Appl. Phys. Lett. **81**, 3879 (2002).
[305] R. Knobel and A. N. Cleland, *Piezoelectric displacement sensing with a single-electron transistor*, Appl. Phys. Lett. **81**, 2258 (2002).
[306] I. Mahboob and H. Yamaguchi, *Piezoelectrically pumped parametric amplification and Q enhancement in an electromechanical oscillator*, Appl. Phys. Lett. **92**, 173109 (pages 3) (2008).
[307] H. Okamoto, D. Ito, K. Onomitsu, H. Sanada, H. Gotoh, T. Sogawa, and H. Yamaguchi, *Vibration Amplification, Damping, and Self-Oscillations in Micromechanical Resonators Induced by Optomechanical Coupling through Carrier Excitation*, Phys. Rev. Lett. **106**, 036801 (2011).
[308] S. C. Masmanidis, R. B. Karabalin, I. De Vlaminck, G. Borghs, M. R. Freeman, and M. L. Roukes, *Multifunctional Nanomechanical Systems via Tunably Coupled Piezoelectric Actuation*, Science **317**, 780 (2007).
[309] J. Clarke and A. Braginski, *The SQUID Handbook volume 1* (Wiley-VCH Verlag, GmbH and Co. KGaA, Weinheim, 2004).
[310] O. Usenko, A. Vinante, G. Wijts, and T. H. Oosterkamp, *A superconducting quantum interference device based read-out of a subattonewton force sensor operating at millikelvin temperatures*, Appl. Phys. Lett. **98**, 133105 (pages 3) (2011).
[311] X. Zhou and A. Mizel, *Nonlinear Coupling of Nanomechanical Resonators to Josephson Quantum Circuits*, Phys. Rev. Lett. **97**, 267201 (pages 4) (2006).
[312] E. Buks and M. P. Blencowe, *Decoherence and recoherence in a vibrating rf SQUID*, Phys. Rev. B **74**, 174504 (pages 8) (2006).
[313] F. Xue, Y. D. Wang, C. P. Sun, H. Okamoto, H. Yamaguchi, and K. Semba, *Controllable coupling between flux qubit and nanomechanical resonator by magnetic field*, New J. Phys. **9**, 35 (2007).
[314] M. P. Blencowe and E. Buks, *Quantum analysis of a linear dc SQUID mechanical displacement detector*, Phys. Rev. B **76**, 014511 (pages 16) (2007).
[315] E. Buks, E. Segev, S. Zaitsev, B. Abdo, and M. P. Blencowe, *Quantum nondemolition measurement of discrete Fock states of a nanomechanical resonator*, EPL **81**, 10001 (2008).
[316] Y.-D. Wang, K. Semba, and H. Yamaguchi, *Cooling of a micro-mechanical resonator by the back-action of Lorentz force*, New J. Phys. **10**, 043015 (15pp) (2008).
[317] P. D. Nation, M. P. Blencowe, and E. Buks, *Quantum analysis of a nonlinear microwave cavity-embedded dc SQUID displacement detector*, Phys. Rev. B **78**, 104516 (pages 17) (2008).
[318] K. Xia and J. Evers, *Ground State Cooling of a Nanomechanical Resonator in the Nonresolved Regime via Quantum Interference*, Phys. Rev. Lett. **103**, 227203 (2009).
[319] S. Pugnetti, Y. M. Blanter, F. Dolcini, and R. Fazio, *Dynamics of a SQUID ratchet coupled to a nanomechanical resonator*, Phys. Rev. B **79**, 174516 (2009).
[320] S. Pugnetti, Y. M. Blanter, and R. Fazio, *Resonant coupling of a SQUID to a mechanical resonator*, EPL (Europhysics Letters) **90**, 48007 (2010).
[321] D. S. Greywall, B. Yurke, P. A. Busch, A. N. Pargellis, and R. L. Willett, *Evading amplifier noise in nonlinear oscillators*, Phys. Rev. Lett. **72**, 2992 (1994).
[322] A. N. Cleland and M. L. Roukes, *Fabrication of high frequency nanometer scale mechanical resonators from bulk Si crystals*, Appl. Phys. Lett. **69**, 2653 (1996).
[323] W. J. Venstra and H. S. J. van der Zant, *Efficient readout of micromechanical resonator arrays in ambient conditions*, Appl. Phys. Lett. **93**, 234106 (2008).
[324] A. Gaidarzhy, G. Zolfagharkhani, R. L. Badzey, and P. Mohanty, *Spectral response of a gigahertz-range nanomechanical oscillator*, Appl. Phys. Lett. **86**, 254103 (pages 3) (2005).
[325] J. M. Thijssen and H. S. J. Van der Zant, *Charge transport and single-electron effects in nanoscale systems*, phys. stat. sol. (b) **245**, 1455 (2008).
[326] K. D. McCarthy, N. Prokof'ev, and M. T. Tuominen, *Incoherent dynamics of vibrating single-molecule transistors*, Phys. Rev. B **67**, 245415 (2003).
[327] H. Park, J. Park, A. K. Lim, E. H. Anderson, P. A. Alivisatos, and P. L. McEuen, *Nanomechanical oscillations in a single-C60 transistor*, Nature **407**, 57 (2000).
[328] B. J. LeRoy, S. G. Lemay, J. Kong, and C. Dekker, *Electrical generation and absorption of phonons in carbon nanotubes*, Nature **432**, 371 (2004).
[329] S. Sapmaz, P. Jarillo-Herrero, Y. M. Blanter, C. Dekker, and H. S. J. van der Zant, *Tunneling in Suspended Carbon Nanotubes Assisted by Longitudinal Phonons*, Phys. Rev. Lett. **96**, 026801 (pages 4) (2006).
[330] J. Koch and F. von Oppen, *Franck-Condon Blockade and Giant Fano Factors in Transport through Single Molecules*, Phys. Rev. Lett. **94**, 206804 (2005).
[331] F. Pistolesi and S. Labarthe, *Current blockade in classical single-electron nanomechanical resonator*, Phys. Rev. B **76**, 165317 (2007).
[332] E. M. Weig, R. H. Blick, T. Brandes, J. Kirschbaum, W. Wegscheider, M. Bichler, and J. P. Kotthaus, *Single-Electron-Phonon Interaction in a Suspended Quantum Dot Phonon Cavity*, Phys. Rev. Lett. **92**, 046804 (2004).
[333] R. Leturcq, C. Stampfer, K. Inderbitzin, L. Durrer, C. Hierold, E. Mariani, M. G. Schultz, F. von Oppen, and K. Ensslin, *Franck-Condon blockade in suspended carbon nanotube quantum dots*, Nat Phys **5**, 327 (2009).
[334] A. K. Hüttel, B. Witkamp, M. Leijnse, M. R. Wegewijs, and H. S. J. van der Zant, *Pumping of Vibrational Excitations in the Coulomb-Blockade Regime in a Suspended Carbon Nanotube*, Phys. Rev. Lett. **102**, 225501 (2009).
[335] M. D. LaHaye, J. Suh, P. M. Echternach, K. C. Schwab, and M. L. Roukes, *Nanomechanical measurements of a superconducting qubit*, Nature **459**, 960 (2009).
[336] R. Ciolfi, *Development of photodetectors for the squeezing experiment at the ligo 40m gw interferometer*, LIGO-T060246-00-R (2006).
[337] R. H. Koch, D. J. V. Harlingen, and J. Clarke, *Quantum noise theory for the dc SQUID*, Appl. Phys. Lett. **38**, 380 (1981).
[338] M. Mück, J. B. Kycia, and J. Clarke, *Superconducting quantum interference device as a near-quantum-limited amplifier at 0.5 GHz.*, Appl. Phys. Lett. **78**, 967 (2001).
[339] A. A. Clerk, S. M. Girvin, and A. D. Stone, *Quantum-limited measurement and information in mesoscopic detectors*, Phys. Rev. B **67**, 165324 (2003).
[340] S. A. Gurvitz, *Measurements with a noninvasive detector and dephasing mechanism*, Phys. Rev. B **56**, 15215 (1997).
[341] H. Takahasi, *Advances in Communication Systems*, vol. 1 (Academic Press, 1965).
[342] V. Peano and M. Thorwart, *Macroscopic quantum effects in a strongly driven nanomechanical resonator*, Phys. Rev. B **70**, 235401 (2004).

[343] I. Katz, A. Retzker, R. Straub, and R. Lifshitz, *Signatures for a Classical to Quantum Transition of a Driven Nonlinear Nanomechanical Resonator*, Phys. Rev. Lett. **99**, 040404 (2007).
[344] M. J. Woolley, G. J. Milburn, and C. M. Caves, *Nonlinear quantum metrology using coupled nanomechanical resonators*, New J. Phys. **10**, 125018 (2008).
[345] B. M. Chernobrod and G. P. Berman, *Spin microscope based on optically detected magnetic resonance*, Journal of Applied Physics **97**, 014903 (pages 3) (2005).
[346] G. P. Berman, A. R. Bishop, B. M. Chernobrod, M. E. Hawley, G. W. Brown, and V. I. Tsifrinovich, *Measurement of single electron and nuclear spin states based on optically detected magnetic resonance*, Journal of Physics: Conference Series **38**, 167 (2006).
[347] C. L. Degen, *Scanning magnetic field microscope with a diamond single-spin sensor*, Appl. Phys. Lett. **92**, 243111 (pages 3) (2008).
[348] A. C. Bleszynski-Jayich, W. E. Shanks, B. Peaudecerf, E. Ginossar, F. von Oppen, L. Glazman, and J. G. E. Harris, *Persistent Currents in Normal Metal Rings*, Science **326**, 272 (2009).
[349] D. E. Chang, A. H. Safavi-Naeini, M. Hafezi, and O. Painter, *Slowing and stopping light with an optomechanical crystal array*, AIP Conference Proceedings **1291**, 13 (2010).
[350] A. H. Safavi-Naeini and O. Painter, *Proposal for an optomechanical traveling wave phononphoton translator*, New J. Phys. **13**, 013017 (2011).
[351] D. Rugar, R. Budakian, H. J. Mamin, and B. W. Chui, *Single spin detection by magnetic resonance force microscopy*, Nature **430**, 329 (2004).
[352] K. L. Ekinci, X. M. H. Huang, and M. L. Roukes, *Ultrasensitive nanoelectromechanical mass detection*, Appl. Phys. Lett. **84**, 4469 (2004).
[353] Y. T. Yang, C. Callegari, X. L. Feng, K. L. Ekinci, and M. L. Roukes, *Zeptogram-Scale Nanomechanical Mass Sensing*, Nano Letters **6**, 583 (2006).
[354] A. K. Naik, M. S. Hanay, W. K. Hiebert, X. L. Feng, and M. L. Roukes, *Towards single-molecule nanomechanical mass spectrometry*, Nat Nano **4**, 445 (2009).
[355] K. Eom, H. S. Park, D. S. Yoon, and T. Kwon, *Nanomechanical resonators and their applications in biological/chemical detection: Nanomechanics principles*, Phys. Rep. **503**, 115 (2011).
[356] K. L. Ekinci, Y. T. Yang, and M. L. Roukes, *Ultimate limits to inertial mass sensing based upon nanoelectromechanical systems*, Journal of Applied Physics **95**, 2682 (2004).
[357] P. Treutlein, D. Hunger, S. Camerer, T. W. Hänsch, and J. Reichel, *Bose-Einstein Condensate Coupled to a Nanomechanical Resonator on an Atom Chip*, Phys. Rev. Lett. **99**, 140403 (2007).
[358] F. Brennecke, S. Ritter, T. Donner, and T. Esslinger, *Cavity Optomechanics with a Bose-Einstein Condensate*, Science **322**, 235 (2008).
[359] K. Hammerer, M. Wallquist, C. Genes, M. Ludwig, F. Marquardt, P. Treutlein, P. Zoller, J. Ye, and H. J. Kimble, *Strong Coupling of a Mechanical Oscillator and a Single Atom*, Phys. Rev. Lett. **103**, 063005 (2009).
[360] K. Vahala, M. Herrmann, S. Knunz, V. Batteiger, G. Saathoff, T. W. Hansch, and T. Udem, *A phonon laser*, Nat Phys **5**, 682 (2009).
[361] D. Hunger, S. Camerer, T. W. Hänsch, D. König, J. P. Kotthaus, J. Reichel, and P. Treutlein, *Resonant Coupling of a Bose-Einstein Condensate to a Micromechanical Oscillator*, Phys. Rev. Lett. **104**, 143002 (2010).
[362] A. A. Geraci and J. Kitching, *Ultracold mechanical resonators coupled to atoms in an optical lattice*, Phys. Rev. A **80**, 032317 (2009).